Challenge Journal of
STRUCTURAL MECHANICS

Vol.7 No.2 (2021)

Mindlin's theory buckling compressive strength dynamic analysis dynamic response earthquake finite element analysis finite element method mechanical properties operational modal analysis optimization pushover analysis railways reinforced concrete seismic analysis seismic design seismic isolation shallow foundations steel silo teaching-learning based optimization th late

ISSN 2149-8024

TULPAR
ACADEMIC PUBLISHING

Challenge Journal of Structural Mechanics

EDITOR IN CHIEF

Prof. Dr. Ümit UZMAN
Avrasya University, Turkey

EDITORIAL BOARD

Prof. Dr. A. Ghani RAZAQPUR
McMaster University, Canada

Prof. Dr. Paulo B. LOURENÇO
University of Minho, Portugal

Prof. Dr. Gilbert Rainer GILLICH
Eftimie Murgu University of Resita, Romania

Prof. Dr. Long-Yuan LI
University of Plymouth, United Kingdom

Prof. Dr. Željana NIKOLIĆ
University of Split, Croatia

Prof. Dr. Ş. Burhanettin ALTAN
Giresun University, Turkey

Prof. Dr. Togay ÖZBAKKALOĞLU
Texas State University, United States

Prof. Dr. Mehmet ÖZYAZICIOĞLU
Atatürk University, Turkey

Assoc. Prof. Dr. Bing QU
California Polytechnic State University, United States

Assoc. Prof. Dr. Naida ADEMOVIĆ
University of Sarajevo, Bosnia and Herzegovina

Assoc. Prof. Dr. Anna SAETTA
IUAV University of Venice, Italy

Prof. Dr. Halil SEZEN
The Ohio State University, United States

Prof. Dr. Adem DOĞANGÜN
Uludağ University, Turkey

Prof. Dr. M. Asghar BHATTI
University of Iowa, United States

Prof. Dr. Reza KIANOUSH
Ryerson University, Canada

Prof. Dr. Y. Cengiz TOKLU
Beykent University, Turkey

Prof. Dr. Habib UYSAL
Atatürk University, Turkey

Prof. Dr. Filiz PİROĞLU
İstanbul Technical University, Turkey

Assoc. Prof. Dr. Khaled MARAR
Eastern Mediterranean University, Cyprus

Assoc. Prof. Dr. Hong SHEN
Shanghai Jiao Tong University, China

Assoc. Prof. Dr. Nunziante VALOROSO
Parthenope University of Naples, Italy

Assoc. Prof. Dr. Serdar ÇARBAŞ
Karamanoğlu Mehmetbey University, Turkey

Assoc. Prof. Dr. Taha IBRAHIM
Benha University, Egypt

Assoc. Prof. Dr. Alper BÜYÜKKARAGÖZ
Gazi University, Turkey

Dr. Sandro CARBONARI
Marche Polytechnic University, Italy

Dr. Chien-Kuo CHIU
National Taiwan University of Science and Technology, Taiwan

Dr. Teng WU
University at Buffalo, United States

Dr. Pierfrancesco CACCIOLA
University of Brighton, United Kingdom

Dr. Marco CORRADI
University of Perugia, Italy

Dr. José SANTOS
University of Madeira, Portugal

Dr. Luca LANDI
University of Bologna, Italy

Dr. Mirko MAZZA
University of Calabria, Italy

Dr. Süleyman Nazif ORHAN
Erzurum Technical University, Turkey

Assoc. Prof. Dr. Amin GHANNADIASL
University of Mohaghegh Ardabili, Iran

Assoc. Prof. Dr. Fatih Mehmet ÖZKAL
Atatürk University, Turkey

Dr. Zühal ÖZDEMİR
The University of Sheffield, United Kingdom

Dr. Syahril TAUFIK
Lambung Mangkurat University, Indonesia

Dr. J. Michael GRAYSON
The Citadel - The Military College of South Carolina, United States

Dr. Fabio MAZZA
University of Calabria, Italy

Dr. Alberto Maria AVOSSA
Second University of Naples, Italy

Dr. Susanta GHOSH
Michigan Technological University, United States

Dr. Burak Kaan ÇIRPICI
Erzurum Technical University, Turkey

Dr. Panatchai CHETCHOTISAK
Rajamangala University of Technology Isan, Thailand

E-mail: *cjsmec@challengejournal.com*

Web page: *cjsmec.challengejournal.com*

TULPAR Academic Publishing
www.tulparpublishing.com

Challenge Journal of Structural Mechanics

CONTENTS

Research Articles

TULPAR
ACADEMIC PUBLISHING

CHALLENGE JOURNAL OF STRUCTURAL MECHANICS 7 (2) (2021) 58–63

Challenge Journal of Structural Mechanics

Research Article

Buckling analysis of natural fiber reinforced composites

Celal Cakiroglu [a,*], Gebrail Bekdaş [b]

[a] *Department of Civil Engineering, Turkish-German University, 34820 İstanbul, Turkey*
[b] *Department of Civil Engineering, İstanbul University-Cerrahpaşa, 34320 İstanbul, Turkey*

ABSTRACT

In the recent years natural fiber reinforced composites are increasingly receiving attention from the researchers and engineers due to their mechanical properties comparable to the conventional synthetic fibers and due to their ease of preparation, low cost and density, eco-friendliness and bio-degradability. Natural fibers such as kenaf or flux are being considered as a viable replacement for glass, aramid or carbon. Extensive experimental studies have been carried out to determine the mechanical behavior of different natural fiber types such as the elastic modulus, tensile strength, flexural strength and the Poisson's ratio. This paper presents a review of the various experimental studies in the field of fiber reinforced composites while summarizing the research outcome about the elastic properties of the major types of natural fiber reinforced composites. Furthermore, the performance of a kenaf reinforced composite plate is demonstrated using finite element analysis and results are compared to a glass fiber reinforced laminated composite plate.

ARTICLE INFO

Article history:
Received 31 August 2020
Revised 28 September 2020
Accepted 23 October 2020

Keywords:
Buckling
Natural fibers
Mechanical properties
Laminated composite plates

1. Introduction

Composite materials are playing an important role in the manufacturing of lightweight structural components in the recent years. The increase in the application of composites as a structural material is mainly because of their superior mechanical properties compared to the regular structural materials such as steel and aluminum. The high stiffness and light weight of composites reduce the production cost and increase the product quality. Carbon fiber reinforced polymers (CFRP), boron/epoxy composites and glass fiber reinforced polymers are some of the most widely used composite material types in the lightweight structures industry. However, despite their ability to deliver high structural performance these types of composite materials do not have optimum recyclability and biodegradability. In order to eliminate these shortcomings, the application of natural fibers reinforced composite materials has been proposed in the literature (Sanjay et al., 2013; Holbery and Houston, 2006). Some of the advantages of using natural fibers over synthetic fibers are their worldwide availability and the ease of manufacturing since natural fiber yielding plants are mostly available in nature in stringy forms. A wide variety of natural materials were reported to have the capability of serving as fiber reinforcement in composites. Some of the most frequently mentioned natural materials in the literature are hemp, jute, kenaf, sisal and banana leaf. Especially kenaf differentiates itself in this group of materials because of its abundant availability, low water usage and high absorption of carbon dioxide.

Synthetic fiber reinforced composite plates have been mainly used as shell structures in aerospace, automotive and construction industries. On the other hand, due to the advancements in the natural fiber reinforced composite technology, these novel materials are being considered as viable replacements for synthetic composites in structural applications. Since buckling is a major failure mode of shell structures the buckling load is widely used as a performance indicator for this type of structural member. Therefore, the buckling response of natural fiber reinforced composites must be assiduously investigated in order to make a large-scale deployment of these materials in the industry possible. In this study the buckling behavior of glass fiber reinforced laminated composite plates has been compared to laminates with various types of natural fiber constituents.

---

* *Corresponding author.* E-mail address: cakiroglu@tau.edu.tr (C. Cakiroglu)

ISSN: 2149-8024 / DOI: https://doi.org/10.20528/cjsmec.2021.02.001

2. Mechanical Properties of Natural Fiber Reinforced Composites

Akil et al. (2011) presented an overview of the general characteristics and the application of kenaf fibers as a composite constituent (Fig. 1). In this work kenaf was put forward as an alternative to replace glass as the fiber reinforcement because of the high energy consumption associated with the glass fiber production. Nishino (2004) reported that the energy needed to produce 1kg of kenaf is 15MJ while the energy required to produce 1kg of glass fiber is 54 MJ. Moreover, it was observed that within three months of sowing the seeds kenaf plants are able to grow to a height of more than 3m and a base diameter of 3 to 5 cm under various weather conditions (Aziz et al., 2005). Because of these circumstances kenaf as a fiber material has obvious economic and ecological advantages over glass. The mechanical properties of kenaf reinforced composites were studied by various researchers. Some of the factors that affect the mechanical properties such as ultimate tensile strength or flexural modulus of the fiber reinforced composites are the type and orientation of the fibers (unilateral or randomly oriented) as well as the fiber volume fraction and the type of resin in which the fibers are embedded. Ochi (2008) investigated the mechanical properties of biodegradable composites with unidirectional fibers made of kenaf and a PLA (polylactic acid) matrix. The kenaf used in the fabrication of the biodegradable composites was cultivated in two different ambient temperatures (22°C and 30°C) and the effect of the ambient temperature on the tensile strength of the fibers was studied.

Fig. 1. Kenaf plants (Akil et al., 2011).

In addition to the effect of the ambient temperature also, the effect of the location of the fiber on the plant i.e. its distance from the root was studied by dividing the kenaf in 500 mm sections and testing each section separately. Besides the effect of the ambient temperature on the mechanical properties of kenaf also its effects on the growth of kenaf was examined. It was observed that at the end of 168 days, the height of kenaf grown in a 30°C environment was on average 1650 mm taller than kenaf grown in a 22°C environment. Moreover, the kenaf fibers taken out of the longer rods grown at 30°C were observed to have greater tensile strength and elasticity modulus compared to the fibers taken out of shorter rods. A comparison of the average tensile strength of the fibers taken from the top 500 mm and bottom 500 mm of the kenaf rods showed that the tensile strength of the top fibers is 80% of the tensile strength of the bottom fibers. Because the fiber tensile strength was found to be increasing with ambient temperature and inversely proportional to the distance from the roots, only fibers taken from the bottom portions of the kenaf rods cultivated at 30°C were used in the fabrication of kenaf fiber reinforced composite specimens that were tested in (Ochi, 2008). The kenaf/PLA composites were found to have tensile and flexural strengths of 223 MPa and 254 MPa respectively. These values are in the same order of magnitude with glass fiber reinforced composites (GFRP) (Naresh et al., 2018). In the experiments of Nishino et al. (2003) the Young's modulus of kenaf/PLA (poly-lactic acid) composites was observed to be comparable to the Young's modulus of synthetic fiber reinforced composites. The average fiber direction Young's modulus of the kenaf reinforced composites in these experiments was reported as 6300 MPa whereas the Young's modulus in the direction perpendicular to the fibers was on average 1500 MPa. Andre et al. (2016) studied the effect of kenaf fiber volume fraction on the tensile strength and the Poisson's ratio of the composites. It was observed that the highest tensile strength and Poisson's ratio occurs at a volume fraction of V_f=0.42. According to the research data collected by multiple researchers in the field (Andre et al., 2016; Ku et al., 2011), a volume fraction around 0.4 is a limit value after which the tensile strength of the composite material begins to decrease since the matrix is not filling the gaps between the fibers properly at these higher volume fraction values (Sawpan et al., 2013;

Dent et al., 2008). In the research carried out by Andre et al. (2016), the modulus of elasticity (E_C) and Poisson's ratio (ν_C) of the kenaf fiber reinforced composites were predicted using the equations developed by Tsai-Pagano, Manera and Cox-Krenchel. The predicted values together with the experimental outcome can be seen in Fig. 2.

Also, the predicted values of the Poisson's ratio were compared to the experimental values as shown in Fig. 3.

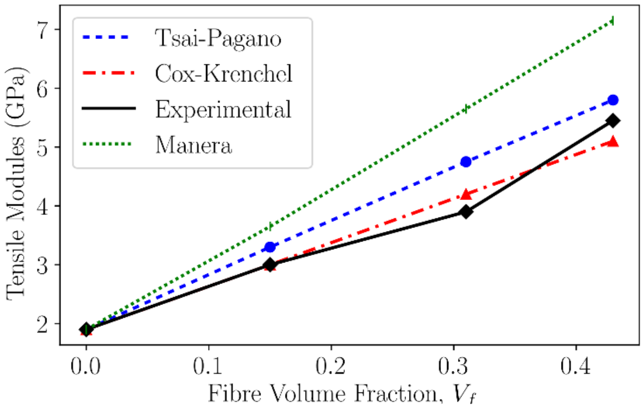

Fig. 2. Experimental and predicted tensile modulus for kenaf reinforced composite (Andre et al., 2016).

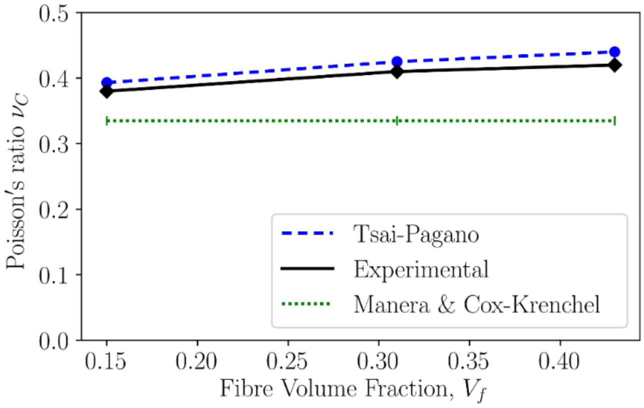

Fig. 3. Experimental and predicted Poisson's ratio for kenaf reinforced composite (Andre et al., 2016).

Another environmentally friendly fiber material that can be used in composites is flax. Oksman et al. (2003) studied the mechanical properties of flax/PLA composites (Fig. 4). In this study it was shown that as a matrix material for composites with flax fibers, PLA performs 50% better than polypropylene (PP). The elasticity modulus and tensile strength reported in the experiments of Oksman et al. (2003) were 8300 MPa and 53MPa respectively. Andersons and Spa (2016) carried out tensile experiments with composites which consist of flax fiber mats embedded in polypropylene matrix in order to determine the mechanical properties. The experiments were carried out with rectangular specimens (250 mm long and 25 mm wide) cut out of plates with 3 mm thickness manufactured for these experiments. An average elasticity modulus of 8700 MPa was measured in these experiments. Pozzi and Sepe (2012) also carried out tensile tests with flax fiber reinforced polymers in order to determine the elasticity modulus, tensile strength and Poisson's ratio. In these experiments a tensile modulus of 7882 MPa and a tensile strength of 103 MPa were measured. The Poisson's ratio was observed to vary with the flax fiber orientation angle in a range from 0.24 to 0.51.

Fig. 4. Flax fibers (Oksman et al., 2003).

Another natural fiber material that was examined in the literature is hemp. Sawpan et al. (2013) carried out tensile tests with hemp fiber reinforced UPE (unsaturated polyester) composites which is a type of natural composite that possesses low density and good stiffness. The result of these tensile tests can be seen in Fig. 5.

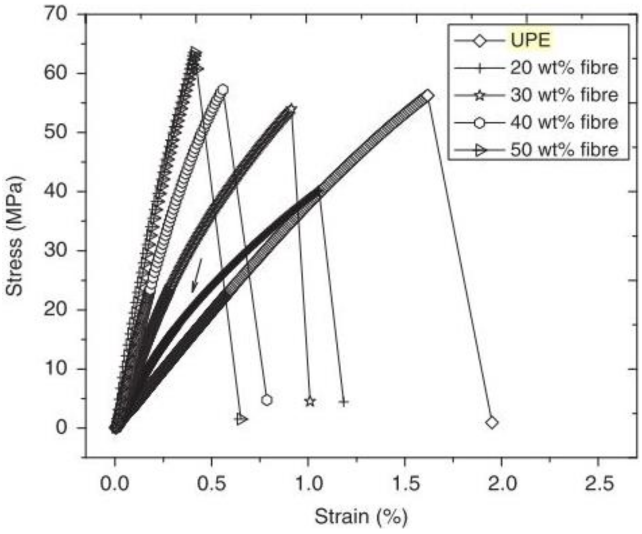

Fig. 5. Stress-strain response of hemp reinforced UPE (unsaturated polyester) compo-sites at various fiber volume fractions (Dent et al., 2008).

Fig. 5 shows the stress-strain response of hemp reinforced composites at four different levels of fiber volume fraction and the stress strain behavior of a matrix only specimen. It can be concluded from Fig. 5 that the composites with 20% fiber volume fraction have less tensile strength than the matrix only specimen, while the tensile strength tends to increase with the fiber content. The decrease in the tensile strength due to the addition of the fibers into the matrix is a subject that was investigated in the literature. (Piggott, 1994) introduced an equation that predicts the minimum fiber volume fraction ($V_{f,min}$) that leads to increased tensile properties as follows:

$$V_{f,min} = \frac{(\sigma_m - \sigma_m^*)}{(K_1 K_2 \sigma_f - \sigma_m^*)} \tag{1}$$

In this equation, σ_m is the tensile strength of the matrix, σ_m^* is the strength of the matrix at the failure strain of the fiber and σ_f is the strength of the fiber. The values recommended in the literature for the fiber orientation coefficient K_1 and the stress transfer factor K_2 are 0.2 and 0.96 respectively (Bos et al., 2006; Kalaprasad et al., 1997).

Lu et al. (2012) tested hemp fiber reinforced composites with high-density poly-ethylene matrix at fiber volume fractions between 20% and 40%. In these experiments a maximum tensile strength of 60 MPa was observed while the best mechanical properties were obtained from the composites with 40% fiber volume fraction. Moreover, the stiffness and fiber volume fraction were observed to be proportional to each other. A maximum elastic modulus of 2574 MPa was exhibited by composites with 40% fiber volume fraction. An overview of the mechanical properties of kenaf, flax and hemp fibers reported in the literature is listed in Table 1.

Table 1. Ranges of the mechanical properties of kenaf, flax and hemp fiber composites.

Fiber	Tensile strength [MPa]	Young's modulus [GPa]
Kenaf	60 – 223	1.5 – 6.3
Flax	53 – 103	8.3 – 8.7
Hemp	60 – 65	2.6 – 16.3

2.1. Mechanics of laminated composite plates

Laminated composite plates are widely used in the industry due to the advantages they offer in terms of structural performance and cost reduction. These structures consist of a certain number of layers where each layer is made of a certain type of composite material. Some of the commonly used composite materials are carbon fiber composites, boron/epoxy composites and glass fiber composites whereas natural fiber reinforced composites such as kenaf reinforced composites are a newer addition to the list of composite materials. The performance of these structures is largely determined by the fiber orientations and thicknesses of each layer.

Fig. 6 illustrates a section out of a laminated composite plate where θ_1 and t_1 denote the fiber orientation angle and the thickness of the first layer respectively. The long and short sides of the rectangular plate are denoted with a and b, and N_x denotes the compressive line load in the x-direction. The stacking sequence optimization of laminates is an extensively studied area of research (De Almeida, 2016; Cakiroglu et al., 2020) that deals with finding the optimum sequence of fiber orientation angles and ply thicknesses that deliver the best possible structural performance or the lowest cost. In these studies, mostly the buckling load is used as a measure of structural performance. The buckling load of a laminate can be computed using the eigenvalue buckling analysis procedure implemented in the finite element analysis program Abaqus.

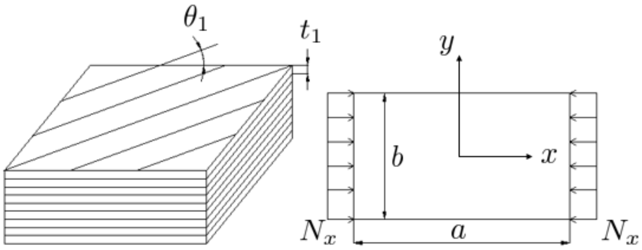

Fig. 6. Laminated composite plate under uniaxial compression.

Fig. 7 illustrates the model of a rectangular laminate with the aspect ratio a/b=2, under uniaxial compression. The finite element mesh consists of reduced integration elements and the colour map shows the displacements (U) in the first buckling mode. On each side of the plate the constrained degrees of freedom are shown with letters such that each letter indicates a constrained degree of freedom in the corresponding direction. The compressive force is applied on the plate using a unit force which increases during the eigenvalue buckling analysis incrementally and multi-point constraints (MPC). The MPC are applied in such a way that all the nodes on the right-hand side of the plate go through the same amount of displacement as the upper right corner node where the concentrated unit force is applied.

2.2. Performance comparison between fiberglass and kenaf reinforced laminated composite plates

In order to compare the performances of kenaf reinforced laminates with fiberglass composite laminates eigenvalue buckling analysis has been carried out using Abaqus. In this analysis optimized stacking sequences have been adopted from the study of Cakiroglu et al. (2020) and are listed in Table 2 for each value of the plate aspect ratio (a/b) where the angles have the unit of degrees and the layer thicknesses have the unit of millimeters. The same stacking sequences have been applied to both kenaf and glass reinforced composites for each aspect ratio.

Table 2 shows the elasticity moduli of kenaf and glass reinforced composites where E1 denotes the elasticity modulus in the fiber direction and E2 denotes the elasticity modulus in the direction perpendicular to the fibers. The stacking sequences for the fiber angles and the ply thicknesses listed in Table 2 are the optimum stacking sequences for 9 layered fiberglass laminates of different aspect ratios obtained through harmony search optimization. It can be seen that the GFRP plate performed on average 4.37 times better than the kenaf reinforced plate in terms of buckling load. The comparison of the two materials in terms of buckling load is also visualized in Fig. 8.

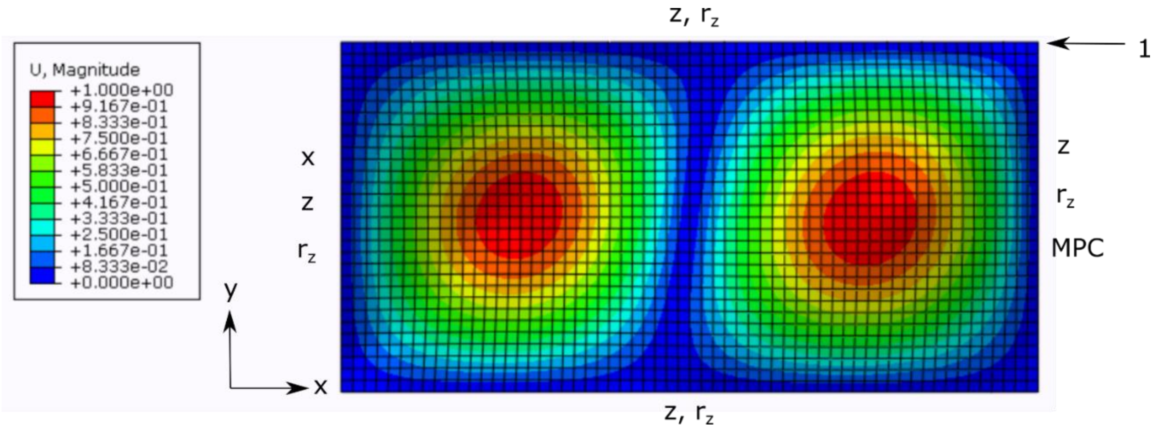

Fig. 7. Boundary conditions in the eigenvalue buckling analysis.

Table 2. Young's modulus and buckling load values for kenaf and glass reinforced composites.

Fiber	Kenaf	Glass	Fiber orientation angle sequence	Ply thickness sequence
*E*1 [MPa]	6300	33000		
*E*2 [MPa]	1500	3100		
Buckling load [N] for *a*/*b*=1	969	4201	[-53, 34, 49, 20, 61, -76, -29, 38, -45]	[0.32, 0.1, 0.22, 0.1, 0.11, 0.78, 0.1, 0.42, 0.1]
Buckling load [N] for *a*/*b* =2	964	4237	[41, 50, -50, -16, -83, 40, 62, -51, -34]	[0.1, 0.17, 0.43, 0.1, 0.45, 0.63, 0.1, 0.16, 0.1]
Buckling load [N] for *a*/*b* =3	962	4210	[49, -47,68, 45, -66, 60, 52, -36, -42]	[0.2, 0.26, 0.38, 0.26, 0.1, 0.3, 0.42, 0.1, 0.22]

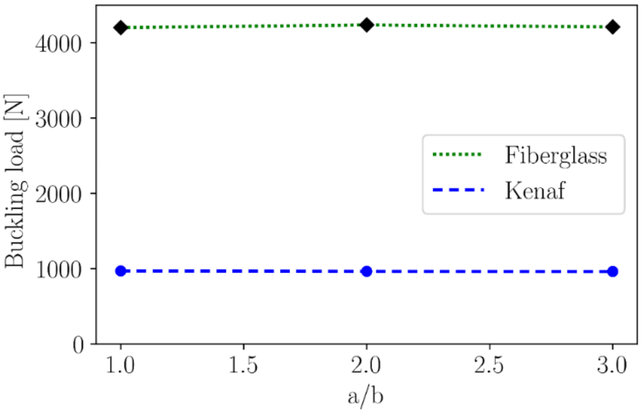

Fig. 8. Variation of the buckling load with the aspect ratio.

3. Conclusions

The low cost, abundant availability and eco-friendliness of natural fiber reinforced composites lead to an increased interest in this field in the recent years. Especially the high CO2 consumption by the natural fiber producing plants and their easy bio-degradability makes natural fibers an attractive material that can be used in structural applications. On the other hand, a large-scale industrial adoption of these natural composite materials requires a meticulous investigation into the mechanical properties of these materials. One of the most significant challenges in manufacturing with natural composites reliably is that the mechanical properties of natural fibers can exhibit randomness and wide variability. This wide variability is also evident from the large differences in the values of mechanical properties reported in the literature (Yukseloglu and Yoney, 2016). Further causes of variability in the mechanical properties of natural composites are the material selected for the matrix of the composite and the fiber volume fraction.

Although using natural composites in lightweight structures has many advantages, the wide variability in the documented mechanical properties of these natural materials makes numerical modelling and simulation of structures made of natural composites a challenging task. A major limitation of the current study is the scarcity of documented experimental research data about the material properties of natural fiber reinforced composites. Further research in this field can be carried out by investigating the buckling behavior of natural fiber reinforced composites under different loading conditions such as multi-directional compression and shear loading. Also, the effect of introducing cut-outs into the plate geometry can be investigated.

Publication Note

This research has previously been presented at the 6th International Conference on Harmony Search, Soft Computing and Applications (ICHSA 2020) held in İstanbul, Turkey, on July 16-17, 2020. Extended version of the research has been submitted to Challenge Journal of Structural Mechanics and has been peer-reviewed prior to the publication.

REFERENCES

Akil HM, Omar MF, Mazuki AAM, Safiee S, Ishak ZAM, Abu Bakar A (2011). Kenaf fiber reinforced composites: A review. *Materials and Design*, 32(8–9), 4107–4121.

Andersons J, Spa E (2016). Stiffness and strength of flax fiber/polymer matrix composites. *Polymer Composites*, 37(1), 915–924.

Andre NG, Ariawan D, Mohd Ishak ZA (2016). Elastic anisotropy of kenaf fibre and micromechanical modeling of nonwoven kenaf fibre/epoxy composites. *Journal of Reinforced Plastics and Composites*, 35(19), 1424–1433.

Aziz SH, Ansell MP, Clarke SJ, Panteny SR (2005). Modified polyester resins for natural fibre composites. *Composites Science and Technology*, 65(3–4), 525–535.

Bos HL, Müssig J, van den Oever MJA (2006). Mechanical properties of short-flax-fibre reinforced compounds. *Composites Part A: Applied Science and Manufacturing*, 37(10), 1591–1604.

Cakiroglu C, Bekdaş G, Geem ZW (2020). Harmony search optimisation of dispersed laminated composite plates. *Materials*, 13(12), 2862.

De Almeida FS (2016). Stacking sequence optimization for maximum buckling load of composite plates using harmony search algorithm. *Composite Structures*, 143, 287–299.

Dent ACE, Bowen CR, Stevens R, Cain MG, Stewart M (2008). Tensile strength of active fibre composites - prediction and measurement. *Ferroelectrics*, 368(1), 209–215.

Holbery J, Houston D (2006). Natural-fiber-reinforced polymer composites in automotive applications. *JOM*, 58(11), 80–86.

Kalaprasad G, Joseph K, Thomas S, Pavithran C (1997). Theoretical modelling of tensile properties of short sisal fibre-reinforced low-density polyethylene composites. *Journal of Materials Science*, 32(16), 4261–4267.

Ku H, Wang H, Pattarachaiyakoop N, Trada M (2011). A review on the tensile properties of natural fiber reinforced polymer composites. *Composites Part B: Engineering*, 42(4), 856–873.

Lu N, Swan RH, Ferguson I (2012). Composition, structure, and mechanical properties of hemp fiber reinforced composite with recycled high-density polyethylene matrix. *Journal of Composite Materials*, 46(16), 1915–1924.

Naresh K, Shankar K, Velmurugan R, Gupta NK (2018). Statistical analysis of the tensile strength of GFRP, CFRP and hybrid composites. *Thin-Walled Structures*, 126, 150–161.

Nishino T (2004). Green Composites: Polymer Composites and the Environment. Baillie C, editor. *Natural Fibre Sources*. Woodhead Publishing, United Kingdom, 49–80.

Nishino T, Hirao K, Kotera M, Nakamae K, Inagaki H (2003). Kenaf reinforced biodegradable composite. *Composites Science and Technology*, 63(9), 1281–1286.

Ochi S (2008). Mechanical properties of kenaf fibers and kenaf/PLA composites. *Mechanics of Materials*, 40(4–5), 446–452.

Oksman K, Skrifvars M, Selin JF (2003). Natural fibres as reinforcement in polylactic acid (PLA) composites. *Composites Science and Technology*, 63(9), 1317–1324.

Piggott MR (1994). Short fibre polymer composites: a fracture-based theory of fibre reinforcement. *Journal of Composite Materials*, 28(7), 588–606.

Pozzi A, Sepe R (2012). Mechanical properties of woven natural fiber reinforced composites. *ECCM 2012 - Composites at Venice, Proceedings of the 15th European Conference on Composite Materials*, Venice, Italy.

Sanjay MR, Arpitha GR, Yogesha B (2015). Study on mechanical properties of natural - glass fibre reinforced polymer hybrid composites: a review. *Materials Today: Proceedings*, 2(4–5), 2959–2967.

Sawpan MA, Pickering KL, Fernyhough A (2013). Analysis of mechanical properties of hemp fibre reinforced unsaturated polyester composites. *Journal of Composite Materials*, 47(12), 1513–1525.

Yukseloglu SM, Yoney H (2016). Natural Fibres: Advances in Science and Technology towards Industrial Applications RILEM Bookseries, 12. Fangueiro R, Sohel R, editors. *The Mechanical Properties of Flax Fibre Reinforced Composites.* Springer, Dordrecht, Germany, 255–266.

CHALLENGE JOURNAL OF STRUCTURAL MECHANICS 7 (2) (2021) 64–70

Challenge Journal of Structural Mechanics

Research Article

Jaya algorithm based optimum design of reinforced concrete retaining walls under dynamic loads

Nur Eroğlu [a,*], Sena Aral [a], Sinan Melih Nigdeli [a], Gebrail Bekdaş [a]

[a] *Department of Civil Engineering, İstanbul University-Cerrahpaşa, 34320 İstanbul, Turkey*

ABSTRACT

In this study, the optimum dimensioning of a reinforced concrete retaining wall that meets the safety conditions under static and dynamic loads in terms of cost has been performed using Jaya algorithm, which is one of the metaheuristic algorithms. In the optimization process, reinforced concrete design rules and ground stress, sliding and overturn tests have been determined as design constraints for the safe design of the retaining wall. While 5 cross-section dimensions of the retaining wall are defined as the design variable, the objective function is targeted as the total cost per unit length of the retaining wall. In the study, optimum results are also presented by examining the changes of the toe projection length of the retaining wall, which is one of the design variables, narrowing between 0.2-10 m. The design variables minimizing the objective function were found via Jaya algorithm that have single-phase. In addition to achieving optimum dimensioning results in terms of safety and cost with the optimization method used as a result of the reinforced concrete design made by applying the rules of the regulation on buildings to be constructed in earthquake zones, the change in cost in seismic and static conditions was examined.

ARTICLE INFO

Article history:
Received 31 August 2020
Revised 26 October 2020
Accepted 17 November 2020

Keywords:
Cantilever retaining wall
Reinforced concrete
Jaya algorithm
Optimum design
Optimization

1. Introduction

Structural design is one of the areas of expertise of civil engineering and it is the process of manufacturing buildings in a safe, economical and aesthetic way. In this process expected from engineers is to determine the type of structure suitable for the requested use and the materials to be used by calculating the loads that the building can carry. These decisions made by the engineers based on accepted rules and experiences affect many areas such as the cost of the project, its duration, the safety of the building, its applicability, etc. If the structural design variables analysed according to the predicted critical situations are insufficient or excessive, the building is redesigned by trial and error. The intensity of this process negatively affects the design process in terms of time and cost concepts that are important for engineers. Structural optimization methods provide the opportunity to reach the optimum solution by making more tests faster than an engineer can do by hand.

Structural design engineers construct retaining walls with rigid supporting structures in order to hold the ground volume at two different levels. Engineers must calculate various loads such as active thrust behind the wall to which the retaining wall will be exposed, passive thrust in front of the wall, surcharge loads and earthquake effects during the design process. Incomplete calculation of these loads affecting the retaining walls may affect the stability of the wall negatively, and the cost of the retaining wall is not economical in unnecessary loads. The pre-dimensions of the reinforced concrete cantilever retaining walls, which are one of the rigid retaining walls, are tried to be made by benefiting from the accepted knowledge and the experience of the engineer. First of all, the initial values of the other cross-section lengths of the wall are determined by making some assumptions in certain regions by correlating with the wall height (Clayton, 2014). By calculating the static and dynamic loads that will affect the wall of the obtained size, a process consisting of many steps such overturning,

---

* *Corresponding author.* E-mail address: nuryilmaz19@ogr.iu.edu.tr (N. Eroğlu)

ISSN: 2149-8024 / DOI: https://doi.org/10.20528/cjsmec.2021.02.002

sliding and stress stability analysis of the wall and in addition to these investigations, reinforcement areas changing according to internal forces, reinforcement ratios not exceeding the limit values are performed. If the controls result is negative, the process cycle is repeated by pre-sizing according to the accepted ratios. This cycle is not a practical method, as testing all design possibilities and finding the best solution will be both a time consuming and tedious process. Structural optimization methods are used because of these difficulties.

Optimum design studies of reinforced concrete cantilever retaining walls started in the 1980s, and after the 2000s, the focus was on the applicability of metaheuristic algorithms in optimization. The optimum design of the reinforced concrete retaining wall under static loads, using Simulated Annealing (SA) algorithm inspired by the annealing of metals, has been studied on the parameters that affect the minimum cost (Yepes et al., 2008) and economic design (Ceranic et al., 2001). The optimum design of the reinforced concrete retaining wall under static and dynamic loads was made by the methods of Collision Bodies Optimization (CBO) and Democratic Particle Swarm Optimization (DPSO) (Kaveh and Soleimani, 2015). As an example of metaheuristic algorithms used in optimum design of reinforced concrete retaining wall; Particle Swarm Optimization(PSO) inspired by the search for food by flocks of birds and fish (Ahmadi and Varaee, 2009) , Ant Colony Optimization (ACO), which is found by making use of the destination ants follow on their way to food (Ghazavi and Bonab, 2011), Harmony Search (HS) Algorithm inspired by the harmony between music rhythms (Kaveh and Abadi, 2011), Big Bang-Big Crunch (BP-BC) inspired by the cosmological model in the theory of evolution of the universe (Camp and Akin, 2012), Genetic Algorithm (GA) that utilizes changes in gene sequence (Pei and Xia, 2012), Firefly Algorithm (FA) developed on the basis of brightness-sensitive social behaviors of fireflies (Akin and Aydogdu, 2014), Teaching-Learning Based Optimization Algorithm (TLBO) inspired by a teacher's effect on students in the classroom (Rao et al., 2011), and Jaya Algorithm, which aims to achieve victory by moving away from the bad solution and approaching the good solution (Rao, 2016) can be shown. The optimum design of the reinforced concrete retaining wall under both static and dynamic loads was made by Temür and Bekdaş (2016) by applying the Teaching-Learning Based Optimization Algorithm (TLBO). There is a study using the Jaya Algorithm to design an optimum retaining wall, but in the mentioned study, the effect of the size of the surcharge load on the cost of the wall and the CO_2 emission value are examined in the mentioned study (Ozturk and Turkeli, 2019). In the literature, optimum design of reinforced concrete retaining wall under earthquake loads additional to static loads has not been encountered with Jaya algorithm.

In this study, it is aimed to design a reinforced concrete cantilever retaining wall designed in accordance with the legislation on Buildings to be built in Earthquake Zones (DBYBHY) (Ministry of Public Works and Settlement, 2007) by using Jaya algorithm, which is one of the metaheuristic algorithms, at optimum cost under static and dynamic loads. In addition, two different designs obtained for earthquake-free and earthquake situations were taken as reference and the relationship between earthquake and cost was examined. For the earthquake state design, the toe projection length limit values of the reinforced concrete retaining wall were also changed, and it was seen that the cost increased as the toe projection length limits were reduced by comparing 6 cases.

2. Design Methodology

2.1. Optimization problem

Retaining walls are exposed to vertical and horizontal loads shown in Fig. 1. External forces acting under static conditions (such as the mass of the wall (G_p, G_{on}, and G_t), soil pressures (P_{as}, Q_{as}) maintain their balance in the rest state. On the other hand, dynamic forces (P_{ad}, Q_{ad}) that occur during an earthquake can disrupt the balance and consequently cause permanent deformations in the wall. In case of extreme deformations, sliding, rotation, bending, etc. crash occurs for reasons. Retaining walls can be safely designed by performing a soil stress check on the base, a forward sliding check along the base and an overturning test at the heel of the wall to prevent collapse.

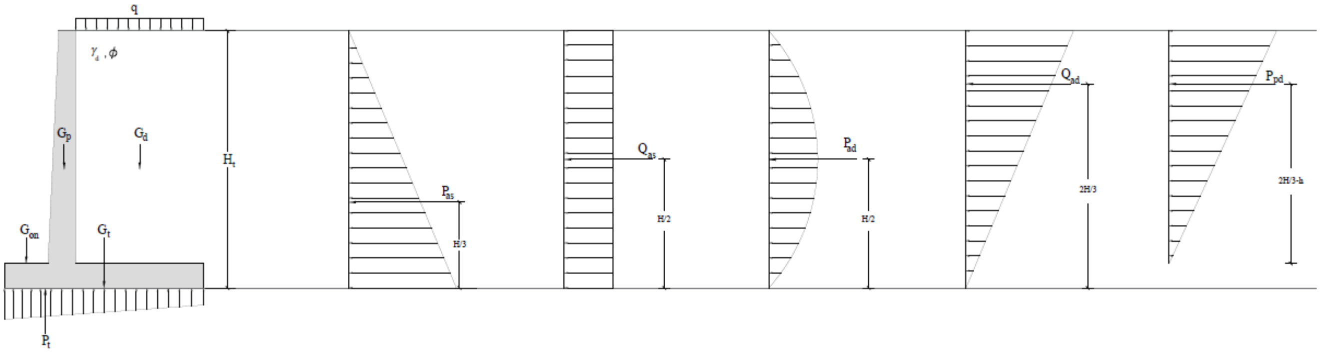

Fig. 1. Static and dynamic loads that can affect a cantilever retaining wall.

For ground stress analysis, the maximum and minimum soil stresses under the base are calculated as shown in Eq. (1). In this equation, N is the axial force, the total area A_t, the moments occurring with respect to the base midpoint M_o and the moment of resistance W_t. The largest ground stress ($\sigma_{\max}$) in the base must be smaller than the ground safety stress (σ_u) (Eq. (2)). The smallest ground stress ($\sigma_{\min}$) on the base should be designed to be positive to avoid undesired tensile stresses (Eq. (3)). In case of earthquake loading, the ground safety stress can be increased by 50% due to the earthquake acting for a limited time (Eq. (4)).

$$\sigma_{\max,\min} = \frac{N}{A_t} \pm \frac{M_O}{W_t} \tag{1}$$

$$\sigma_{\max} < \sigma_u \tag{2}$$

$$\sigma_{\min} > 0 \tag{3}$$

$$\sigma_{\max} < 1.5\ \sigma_u \tag{4}$$

The impulse from the embankment and surcharge load forces the base of the retaining wall to slide. The sliding test of the retaining wall is expressed as the ratio of the forces (F_R) against the sliding to the forces (F_O) that cause the wall to slide (Eq. (5)). The safety number (SF_S) has been accepted as at least 1.5 in granular soils and at least 1.1 under earthquake loads (Yıldırım, 2009). If the safety number is not sufficient, the safe state can be reached more economically by increasing the base width.

$$SF_S = \frac{\sum F_R}{\sum F_O} \tag{5}$$

The loads generated behind the retaining wall tend to tip the wall. The overturning safety coefficient (SF_O) is expressed as the ratio of the moments taken relative to the lower end of the toe projection to the forces (M_O) trying to overturn the system (M_R) (Eq. (6)). SF_O should only meet the condition of at least 2 under static loads and at least 1.2 under static and dynamic loads. If these conditions are not met, overturning safety can be provided by increasing the moment arm of the M_R by extending the heel projection.

$$SF_O = \frac{\sum M_R}{\sum M_O} \tag{6}$$

In the optimization problem examined in this study, five design variables were used, namely stem thickness at the top of the wall ($b1$), toe projection length ($b2$), stem thickness at the bottom of the wall ($b3$), heel projection length ($b4$) and base slab thickness (h) (Fig. 2). In the calculation of these variables, Eqs. (2-6) are considered as design constraints.

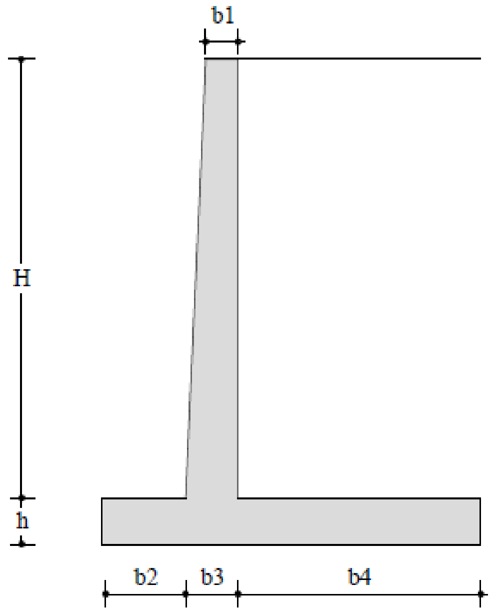

Fig. 2. Design variables of a cantilever retaining wall.

Eqs. (2-6) mentioned above are determined as design constraints. Preliminary dimensions, which are accepted in height-dependent proportions and certain limit values in cantilever reinforced concrete retaining walls, are also included in the optimization problem as a design constraint (Clayton, 2014). In addition, critical internal force (shear and bending) in the cantilever, toe and heel projection for non-earthquake and earthquake conditions were calculated and the minimum and maximum reinforcement areas were checked. Table 1 presents design restrictions.

Table 1. Restrictions on the strength of the retaining wall.

Explanation	Restricts	
	Under static loads	Under static and Dynamics loads
Safety for bearing capacity	$\sigma_{\max,\text{design}} < \sigma_u$ $\sigma_{\min,\text{design}} > 0$	$\sigma_{\max,\text{design}} < 1.5\ \sigma_u$ $\sigma_{\min,\text{design}} > 0$
Safety for sliding stability	$SF_{S,\text{design}} > 1.5$	$SF_{S,\text{design}} > 1.1$
Safety for overturning stability	$SF_{O,\text{design}} > 1.5$	$SF_{O,\text{design}} > 1.2$
Maximum reinforcement area of console section, $A_{s,\max}$	$A_{s,\text{design}} < A_{s,\max}$	$A_{sd,\text{design}} < A_{s,\max}$
Minimum reinforcement area of console section, $A_{s,\min}$	$A_{s,\text{design}} \geq A_{s,\min}$	$A_{sd,\text{design}} \geq A_{s,\min}$
Maximum reinforcement area of toe projection, $A_{so,\max}$	$A_{so,\text{design}} < A_{so,\max}$	$A_{sod,\text{design}} < A_{so,\max}$
Minimum reinforcement area of toe projection, $A_{so,\min}$	$A_{so,\text{design}} \geq A_{so,\min}$	$A_{sod,\text{design}} \geq A_{so,\min}$
Maximum reinforcement area of heel projection, $A_{sa,\max}$	$A_{sa,\text{design}} < A_{sa,\max}$	$A_{sad,\text{design}} < A_{sa,\max}$
Minimum reinforcement area of heel projection, $A_{sa,\min}$	$A_{sa,\text{design}} \geq A_{sa,\min}$	$A_{sad,\text{design}} \geq A_{sa,\min}$
Shear strength capacities ocritical sections, $V_{\max}$	$V_{\max,\text{design}} \leq V_{cr}/2$	$V_{\max,\text{design}} \leq V_{cr}/2$

Cost minimization is aimed in optimum design. In this direction, the mathematical representation of the objective function is as in Eq. (7). C_c represents the unit concrete cost, V_c represents the unit length concrete volume, C_s represents the unit reinforcement cost, W_s represents the unit length reinforcement steel weight. While C_c and C_s are independent of optimization, V_c and W_s values vary according to design variables.

$$\min f(x) = C_c \cdot V_c + C_s \cdot W_s \tag{7}$$

2.2. Optimization process

There are many types of metaheuristic algorithms used in engineering applications in the literature. Jaya algorithm, one of these metaheuristic algorithms, was developed by Rao (2016). Jaya, a word that means victory in Sanskrit, is an algorithm that aims to achieve victory by reaching the best solution thanks to the goal function obtained by multiplying the design variables with random coefficients, constantly moving away from bad solutions and approaching good solutions.

First of all, the objective function ($f(x)$) should be determined for the targeted maximization or minimization problem as in other algorithms. Population number, design variables and maximum number of iterations are essential parameters for the Jaya algorithm. Randomly generated design variables within the range of design constraints are recorded in the initial solution matrix. The size of the solution matrix is the population number determined by the designer.

The design variables produced in the initial solution matrix are reused in the iterative process using the Jaya algorithm and stored as the best solution ($f(x)_{\text{best}}$) and worst solution ($f(x)_{\text{worst}}$) values. New design variables are obtained by summing the best solution difference and subtracting the worst solution difference. The formulation of this expression is shown in Eq. (8) as the updated value of the jth variable of the kth population. Candidate solution in the ith iteration is shown as $X'_{i,k,i}$.

$$X'_{j,k,i} = X_{j,k,i} + r_{1,j,i}\left(X_{j,best,i} - \left|X_{j,k,i}\right|\right) - r_{2,j,i}\left(X_{j,worst,i} - \left|X_{j,k,i}\right|\right) \tag{8}$$

Since $r_{1,j,i}$ and $r_{2,j,i}$ are random numbers in the range of [0, 1] in the above equation, they ensure that new different solutions are obtained continuously. While $X_{j,k,i}$ is the value of the previous design variable, $X_{j,\text{best},i}$ shows the design variable values in the best solution so far and $X_{j,\text{worst},i}$ in the worst solution. If the updated variable $X'_{j,k,i}$ gives a better objective function, $X_{j,k,i}$ is replaced by $X'_{j,k,i}$. After checking for compliance with design constraints, it is recorded in the optimum solution matrix and used as input data in the next iteration.

This process is repeated until the specified stop condition is met. If the termination criteria are met, optimization is complete. The flow diagram of the Jaya algorithm is presented in Fig. 3.

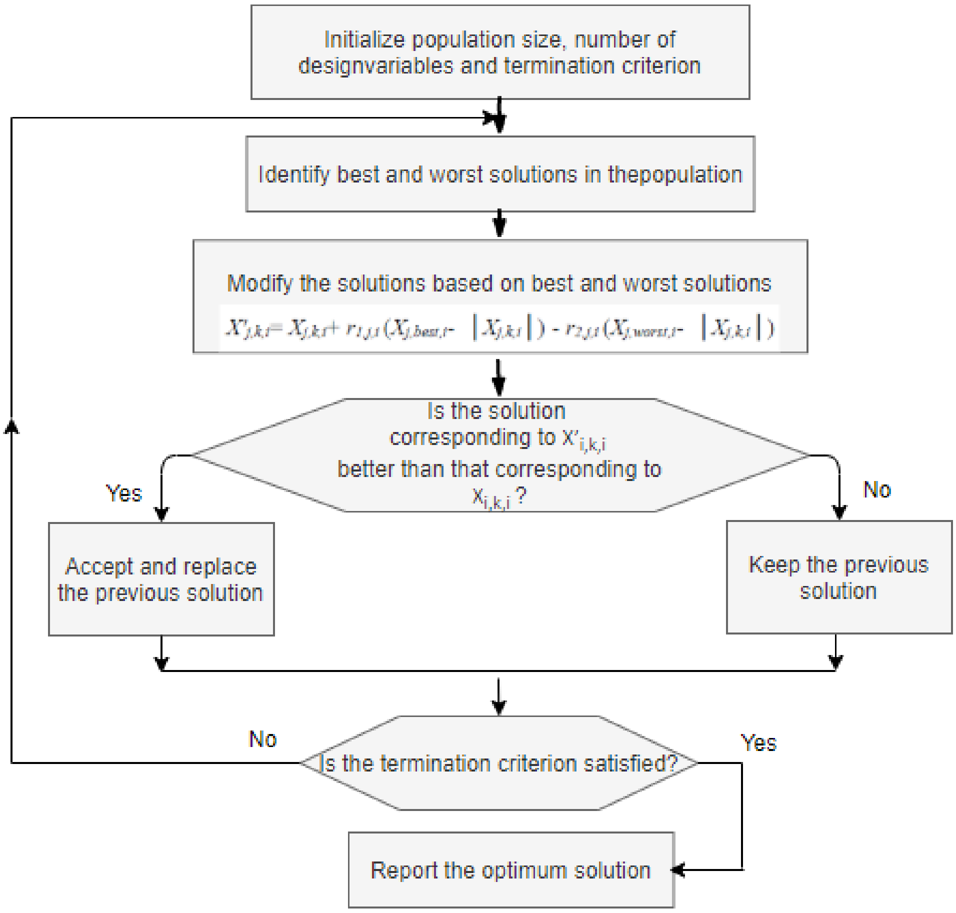

Fig. 1. Jaya algorithm flow chart (Rao, 2016).

3. Numerical Examples

The methodology has been studied for two different cases depending on static and dynamic loads. In Table 2, the design of the cantilever retaining wall (Solution 1) made by Celep (2014) was optimized using the Jaya algorithm in the first case only under static loads and named as the Solution 2. In the second case, in addition to static loads, the cantilever retaining wall was dimensioned under dynamic loads and the results were expressed as the Solution 3. The results of the design of Celep (2014) and the optimization studies made with the Jaya algorithm were compared.

Calculations are made for 1 m length of cantilever retaining wall. As the design parameters of the cantilever retaining wall in the second degree earthquake zone; the internal friction angle of the embankment is 30°, and the unit volume weight is 18 kN/m^2, the soil safety stress is 200 kN/m^2, the material class is C30/S420, the surcharge load is 5 kN/m^2 and the wall height (H) is 5.4 m excluding the floor height (h). The unit price of steel is 1400 TL/ton and the unit price of concrete is 111 TL/m^3.

The design variables are as shown in Fig. 2. The objective function changes according to the above design constants and design variables as in Eq. (7). The stop criterion (maximum number of iterations) for optimization is 100000 and the population number is 20. All dimensions, reinforcements and total costs are given in Tables 2-4, respectively.

The optimization process of Jaya Algorithm based methodology was repeated for 10 times and average results are presented in Table 5 with the standard deviation results. Since the standard deviation results are zero, the proposed methodology is robust.

Table 2. Geometric size comparison.

Variables (m)	Range (m)	Solution 1	Solution 2	Solution 3
h	0.2-3.0	0.6000	0.4480	0.4536
$b1$	0.2-3.0	0.2500	0.2000	0.2000
$b2$	0.2-10	0.9000	1.2303	1.3076
$b3$	0.2-3.0	0.6000	0.6993	0.7123
$b4$	0.2-10	3.0000	1.9760	2.1296

Table 3. Reinforcement area comparisons on console (A_s), toe projection ($A_{s,o}$) and heel projection($A_{s,a}$).

Reinforcement areas (mm^2)	Solution 1	Solution 2	Solution 3
A_s	1578.6	1278	1304
$A_{s,o}$	1080.0	776.0	787.3
$A_{s,a}$	1298.9	1156.5	1146

Table 4. Total cost comparison.

	Solution 1	Solution 2	Solution 3
Total Cost (TL/m)	2286.9	1789.7	1854.0

Table 5. Comparison of 10 runs solved by Jaya algorithm with earthquake and without earthquake cases.

Cases		h (m)	$b1$ (m)	$b2$ (m)	$b3$ (m)	$b4$ (m)	A_s (m^2)	$A_{s,o}$ (m^2)	$A_{s,a}$ (m^2)	$f(x)$ Cost (TL/m)
Without Earthquake	Avg.	0.448	0.2	1.230	0.699	1.976	1278	776	1156	1789.7
	Std.	0	0	0.0004	0.0001	0	0.0001	0.0005	0,0003	0
With Earthquake	Avg.	0.4536	0.2	1.307	0.713	2.129	1305	787.3	1146	1854
	Std.	0.0001	0	0.0004	0	0	0	0.0001	0.0003	0

In addition, the effect of toe-projection design limit change on the cost function was checked for 6 cases. In Table 6, the effect of the amendment of the toe-projection design limit on the retaining wall section dimensions; they are compared on the basis of best, average and standard deviation values.

4. Conclusions

In this study, the optimum design of the cantilever reinforced concrete retaining wall in an earthquake-free and earthquake condition has been made using the Jaya algorithm according to DBYBHY (2007) rules. In order to test the performance and success of the method, analyses aimed at optimum cost under design constraints using the Jaya algorithm were performed and compared with a retaining wall problem solved using the same design constants (Celep, 2014).

When the design cost under static loads presented by Celep (2014) was calculated according to the unit costs used in this study, 2255 TL/m was obtained. It has been observed that the design cost in non-earthquake condition obtained by the optimization method used in the study is approximately 21% (465.3 TL/m) more economical. In addition, the optimization of the cantilever reinforced concrete retaining wall was made under both static loads and dynamic loads. The design under static and dynamic loads presented by Celep (2014) was calculated as 2286.9 TL/m according to the unit costs used in this study. In this case, it was seen that the design in earthquake condition obtained by optimization was approximately 19% (432.9 TL/m) more economical. These analyzes have shown that the optimization made with the Jaya algorithm gives more efficient results.

When the analysis performed for 6 different design intervals in the toe-projection was compared, it was determined that the standard deviation increased when the design range was narrowed, and it was not robust comparing to other cases according to the multiple cycles of the optimization process.

In the study, the analysis of the reinforced concrete retaining wall under seismic and earthquake conditions was made and optimum design results were obtained. When the comparison is made according to these results, it is seen that the analysis results without dynamic loads are approximately 4% (64.9 TL/m) lower cost as predicted. Since the load will increase with the addition of dynamic loads to the static loads, it has been determined that the wall dimensions and the required reinforcement areas should be increased by approximately 1.0259. Therefore, it was understood that dynamic impulses caused the cost of reinforced concrete retaining wall to increase. Thanks to the study, the reinforced concrete section dimensions that provide the economic and safety constraints of the reinforced concrete cantilever retaining wall were calculated with the Jaya algorithm and a more efficient design was made by examining the relationship between the earthquake load and the cost of the retaining wall.

Table 6. The Effect of pre-encasement design range on optimization.

Variables	Case	$b2$ limits	$f(x)$ $*10^3$	$b1$ (m)	$b2$ (m)	$b3$ (m)	$b4$ (m)	h (m)	A_s $*10^3$	$A_{s,a}$ $*10^3$	$A_{s,o}$ $*10^3$
best	1	0.2-10	1.854	0.200	1.307	0.713	2.129	0.454	1.305	1.146	0.787
average			1.854	0.200	1.307	0.712	2.130	0.454	1.305	1.147	0.787
std. deviation			0.000	0.000	0.001	0.000	0.000	0.000	0.000	0.000	0.000
best	2	0.2-8	1.854	0.200	1.306	0.712	2.130	0.453	1.305	1.148	0.787
average			1.854	0.200	1.307	0.712	2.130	0.454	1.305	1.147	0.787
std. deviation			0.000	0.000	0.001	0.000	0.000	0.000	0.000	0.001	0.000
best	3	0.2-6	1.854	0.200	1.306	0.712	2.130	0.453	1.305	1.148	0.787
average			1.919	0.200	1.265	0.687	2.192	0.464	1.387	1.178	0.807
std. deviation			0.206	0.000	0.134	0.079	0.196	0.032	0.261	0.098	0.064
best	4	0.2-4	1.854	0.200	1.306	0.712	2.130	0.454	1.305	1.147	0.787
average			1.946	0.200	1.289	0.678	2.108	0.450	1.473	1.187	0.798
std. deviation			0.291	0.000	0.056	0.110	0.070	0.011	0.533	0.125	0.036
best	5	0.2-2	1854	0.200	1.307	0.712	2.130	0.454	1.305	1.146	0.787
average			1.930	0.239	1.377	0.700	2.092	0.481	1.345	1.166	0.843
std. deviation			0.240	0.122	0.219	0.040	0.120	0.088	0.128	0.062	0.176
best	6	0	2.792	0.200	0.000	0.712	3.477	0.754	1.304	2.795	0.000
average			2.862	0.200	0.000	0.728	3.488	0.729	1.335	2.897	0.000
std. deviation			0.221	0.000	0.000	0.050	0.036	0.078	0.100	0.321	0.000

Publication Note

This research has previously been presented at the 6th International Conference on Harmony Search, Soft Computing and Applications (ICHSA 2020) held in İstanbul, Turkey, on July 16-17, 2020. Extended version of the research has been submitted to Challenge Journal of Structural Mechanics and has been peer-reviewed prior to the publication.

REFERENCES

Ahmadi-Nedushan B, Varaee H (2009). Optimal design of reinforced concrete retaining walls using a swarm intelligence technique. *Proceeding of the First International Conference on Soft Computing Technology in Civil, Structural and Environmental Engineering*, Civil-Comp Press, Scotland.

Akin A, Aydogdu I (2014). Optimum design of retaining walls using adaptive firefly algorithm. *International Civil Engineering and Architecture Symposium for Academicians, Geotechnical Engineering*, 57-67.

Camp CV, Akin A (2012). Design of retaining walls using big bang–big crunch optimization. *Journal of Structural Engineering*, 138 (3), 438-448.

Celep Z (2014). Introduction to Earthquake Engineering and Earthquake Resistant Building Design. İstanbul, Turkey, 299-305.

Ceranic B, Freyer C, Baines RW (2001). An application of simulated annealing to the optimum design reinforced concrete retaining structure. *Computers & Structures,* 79, 1569-1581.

Clayton CRI (2014). Earth Pressures and Earth Retaining Structures. Third Edition, CRC Press, London and New York, UK and USA.

Ghazavi M, Bonab SB (2011). Optimization of reinforced concrete retaining walls using ant colony method. *ISGSR 2011-Vogt, Schuppener, Straub and Bräu (eds.),* 297-305.

Kaveh A, Abadi ASM (2011). Harmony search based algorithms for the optimum cost design of reinforced concrete cantilever retaining walls. *International Journal of Civil Engineering,* 9(1), 1-8.

Kaveh A, Soleimani N (2015). CBO and DPSO for optimum design of reinforced concrete cantilever retaining walls. *Asian Journal of Civil Engineering*, 16(6), 751-774.

Ministry of Public Works and Settlement (2007). Principles about Buildings to be made in Earthquake Zones. Ankara, Turkey.

Öztürk HT, Türkeli E (2019). Optimum design of reinforced concrete retaining walls with a key section at the base with the algorithm of Jaya. *Polytechnic Magazine*, 22(2), 283-291.

Pei Y, Xia Y (2012). Design of reinforced cantilever retaining walls using heuristic optimization algorithms. *Procedia Earth and Planetary Science,* 5, 32-36.

Rao RV, Savsani VJ, Vakharia DP (2011). Teaching-learning based optimization: a novel method for constrained mechanical design optimization problems. *Computer-Aided Design*, 43(3), 303-315.

Rao R (2016). Jaya: a simple and new optimization algorithm for solving constrained and unconstrained optimization problems. *International Journal of Industrial Engineering Computations*, 7(1), 19-34.

Temur R, Bekdaş G (2016). Teaching learning-based optimization for design of cantilever retaining walls. *Structural Engineering and Mechanics,* 57(4), 763-783.

Yepes V, Alcala J, Perea C, Gonzalez-Vidosa F (2008). A parametric study of optimum earth-retaining walls by simulated annealing. *Engineering Structures*, 30, 821–830.

Yıldırım S (2009). Soil Investigation and Foundation Design, Birsen Publishing, İstanbul, Turkey.

CHALLENGE JOURNAL OF STRUCTURAL MECHANICS 7 (2) (2021) 71–83

Challenge Journal of Structural Mechanics

Research Article

Evaluating the effects of different slab types on static and dynamic characteristics of structures

Yılmaz Keleş [a], Hüseyin Kasap [a], Zeynep Yaman [a,*]

[a] *Department of Civil Engineering, Sakarya University, 54187 İstanbul, Turkey*

ABSTRACT

In this study, the effect of different types of slabs on dynamic characteristics of structures under the lateral loading was investigated. For this purpose, four different types of slabs namely, beamed slab, flat slab, one way ribbed (hollow core) slab and waffle slab have been modeled in buildings having 3, 4 and 5 storeys with the same geometric dimensions, in accordance to design and construction requirements (TS 500) and Turkish building seismic codes (TBDY, 2018). Seismic analysis calculations of the modeled buildings were done using the equivalent seismic load method. The assumed local soil class was taken from the geotechnical report as ZD. As a result of the analysis, natural periods, base shear forces, maximum horizontal displacements and relative storey drifts of the buildings were compared. Seismic analysis and calculations of the buildings were completed using SAP2000 finite element software.

ARTICLE INFO

Article history:
Received 26 October 2020
Revised 17 December 2020
Accepted 20 January 2021

Keywords:
Beam slab
Flat slab
Ribbed slab
Waffle slab
Natural frequency
Base shear force
Storey drift

1. Introduction

Due to the fact that our country has active fault line lines, there have been many casualties of life and properties in the structures that have been destroyed or damaged by the earthquake. Reducing damages and destructions caused by earthquake can only be achieved by designing and constructing structures with high resistance to loads caused by earthquake. Design codes and specifications are set in order to prevent or reduce the loss of lives and assets due to the frequent occurrence of earthquake in our country. In spite of the frequent revisions of the Seismic design codes that are mandatory part of constructing new buildings, unfortunately, there has been no effective result that will significantly reduce the loss of life and property in case of an earthquake disaster. The Turkish Building Seismic Codes (TBDY, 2018) which was prepared by the commission created by AFAD was published as a draft in 2016. Following some arrangements in its contents, was published in the Official Gazette on March 18, 2018 and subsequently enforced as of January 1, 2019. TBDY (2018) has been prepared in line with the developments in earthquake engineering, taking into account the increasing and/or changing needs of our country. The most common and preferred types of structures in our country are reinforced concrete structures. The reason why reinforced concrete structures are preferred compared to other types of buildings is their longer useful life, the availability of concrete raw material, and higher resistance to earthquake loads. Structural members such as columns, beams, slabs and walls act as load bearing elements in reinforced concrete structures. The slab being one of the main load bearings in the structure is important in determining static and dynamic characteristics of the structure.

Different methods are used to find the optimum solution in building design. Shake tables and finite element modeling are two of the main solutions in determining dynamic characteristics (Ağcakoca, 2019; Sümer and Aktaş, 2015). Different methods are used in literature to properly understand the dynamic behavior of the building (Bilgin and Uruçi, 2018; Paripour et al., 2018; Martinez and Ventura, 2016). The characteristic behavior of the structure can be determined by estimation methods such as Arma-Arx (Uyar and Ağcakoca, 2020a, 2020b)

---

* *Corresponding author.* Tel.: +90-264-295-5744 ; Fax: +90-264-295-5601 ; E-mail address: zdyaman@sakarya.edu.tr (Z. Yaman)

ISSN: 2149-8024 / DOI: https://doi.org/10.20528/cjsmec.2021.02.003

and Artificial Neural Networks (Çağlar et al., 2008). In this study, the effects of different slab types on dynamic characteristics of the building is evaluated using finite element modeling method.

By using different slab types in the design of reinforced concrete structures, alternative design options can be considered for the same building system. Different slab types transfer the vertical and horizontal loads to the members differently. In addition, changing the slab type will cause changes in the earthquake parameters affecting the load bearing system. The most important factor in dissipating earthquake energy is the ductility capacity of the load bearing system.

During the design phase, it is important to maintain level of ductility of the building between the boundary values allowed by the design codes while determining the type of slab to be used in the structure. Moreover, slab type selection is important in determining the safety level of the load bearing system according to the Turkish seismic codes TBDY (2018). Therefore the slab types to be used in the load bearing systems and their performance mechanism should be correctly defined by the design engineers.

1.1. Previous research

Bansal and Patidar (2016) used beam slab and waffle slab in their work. They designed 4, 8 and 12 story buildings with a floor height of 3.6 m and building floor area of 20x20 m. The structures that were subjected to seismic load were examined for the changes in base shear forces, storey drift and maximum displacements using static pushover analysis. Bhina et al. (2013) compared the costs of flat slabs and beam slabs and their behavior under lateral load. They used static pushover analysis, time history and response spectrum analysis in order to assess the performance of both structures.

A study by Çağlarım (2002), has examined the effect of different types of slabs on structural behavior of rigid and ductile slab diaphragms. Rigid and ductile diaphragm were examined considering A2 and A3 modelling. Demirok (2009) investigated the effects of three different types of slab on the bearing system in a 10 storey building with the architectural features designed according to DBYBHY-2007 and compared the results. With regards to the periods in both directions, the largest period values were seen in the building model with flat slab. As for the displacements, the building model with ribbed slab had 32% more displacement in X direction and 38% more displacement in Y direction comparing to building models with beam slab.

El-Shaer (2013), has modelled a 30-storey building having concrete load bearing system with different slab systems namely, beam slab, flat slab and ribbed slabs in order to compare the storey drift, building overturning moments and base shear forces. Moreover, Özlü (2015) has evaluated a building consisting of three different bearing systems (frame, shear wall frame and shear wall) which was designed according to the Turkish seismic codes (DBYBHY-2007). They used traditional slab, filled beam slab and flat slab with different floors as 10, 15, 20, 25, 30, 35, 40 and 50. Different loading and different concrete classes were evaluated according to different floor classes in the designed structures. The load bearing system behaviors were examined by comparing the maximum displacements and maximum storey drift in both directions, secondary moment values, natural periods, and torsional and stiffness irregularity coefficients.

In a study conducted by Yaşaroğlu (2015) in which they designed an architectural plan with different slabs and different bearing systems according to Turkish seismic codes (DBYBHY, 2007). The 6 storey building was designed with frame and shear wall frame and the 12 storey building was designed with shear wall frame using the ETABS finite element analysis package. Structure weight, natural period and base shear forces were compared in the study. In all models, the largest base shear force, structure weight and natural period was obtained in buildings modeled with flat slab.

Yeşilyurt (2016); in his thesis study looked into 18 different multi-storey reinforced concrete structures with different bearing and slab systems under seismic loading using ETABS finite element program. The structural behaviors of these buildings were examined using mode superposition and design spectrum methods. The selected bearing systems were frame, tube and shear wall-frame systems, and slab systems were determined as beam slab and Ribbed (hollow core) slabs. The obtained base shear forces, maximum displacements, maximum bending moments, maximum shear forces and natural periods were compared.

The bending behavior of different slab types such as ribbed slabs has been examined. Using such slabs decreases material consumption and improve the insulation properties which enhances the sustainability of the structures (Alfeehan et al., 2017). Lastly, a parametric study has been done for the optimum solution of cantilever retaining walls such as slab (Uray, 2019), earth-retaining walls (Yepes et al., 2008), and reinforced concrete columns (Bektaş and Nigdeli, 2016).

2. Reinforced Concrete Slabs

Slabs are two-dimensional structural elements which have a considerably smaller thickness compared to the other two dimensions. The main role of slabs is to absorb the vertical loads and transfer them to the beams, columns and shear walls by which these slabs are supported. Additionally, slabs are responsible for transferring their own weights and the loads perpendicular to their planes to the beams or bearing members such as columns and/or shear walls by which are supported. The loads on the slabs vary a lot according to the usage purpose of the building. Therefore, considering the difficulties in calculating the loads affecting the slabs, it is assumed that the loads act uniformly on the slab. In addition, the change in the span of the slab will change the amount of load the slab is exposed to as a structural element. For small spans, simple slab types are generally used, while for large spans, more complicated systems and slab types are used (Topcu, 2019).

Slabs are mainly classified as beamed slabs, flat slabs, ribbed slab and waffle slabs according to their performance principles and supporting connections. In this study, the effect of different slab types such as flat slabs, beam slabs and ribbed slabs on the dynamic behavior of the building has been evaluated. According to TBDY (2018) Article 4.5.6.3, reinforced concrete slabs can be modeled with assumed rigid diaphragm in building plans where there are no A2 and A3 type irregularities and significant deflection in the plane will not occur. In addition to rigid diaphragm, the effect of eccentricity should also be taken into consideration during the analysis as per TBDY (2018).

Beam slabs are often preferred in residential buildings. They can be attached to the beam at least on one side (for example balcony slab) and can be supported by the beams on all four sides. Generally, the thickness of the beam slab is from 12 to 20 cm. Beam slabs are divided into two types namely one way slab and two way slabs based on the ratio of long span to the short span. If the ratio of the length of the slab (long span) to the width of the slab (short span) is equal to or more than 2, then it is called One way slabs. If that ratio is smaller than 2, then it is called two way slab. While one way slab are cost effective if span is short and the beam goes in one direction, but are not cost effective if the span is large. Additionally, in one way slabs, reinforcement calculations are made for only short spans, and these reinforcements are placed in the short span direction. For the long span, reinforcements are placed as per the design codes without any calculation. The main reason of placing these reinforcements is to absorb the additional stresses caused by freeze and thaw action as well as shrinkage (Topcu, 2019).

The ribbed (hollow core) slabs are formed by placing ribs parallel to each other which are then connected to main beam and have a thin plate over the ribs. Ribbed slabs can be considered as an alternative due to the fact that beamed slabs are not economical in structures with large spans. Practically, the thickness of the plate over ribbed slabs is generally 7-10 cm. The rib width is 10-20 cm and rib height is 32-50 cm. The space between each rib according to TS 500 is usually 40-70 cm. Dead and live loads on the thin plate are transferred to the ribs which then transfer them to the main beams. The most important point to consider is the direction of the ribs. If the ribs are arranged in the direction of the short span then the rib opening becomes small which is not a problem for the ribs but will cause big shear force and moment on the main beams. However, if the ribs are arranged in the direction of the long span, the ribs will be long in length causing to produce big shear force and moment in them and will not affect the main beams. Since the stiffness of the main beams, is already low in practice, it is not desirable to force the main beams too much, so ribs are generally arranged in long span direction in practice.

Ribbed slabs running in one direction are called one way ribbed slab. Ribbed slabs running in two directions are also referred to as waffle/grid slabs in practice. In ribbed slabs, the ribs are usually filled with filling material. The most commonly used filling materials in practice are: hollow concrete blocks, hollow brick, aerated concrete and foam. These filling materials do not have any load carrying capacity, and they are only considered as a dead load in the calculations. In cases where filling material is not necessary, the spaces between the ribs can be used for installation of utilities such as HVAC or mechanical pipes. According to Topcu (2019), in systems with ribbed slabs, normal beams on outer axes with a wall under them are more suitable in terms of seismic performance

Ribbed slab with ribs in both directions carrying the load are called waffle slabs. All the principles designated for one way ribbed slabs are applicable to waffle slabs as well. Waffle slabs are often used for large spans and large spaces where columns are undesirable (parking lot, Movie Theater, etc.). Waffle slabs can be thought of as beamed slabs running in two directions, which have voids in between. In this context, it can be said that the methods valid for beamed slabs will be valid for waffle slabs as well (Doğangün, 2018).

There are no restrictions on constructing waffle slabs in TBDY (2018). Same solutions and analysis that are used for one way ribbed slabs are applicable for waffle slabs as well. Since one way ribbed slabs perform poorly when exposed to earthquake load, therefore TBDY (2018) has put quite strict restrictions on using one way ribbed slabs in order to increase its performance against seismic loading. According to TBDY (2018), it is not allowed to design one way ribbed (hollow core) slab systems for high ductility. If a one way ribbed slab systems are to be created, then a shear wall needs to be included in order to increase the system ductility and can be designed as a mixed system. A system of one way ribbed slab can only be created with columns when the ductility level can be designed normally. According to TBDY (2018), one way ribbed slab systems without using shear walls are used only in buildings that are in earthquake design classes DTS = 3 and DTS = 4, and in building usage classes, BKS = 2 and BKS = 3. In other words, they can be used in building with an importance factor 1 and 1.2. In buildings with BKS = 1, (importance factor 1.5) it is not allowed to create a ribbed slab system without including shear walls. If it is to be constructed without a shear wall, then the maximum height of the building should not exceed 17.5 meters from the top of foundation elevation (if there is a basement, the height is calculated over the shear wall upper elevation). According to TBDY (2018), the maximum building height can be up to 17.5 meters from the foundation upper elevation for the earthquake design buildings with earthquake design classes DTS = 1, 1a, 2, 2a TBDY (2018). It is recommended to fill the gaps between the ribs with lightweight filling materials instead of heavy filling materials in one way ribbed slabs in order to reduce the overall weight of the structure.

Flat slabs are the structural elements that allow the loads acting on them to be transferred directly to the columns and/or shear walls since there are no surrounding beams. The most important problem in flat slabs is the risk of punching shear around the column. To prevent this, caps (column heads) are used between the column and the slab. In tensile-free slabs, the prime tensile stresses in the column- slab connection areas can exceed the tensile strength of concrete and cracks occur in the direction perpendicular to these stresses. Since the principal tensile stresses are at an angle of 45° with the slab plane, the cracks are formed at an angle of 45°. As a result, the column drills the slab by punching it in a sudden and brittle manner. Formulas are given in TS500 for controlling punching shear. If punching resistance is not achieved, then, increasing slab thickness, column/shear wall dimensions, concrete quality or using punching reinforcement can be the solution (Doğangün, 2018).

According to TBDY (2018), it has become mandatory to create shear walls in buildings with flat slabs. The shear walls should be placed as symmetrical and close to the outer axes in the X and Y direction as possible in the plan. Bearing systems of buildings with flat slabs can be arranged together with columns and shear walls. There is no obligation to create it with only shear walls. However, according to TBDY (2018), in buildings with flat slabs, shear walls have to meet the capacity of overturning moments caused by seismic loads TBDY (2018). Great effects can occur in areas where the flat slabs is supported directly by shear walls. If the shear walls are arranged on the outer axes, it is recommended to connect the columns and shear walls on the outer periphery with a beam. Thus, lateral loads are transferred to the shear wall through beams. Stiffness can be increased by placing beams on the outer axes of the systems with flat slabs.

3. Modeling by TBDY-2018

The models we have developed are to be constructed in Erenler district of Sakarya province (latitude=40.7°, longitude=30.3°). At DD-2 Earthquake Motion Level, the short period map spectral acceleration coefficient required to obtain the Horizontal Elastic Spectrum is S_S and the map spectral S_1 values for 1.0 second period (Afad, 2019).

Horizontal elastic design spectral accelerations S_{ae} (T), which are the ordinates of the horizontal elastic design acceleration spectrum for any earthquake ground motion level, are defined by Eqs. (1-4) in terms of gravity acceleration (g) depending on the natural period (Fig. 1). In the equations below, S_{DS} and S_{D1} are design spectral acceleration coefficients, T is the natural period, T_A and T_B are horizontal design spectrum corner periods and T_L indicates transition period to the constant velocity zone. The value for T_L = 6 in Eq. (5) which is taken from TBDY (2018).

$$0 \leq T \leq T_A \quad \Rightarrow \quad S_{ae}(T) = \left(0.4 + 0.6\frac{T}{T_A}\right) \qquad (1)$$

$$T_A \leq T \leq T_B \quad \Rightarrow \quad S_{ae}(T) = S_{DS} \qquad (2)$$

$$T_B \leq T \leq T_L \quad \Rightarrow \quad S_{ae}(T) = \frac{S_{D1}}{T} \qquad (3)$$

$$T_L \leq T \Rightarrow S_{ae}(T) = \frac{S_{D1}T_L}{T^2} \qquad (4)$$

$$T_A = 0.2\frac{S_{D1}}{S_{DS}} \;\; ; \; T_B = \frac{S_{D1}}{S_{DS}} \;\; ; \; T_L = 6 \text{ s} \qquad (5)$$

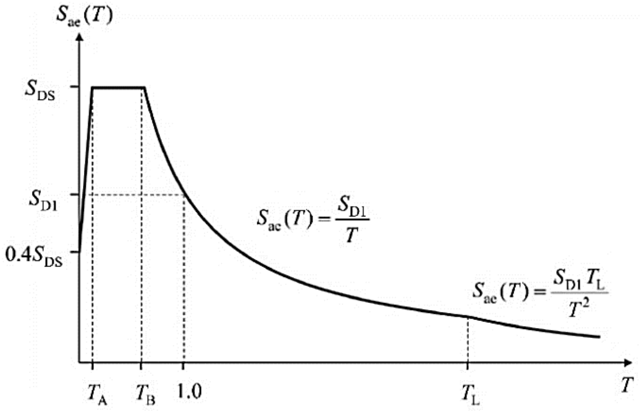

Fig. 1. Horizontal elastic design spectrum (TBDY, 2018).

The S_S and S_1 values are as follows S_S = 1.62 and S_1 = 0.444 which are mentioned in a report from Earthquake Hazard Map of Turkey. The Local Ground Impact coefficients F_S and F_1 values are obtained from assumed values in the geotechnical report for ground class ZD in the Table 2.1 of TBDY which are F_S = 1, F_1 = 1.856 respectively. In addition, design spectral acceleration coefficients: S_{DS} = 1.622, and S_{D1} = 0.824. Horizontal design spectrum corner periods T_A = 0.1202 sec and T_B = 0.508 sec. Spectral values for the locations in the vicinity of Erenler district of Sakarya province are given in Table 1. The ground class at the location where the models will be built is assumed to be ZD. The spectrum graphs obtained from the numerical data in Table 1 are shown in Fig. 2.

$$E_d^{(Z)} \cong \frac{2}{3}S_{DS}G \qquad (6)$$

The BKS = 3 which is for the buildings used for residential / business purposes was taken from Table 3.1 of TBDY (2018). The Building Importance Factor (I) in the calculations used was I = 1 for the building belonging to this usage class. Short Period, Spectral Acceleration Coefficient for DD-2 earthquake level of building models was S_{DS} = 1.622. When BKS = 3 is taken into consideration, DTS = 1 as per TBDY (2018) Table 3.2. Since the building models are without basements, building heights have been determined from the foundation's upper elevation. There are different floors in building models. Building Height Class BYS for DTS = 1 and the building height HN of the relevant building model was determined. According to TBDY, the normal performance target for DTS = 1 and cast concrete buildings in the new building is Critic Controlled Damage (CCP) and the design approach is DD-2 earthquake ground motion Design by Strength (DGT).

Load-bearing system behavior coefficient (R) and strength excess coefficient (D) within the framework of DGT are shown in Table 4.1 of TBDY (2018). According to TBDY (2018), reinforced concrete bearing systems are divided into three classes as high ductility level bearing systems, limited ductility level bearing systems and mixed ductility level bearing systems. The reduced internal forces acting in the plane of the building floors are applied strength surplus coefficient specified in TBDY Table 4.1 for the relevant bearing systems TBDY (2018).

According to Article 4.5.8.3 of the TBDY, effective cross-sectional stiffness factors are applied only under seismic effective load combinations and under the loads entering these combinations TBDY (2018).

Table 1. Earthquake parameters for DD-3 and DD-2 earthquake level.

Earthquake Level	Spectral Parameters							
	S_S	S_1	F_s	F_1	S_{DS}	S_{D1}	T_A	T_B
DD-2	1.622	0.444	1	1.856	1.622	0.824	0.102	0.508
DD-3	0.643	0.156	1.256	2.288	0.827	0.327	0.086	0.432

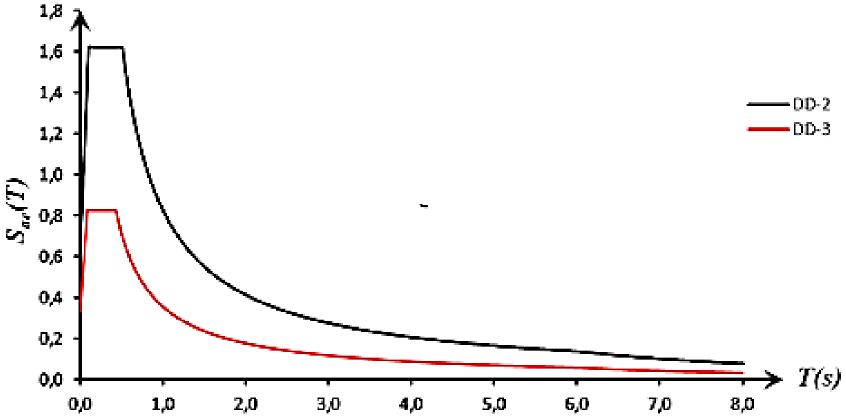

Fig. 2. Design acceleration response spectra for DD-3 and DD-2 earthquake level.

3.1. Equivalent seismic load method and floor earthquake loads

The earthquake in the X direction, the total equivalent earthquake load (base shear force), $V_{tE}^{(X)}$ is calculated as given in Eq. (7) as per TBDY (2018).

$$V_{tE}^{(X)} = m_t \cdot S_{aR}\left(T_p^{(X)}\right) \geq 0.04 \cdot S_{DS} \cdot I \cdot m_t \cdot g \qquad (7)$$

The additional equivalent earthquake load on the top floor of the building having N floors, is calculated by Eq. (8).

$$\Delta F_{NE}^{(X)} = 0.0075 \cdot N \cdot V_{tE}^{(X)} \qquad (8)$$

Earthquake loads affecting floor levels are calculated by Eq. (9).

$$F_{iE}^{(X)} = \left(V_{tE}^{(X)} - \Delta F_{NE}^{(X)}\right) \frac{m_i * H_i}{\Sigma_{j=1}^{N}(m_j * H_j)} \qquad (9)$$

The total overturning moment at the base of the building occurring from the seismic loads is calculated by Eq. (10).

$$M_O^{(X)} = \Sigma_{i=1}^{N} \cdot F_{iE}^{(X)} \cdot H_i \qquad (10)$$

Similarly, there are equivalent earthquake forces in the Y direction.

3.2. Control of effective relative storey drifts

The control of effective relative storey drift is in accordance with section 4.9.1 of the TBDY (2018). For equivalent earthquake loads in the X and Y direction, the reduced relative storey drift (Δ_i) and effective relative storey drift ($\delta_{\max}$) on all floors of the building, corner points and/or columns are calculated by Eqs. (11) and (12), respectively (TBDY, 2018).

$$\Delta_{\mathrm{i}}^{(X)} = u_i^{(X)} - u_{i-1}^{(X)} \qquad (11)$$

$$\delta_i^{(X)} = \frac{R}{I} \Delta_i^{(X)} \qquad (12)$$

The control of relative storey drift is made according to Eq. (13) of Article 4.9.1.3.a of TBDY (2018).

$$\lambda \frac{\delta_{i,\max}^{(X)}}{h_i} \leq 0.008\kappa \qquad (13)$$

In the equations: h_i = height of ith storey of building (m.), $\delta_i^{(X)}$= effective storey drift of ith floor of building column and wall for earthquake in X direction, $\delta_{i,\max}^{(X)}$= maximum effective storey drift of ith floor of building column or walls for earthquake in X direction, κ = allowable relative floor displacements coefficient used for reinforced concrete systems, R = structural system behavior factor, I = building importance factor, λ = empirical coefficient for limiting storey drifts. $u_i^{(X)}$= horizontal displacement at the ith floor for any column or wall in the X earthquake direction, and $\Delta_i^{(X)}$= reduced storey drift of *i*th floor of building column or walls in X direction.

Our building models comply with the article 4.9.1.a of the TBDY that the filler walls and facade elements made of brittle material are completely adjacent to the frame elements, without any joints between them. The value for coefficient κ is taken as 1 for reinforced concrete buildings. The λ coefficient was obtained by dividing the elastic design spectral acceleration of the DD-3 earthquake ground motion by the elastic design spectral acceleration of the DD-2 earthquake ground motion. Elastic spectral acceleration values for DD-3 earthquake ground motion were obtained by entering the same latitude and longitude values as shown in Table 2.

Table 2. Earthquake parameters for DD-3 earthquake level.

Earthquake Level	$S_{ae}\,(T^X)$	$S_{ae}\,(T^Y)$	$\lambda^{(X)}$	$\lambda^{(Y)}$	κ	I
DD-3	0.827g	0.827g	1.256	2.288	1	1

4. Finite Element Models

In this study, a structure 18 m wide and 30 m long was designed with different slab types and different number of floors. The plan consists of 6 axes in the X-X direction and 4 axes in the Y-Y direction. The lengths of all models in the plan are 30 m in the X-X direction, 18 m in the Y-Y direction and between axes distance 6 m in both directions. Plan geometry is orthogonal and symmetrical in both directions. Since the columns and shear walls are symmetrically and uniformly placed on the X and Y axes in the plan, the center of mass and the center of stiffness are coincide. The shear walls are arranged in outer plan axes to increase the torsional stiffness.

C30 concrete with a 28-day cylindrical compressive strength of 30 MPa and B420C steel with a minimum yield strength of 420 MPa were selected for all building models. In order to pre-dimension the load bearing elements of all building models, it was manually calculated under axial loads in accordance with TS 500 and TBDY (2018) codes and controlled with ideCAD-Static V10 package program.

The bearing systems of the designed models have been economically considered and have been chosen in the sizes that are frequently used in the application considering the regulations. Rules for the modeling of load carrier systems for linear calculations have been taken into consideration. The calculation models of the structures are created in three dimensions and the earthquake effect in two horizontal directions perpendicular to each other is taken into consideration. The damping ratio is taken as 5%. Earthquake calculations of all structures in the study were done with SAP2000 finite element software. Columns, beams, rib beams and waffle beams in the building models are modeled as a frame element in the SAP2000 finite element program. The slabs and walls are modeled as shell elements in the SAP2000 finite element program. Since the finite element method is an approximate method, the wall and slab elements are divided into a number of rectangular and square mesh that can be sensitive to solution. In order to ensure a healthy load flow during the modeling phase, attention has been paid to overlap the joints of the axes where the walls and columns meet the slabs. Columns and shear walls at ± 0.00 level are supported in the SAP2000 program as built-in foundation. Rules for the modeling of load bearing systems for linear calculations have been taken into consideration. The names of the buildings corresponding to the slab types are shown in Table 3.

The load-bearing system behavior coefficients of beamed slab Type A buildings, waffle slab Type C buildings and flat slab Type B buildings were taken as $R = 6$ by performing the relevant controls in the earthquake regulation. As for ribbed (hollow core) slab Type D buildings the coefficient $R = 5$ was taken according to the earthquake codes of the one way ribbed slab. The dimensions of the bearing elements of the buildings with respect to the slab types are shown in Table 4.

4.1. Design based loads and load calculations

4.1.1. Fixed loads

Structures are under the influence of fixed and dynamic (live) loads throughout their lifetime. However, structures can be exposed to different loading conditions such as impact load as well (Nasery et al., 2020; Ağcakoca et al., 2018; Al Munifi and Alameri, 2019; Al-Safi et. al., 2020). Fixed loads affecting all building models are shown in Table 5. Wall loads are given for the unit area by converting them to distributed loads in order to simplify the calculations.

Table 3. Building names according to their slab types.

Number of Floors	Slab Type			
	Beam Slab (Type A)	Flat Slab (Type B)	Waffle Slab (Type C)	Ribbed (Hollow Block) Slab (Type D)
3	Type 3A	Type 3B	Type 3C	Type 3D
4	Type 4A	Type 4B	Type 4C	Type 4D
5	Type 5A	Type 5B	Type 5C	Type 5D

Table 4. The dimensions of the bearing elements of the buildings with respect to the slab types.

Number of Floors	Building Name	Beam (cm)	Slab (cm)	Wide Beam (cm)	Rib (cm)	Column (cm)	Wall (cm)
3	Type 3A	25/60	15	-	-	50/50	650/25
	Type 3B	25/60	26	-	-		
	Type 3C	25/60	10	50/35	15/35		
	Type 3D	25/60	10	50/35	15/35		
4	Type 4A	25/60	15	-	-		
	Type 4B	25/60	26	-	-		
	Type 4C	25/60	10	50/35	15/35		
	Type 4D	25/60	10	50/35	15/35		
5	Type 5A	25/60	15	-	-		
	Type 5B	25/60	26	-	-		
	Type 5C	25/60	10	50/35	15/35		
	Type 5D	25/60	10	50/35	15/35		

Table 5. Constant load values.

Unit volume weight of reinforced concrete elements	25 kN / m^3
Plaster + Coating (normal floors)	1.5 kN / m^2
Suspended Ceiling + Installation (on normal floors)	0.5 kN / m^2
Wall Load (normal floors)	2.8 kN / m^2
Plaster + Coating (on the roof)	1.0 kN / m^2
Suspended Ceiling + Installation (on the roof)	0.5 kN / m^2

4.2. Live loads

Live loads and snow loads are determined in accordance with TS 498. All live loads and snow loads affecting building models are presented in Table 6.

Table 6. Dynamic and snow load values.

Normal floor moving load	3.5 kN / m^2
Penthouse moving load	1.5 kN / m^2
Roof snow load	1.0 kN / m^2

The ground properties of the building models are shown in Table 7. Normal floor formwork plans based on their slab types are illustrated in Fig. 3. Three-dimensional calculation models of only 4-storey buildings by slab types are shown in Fig. 4.

Table 7. Soil information of the buildings.

Soil Class	S_s	S_1	S_{DS}	S_{D1}	*PGA*	*PGV*
ZD	1.622	0.444	1.622	0.444	0.659	53.480

5. Comparison of Analysis Results

The building periods, base shear forces, maximum displacements and relative storey drifts obtained from the analyses are compared below. Earthquake load reduction coefficients in the X and Y direction used directly in the calculation of reduced design spectral accelerations corresponding to 4 different slab types are shown in Table 8.

Table 8. Earthquake load reduction coefficients.

Slab Type	3 storey		4 storey		5 storey	
	$R_a(T_X)$	$R_a(T_Y)$	$R_a(T_X)$	$R_a(T_Y)$	$R_a(T_X)$	$R_a(T_Y)$
Type A	3.678	3.678	4.340	4.35	5.146	5.173
Type B	3.823	3.940	4.539	4.629	5.428	5.511
Type C	3.699	3.706	4.367	4.381	5.166	5.208
Type D	3.420	3.519	3.903	3.952	4.493	4.503

When the slab types are compared, it can be seen from Table 9 that the earthquake load reduction coefficients increase as the number of floors increases. It is known that natural periods increase with increasing number of floors. In this context, it can be said that earthquake load reduction coefficients are directly proportional to the period. Reduced design spectral accelerations of Type A, Type B, Type C and Type D structures designed according to 4 different slab types are shown in Table 9.

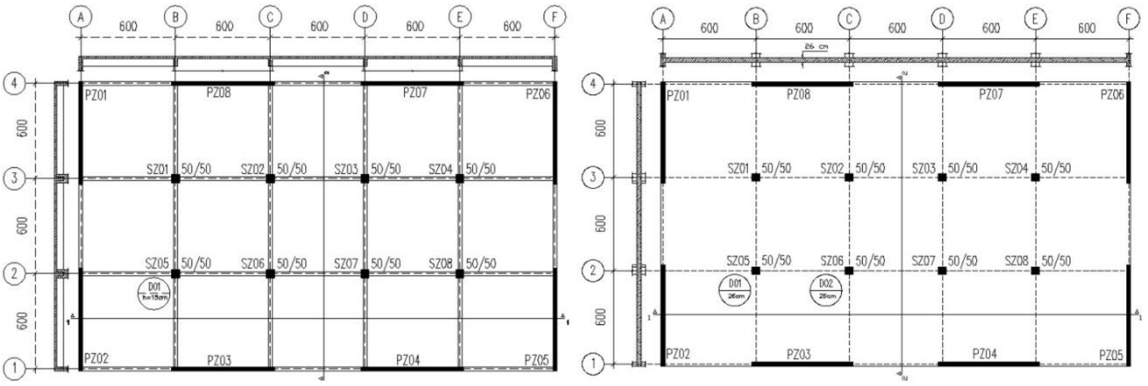

Type A Type B

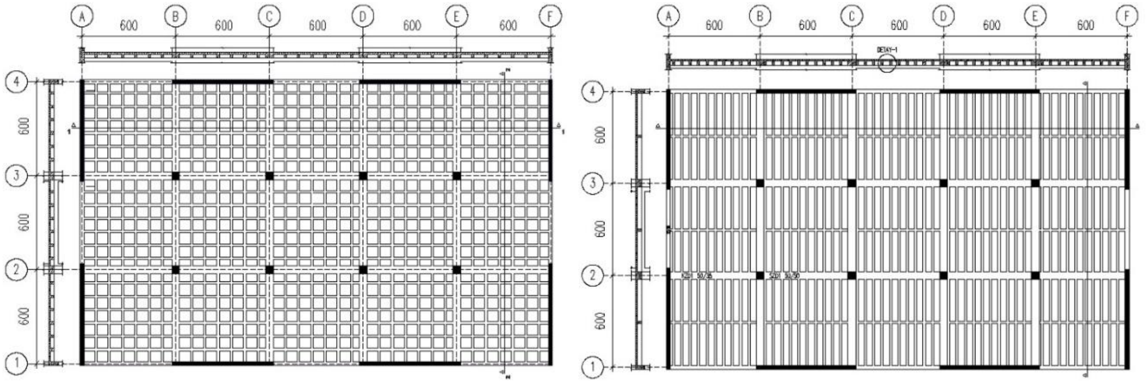

Type C Type D

Fig. 3. Formwork plan.

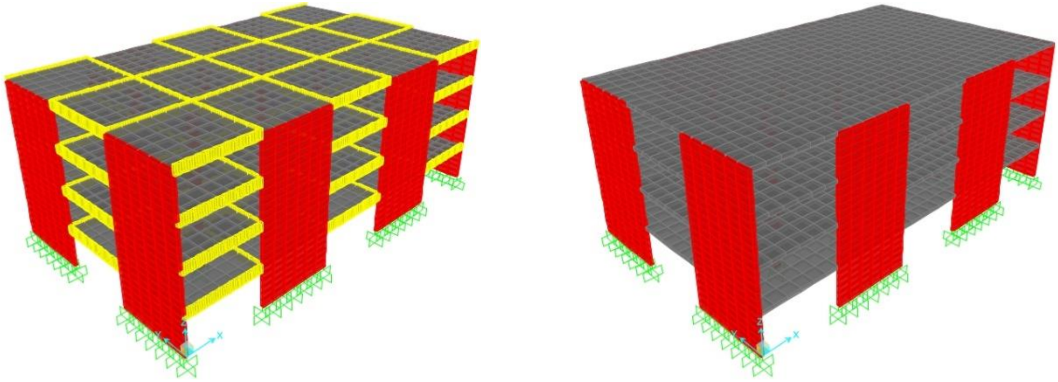

3D calculation model of the Type 4A building 3D calculation model of the Type 4B building

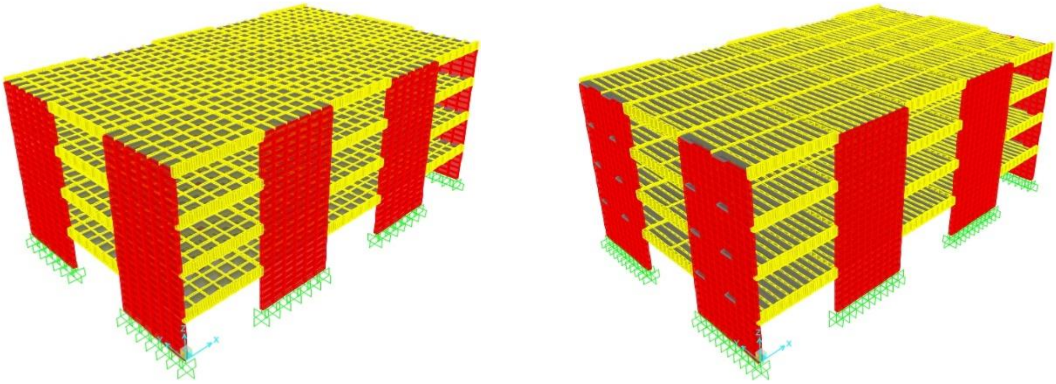

3D calculation model of the Type 4C building 3D calculation model of the Type 4D building

Fig. 4. Finite element models of buildings with different types of slabs.

Table 9. Reduced design spectral accelerations

Slab Type	3 storey		4 storey		5 storey	
	$SaR(T_X)$	$SaR(T_Y)$	$SaR(T_X)$	$SaR(T_Y)$	$SaR(T_X)$	$SaR(T_Y)$
Type A	0.441	0.441	0.374	0.373	0.315	0.314
Type B	0.424	0.412	0.357	0.350	0.299	0.294
Type C	0.439	0.438	0.371	0.370	0.314	0.311
Type D	0.474	0.461	0.416	0.410	0.361	0.360

When the slab types are compared among themselves, it is seen that the reduced design spectral accelerations decrease as the number of floors increases. The building weights of Type A, Type B, Type C and Type D building models are given in Table 10.

Table 10. Weights of structures.

Slab Type	Weights (kN)		
	3 storey	4 storey	5 storey
Type A	18403	25085	31766
Type B	21136	28778	36421
Type C	19409	26468	33527
Type D	19409	26468	33527

When the building weights given in Table 10 are compared, it can be seen that the flat slab Type B building models are the heaviest and the beam slab Type A building models are the lightest. Weights of ribbed slabs Type D buildings and waffle slab Type C buildings are almost the same. Comparing the building weights in percentage, Type B buildings with flat slabs was 13% heavier than beamed slab Type A buildings, 8% heavier compared to waffle slab Type C buildings and 8% heavier than one way ribbed slab Type D buildings. The natural vibration periods in the X and Y directions of the buildings modeled based on 4 different slab types and the number of floors are provided in Table 11.

Table 11. Natural vibration periods (sec) in X and Y directions.

Slab Type	X direction			Y direction		
	3 storey	4 storey	5 storey	3 storey	4 storey	5 storey
Type A	0.171	0.267	0.384	0.171	0.269	0.388
Type B	0.192	0.296	0.425	0.209	0.309	0.437
Type C	0.174	0.271	0.387	0.175	0.273	0.393
Type D	0.187	0.285	0.405	0.207	0.295	0.407

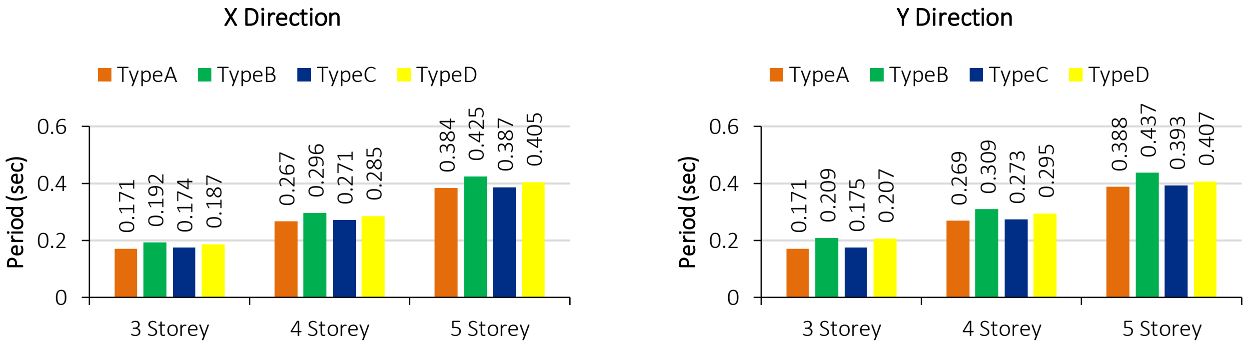

Fig. 5. Natural periods in X and Y directions.

Fig. 5 shows the comparison of natural periods in X and Y directions. Initially we compared the periods in the X direction of Type 3B (3-storey model) with different building models. We have observed that it had an 11% larger period compared to Type 3A building, 9% larger than the Type 3C and 3% larger than the Type 3D building models. Similarly, the natural periods in X direction of Type 4B building had a 10% larger period compared to Type 4A building, 8% larger than the Type 4C building and 4% larger than the Type 4D building. Finally, the natural vibration periods in the X direction of Type 5B building had a 10% larger period compared to Type 5A building, 9% larger than the Type5C building and 5% larger than Type5D building. The period of Type B building was the largest followed by type D building models in all three different storeys. Type A buildings had the smallest period in all three storeys. Next we compared the natural vibration periods in Y direction of Type 3B building with the remaining three building types. It could be seen that Type 3B had an 18% larger period compared to Type 3A building, 16% larger than the Type 3C and 1% larger than the Type 3D building models. Additionally, the natural periods in Y direction Type 4B building had a 13% larger period compared to Type 4A building, 12% larger than the Type 4C building and 5% larger than the Type 4D building. Lastly, the natural vibration periods in the Y direction of Type 5B building had an 11% larger period compared to Type 5A building, 10% larger than the Type 5C building and 7% larger than Type 5D building. Similar to the X direction, the period of Type B building in the Y direction was the largest followed by type D building models in all three different storeys. Type A buildings had the smallest period in all three storeys.

Total base shear force values in the X and Y directions, which are modeled with respect to 4 different slab types and floor volumes, are different from the horizontal earthquake forces (EXP and EYP) of Type A, Type B, Type C and Type D buildings as presented in Table 12.

Table 12. Base shear forces (kN) in X and Y directions.

Slab Type	X direction			Y direction		
	3 storey	4 storey	5 storey	3 storey	4 storey	5 storey
Type A	8115	9374	10013	8115	9354	9960
Type B	8968	10283	10883	8701	10084	10720
Type C	8511	9831	10526	8495	9800	10442
Type D	9204	11001	12103	8947	10864	12077

As it can be seen that in both X and Y directions, the largest base share forces values are in ribbed (hollow core) slab Type D building models, Followed by flat slab Type B, waffle slab Type C and beam slab Type A building models,

The lowest base shear force values can be found in the Type A building models with beam slabs, Although the building weights of Type C and Type D building models were the same, the base shear force values yielded different results (Fig. 6), This is due to the direct change of periods because of the arrangement of ribs in two directions in the plan in waffle slab systems,

Fig. 6 shows the comparison of base shear forces in X and Y directions of different types of building and with three different storeys. Initially, we compared the base shear force of Type 4D (4-storey model) with different building models. We have observed that Type 4D had a 15% bigger base shear force compared to Type 4A building, 11% bigger than the Type 4C and 7% bigger than the Type 4B building models. In addition, the base shear force in X direction of Type 5D building had a 17% larger base shear force compared to Type 5A building, 13% larger than the Type 5C building and 10% bigger than the Type 5B building. Next, we compared the base shear forces in Y direction of Type 3D building with the remaining three building types. It could be seen that Type 3D had a 9% bigger shear force compared to Type 3A building, 5% larger than the Type 3C and 3% bigger than the Type 3B building models. Additionally, the base shear force in Y direction Type 4D building had a 14% bigger base shear force compared to Type 4A building, 10% bigger than the Type 4C building and 7% larger than the Type 4B building. Lastly, the base shear forces in the Y direction of Type 5B building had a 18% bigger base shear force compared to Type 5A building, 14% larger than the Type 5C building and 11% larger than Type 5B building.

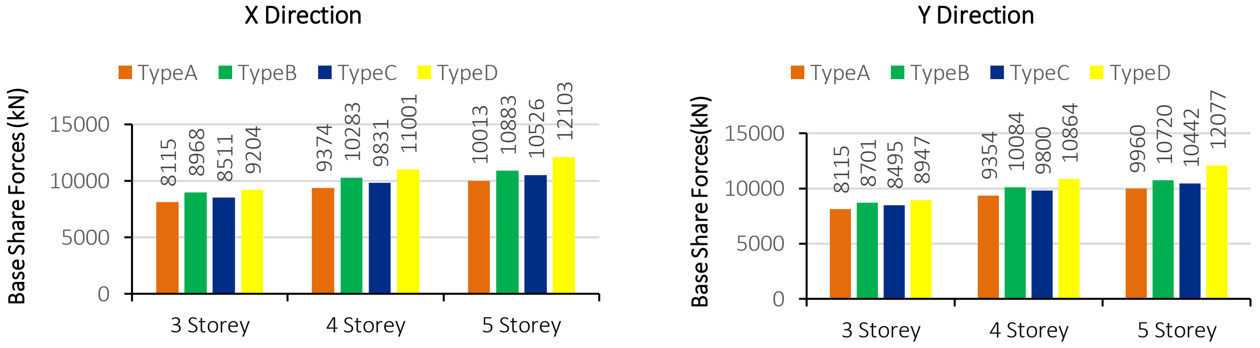

Fig. 6. Base shear forces in X and Y directions.

Maximum horizontal displacements consisting of EXP and EYP earthquake loads in X and Y directions are shown in Table 13. As seen in Table 13, the largest displacement values in the direction of X and Y are seen in the Type D building models with ribbed slabs while the smallest displacement values are in the Type A building models with beam slabs. The displacement values of the flat slab Type B and ribbed (hollow block) slab Type D buildings are close to each other as can be seen in Table 13.

Fig. 6 compares the maximum displacements in X and Y directions of the top floor of different types of building and with three different storeys. Initially, we compared the maximum displacement in X direction of top floor of Type 3D (3-storey model) with different building models. We have observed that the Type 3D had a 32% bigger maximum displacement compared to Type 3A building, 30% larger than the Type 3C and 1% bigger than the Type 3B building models. In addition, the top floor of Type 4D had a 25% bigger maximum displacement compared to Type 4A building, 24% larger than the Type 4C and 5% bigger than the Type 4B building models. Finally, the maximum displacement in X direction of top floor of Type 5D building had a 18% larger maximum displacement compared to Type 5A building, 23% larger than the Type 5C building and 8% bigger than the Type 5B building. Next we compared the maximum displacement in Y direction of top floor of Type 3D (3-storey model) with different building models. We have observed that the top floor of Type 3D building had a 9% bigger maximum displacement compared to Type 3A building and 6% larger than the Type 3C. The maximum displacements of Type 3B and Type 3D were close to each other. In addition, the top floor of Type 4D had a 10% bigger maximum displacement compared to Type 4A building and 8% larger than the Type 4C. The maximum displacements of top floor of Type 4B and Type 4D were close to each other. Finally, the maximum displacement in Y direction of top floor of Type 5D building had a 13% larger maximum displacement compared to Type 5A building, 11% larger than the Type 5C building and 3% bigger than the Type 5B building.

Control values of effective relative storey drift of the top floors of buildings in X and Y directions are shown in

Table 14. The values of relative storey drifts are compared to each other (Fig. 7). For all the building models, the ratio of effective relative storey drifts in both directions to the height of the floor was found below the limit value of 0,008 which is permitted by the design codes.

Table 13. Maximum horizontal displacements (mm) in X and Y directions.

Slab Type	X direction			Y direction		
	3 storey	4 storey	5 storey	3 storey	4 storey	5 storey
Type A	5,75	12,89	25,54	6,08	13,68	25,09
Type B	8,36	16,38	28,33	6,58	14,99	27,74
Type C	5,92	13,12	23,71	6,28	14,03	25,52
Type D	8,42	17,18	30,96	6,70	15,19	28,69

Table 14. Control of effective relative story drift in X and Y directions.

Slab Type	X direction			Y direction		
	3 storey	4 storey	5 storey	3 storey	4 storey	5 storey
Type A	0.00227	0.00399	0.00595	0.00242	0.00425	0.00638
Type B	0.00292	0.00478	0.00695	0.00262	0.00468	0.00712
Type C	0.00234	0.00403	0.00593	0.00249	0.00434	0.00644
Type D	0.00275	0.00437	0.00649	0.00219	0.00395	0.00607

Fig 8. illustrates the relative storey drifts of the top floors of all the building models in X and Y directions. Initially, we compared the storey drifts in the X direction of Type 3B (3-storey model) with different building models. We have observed that it had 22% larger storey drift compared to Type 3A building, 20% larger than the Type 3C and 6% larger than the Type 3D building models. Similarly, the storey drift in X direction of the top floor of Type 4B building had a 17% larger drift compared to Type 4A building, 16% larger than the Type 4C building and 9% larger than the Type 4D building. Finally, the storey drift in the X direction of the top floor of Type 5B building had a 14% larger storey drift compared to Type 5A building, 15% larger than the Type 5C building and 7% larger than Type 5D building. The storey drift of Type B building was the largest followed by type D building models in all three different storeys, Next, we compared the storey drifts in the Y direction of the top floor of Type 3B (3-storey model) with different building models. We have observed that it had 8% larger storey drift compared to Type 3A building, 5% larger than the Type 3C and 16% larger than the Type 3D building models. Similarly, the storey drift in Y direction of the top floor of Type 4B building had a 9% larger drift compared to Type 4A building, 7% larger than the Type 4C building and 16% larger than the Type 4D building. Finally, the storey drift in the Y direction of Type 5B building had a 10% larger storey drift compared to Type 5A building, 10% larger than the Type 5C building and 15% larger than Type 5D building. The storey drifts of Type B building were the largest and the storey drift of Type D building models were the smallest in all three different storeys,

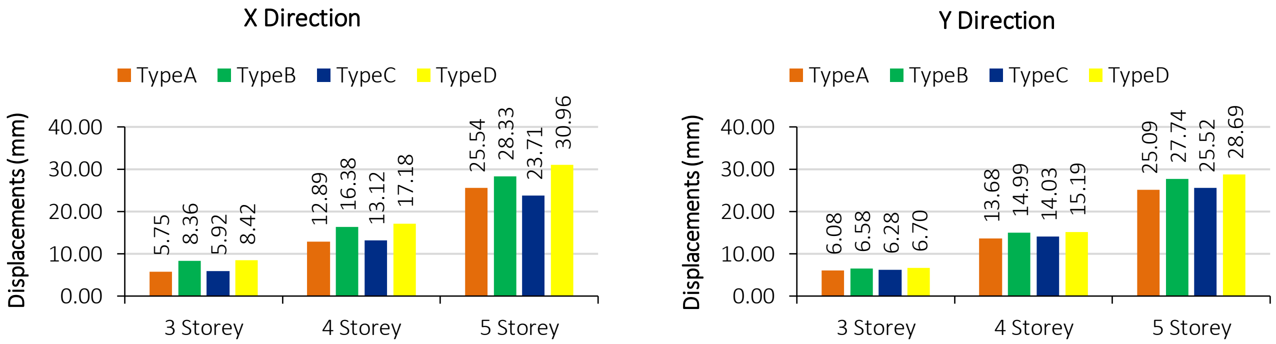

Fig. 7. Maximum lateral displacements in X and Y directions.

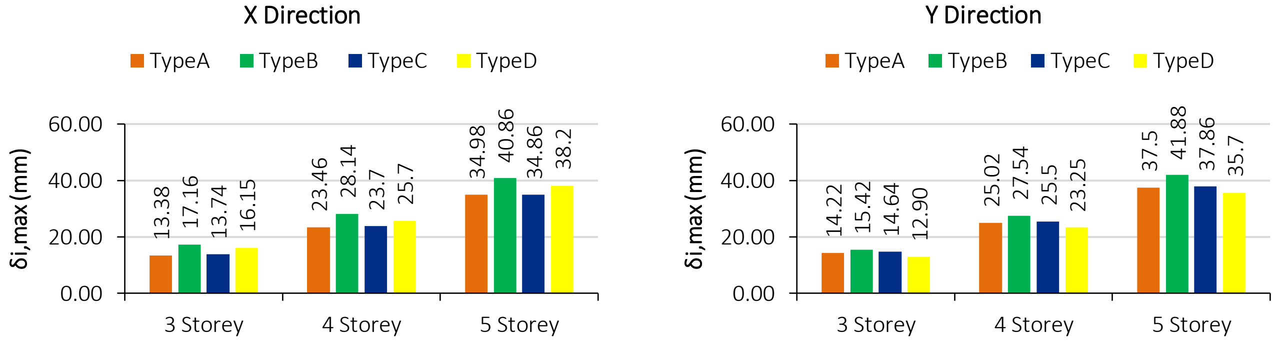

Fig. 8. Relative storey drifts in X and Y directions.

6. Conclusions

The horizontal loads that will affect the structure due to the earthquake are transferred to the carrier system elements by means of floors. During the transfer of these loads, the floor does not wrinkle and the loads can be transported properly only if the rigidity of the flooring is high. Thus, a true diaphragm behavior can be mentioned.

In the study, Earthquake calculations of model builds were analyzed by assuming full rigid diaphragm with beamed slab and waffle slab structures. Flat slab models and one way ribbed (hollow core) slab models were analyzed by assuming semi-rigid diaphragm. Rigid diaphragm behavior can be assumed in the direction of ribs in one way ribbed (hollow) slab systems. But assuming full rigid diaphragm behavior in the direction perpendicular to the ribs will give incorrect results. Therefore it is recommended to calculate such slab systems by assuming semi rigid diaphragm as a whole. Building systems can easily change shape during an earthquake as the beams is not embedded in slab, it is recommended to assume a semi-rigid diaphragm the calculations.

As we evaluated the effect of changing slab types on building natural periods, it was observed that the biggest periods in the X and Y direction were in flat slab Type B building models. The fact that the buildings with flat slabs have a big natural period is because their horizontal stiffness is less compared to other slab types. One way ribbed slabs Type D had the second biggest natural period followed by waffle slab Type C. The beam slab Type A buildings had the smallest period in all three storeys among all building models. The periods of beam slab Type A and waffle slab Type C buildings were very close to each other,

When the effect of the changing slab types on base shear forces was examined, it could be seen that the biggest base shear force values in the X and Y direction are in the Type D building models. Type B building models had the second and Type C building had the third biggest base shear forces. Type A building had the smallest base shear force,

The largest displacement values in the X and Y directions were obtained in one way ribbed slab Type D building models and the smallest displacement values were in the beamed slab Type A building models. The maximum displacement in Type B and Type D were close to each other while the maximum displacements of Type A and Type C were closes to each other.

All building models in the study were analyzed with the SAP2000 V20 finite element program according to TBDY (2018). C30/37 concrete and B420C reinforcement steel were used as materials in all analyzes. It has been accepted that the buildings will be built in Sakarya -Erenler district and the ground classes are ZD. It is assumed that all building models in the study are fixed to the foundation and foundation calculations are excluded. The effect of different slab type on the dynamic characteristics of the building can be re-examined by changing all these assumptions as material and soil type.

The buildings seismic analyzed in the study have a symmetrical plan, shear walls on the outer axes and coincide the center of mass and the center of rigidity . They have no irregularities specified in TBDY (2018). In other words, the most favorable situations have been considered. It is certain that different results will be obtained in different design styles.

The study has concluded that it is recommended to use beamed slab systems in areas with high risk of earthquakes. Frames formed by beams, columns and walls created in beamed slab, hollow slab and waffle slab systems are of great importance in terms of the horizontal rigidity of the system.

REFERENCES

Afad (2019). T.C. İçişleri Bakanlığı Afet ve Acil Durum Yönetimi Başkanlığı, Ankara, Turkey. https://tdth.afad.gov.tr/ Date of access: 12.05.2019.

Ağcakoca E (2019). Yüksek katlı yapının sarsma tablası üzerinde deprem performansının incelenmesi. *ALKÜ Fen Bilimleri Dergisi*, 1(3), 132-143. (in Turkish)

Ağcakoca E, Yaman Z, Yazıcı YE (2018). Kompozit ve kutu profilin darbe kuvveti altındaki davranışı. *Journal of New Results in Engineering and Natural Sciences*, 8, 75-83. (in Turkish)

Alfeehan A, Abdulkareem HI, Mutashar SH (2017). Flexural behavior of sustainable reactive powder concrete bubbled slab flooring elements. *Challenge Journal of Structural Mechanics*, 3(2), 81-89.

Al Munifi AA, Alameri IA (2019). The impact of design approach and contracting practices on cost and execution period of school buildings. *Challenge Journal of Structural Mechanics*, 5(3), 85-95.

Al-Safi S, Alameri IA, Badhib RA, Kuleib M (2020). Evaluation of performance-based earthquake engineering in Yemen. *Challenge Journal of Structural Mechanics*, 6(1), 10-22.

Bansal A, Patidar A (2016). Pushover analysis of multistorey buildings having flat slab and grid slab. *International Journal of Engineering Science Invention Research & Development*, 2(7), 435-441.

Bekdaş G, Nigdeli SM (2016). Optimum design of reinforced concrete columns employing teaching learning based optimization. *Challenge Journal of Structural Mechanics*, 2(4), 216-219.

Bhina MR, Banerjee A, Paul DK (2013). Assessment of different aspect of RC flat slab building over normal RC frame building. *International Conference on Structural Engineering & Construction Management* (*ICSECM,*), Kandy, Sri Lanka.

Bilgin H, Uruçi R, (2018). Effects of structural irregularities on low and mid-rise RC building response. *Challenge Journal of Structural Mechanics*, 4(2), 33-44.

Caglar N, Elmas M, Yaman ZD, Saribiyik M (2008). Neural networks in 3-dimensional dynamic analysis of reinforced concrete buildings, *Construction and Building Materials*, 22(5), 788-800.

Çağlarım M (2002). Betonarme Çok Katlı Yapılarda Döşeme Türünün Taşıyıcı Sisteme Etkileri. *Ph.D thesis*, İstanbul Technical University, İstanbul, Turkey. (in Turkish)

Demirok A (2009). Perdeli Çerçeve Taşıyıcı Sisteme Sahip bir Betonarme Yapıda Farklı Döşeme Türlerinin Davranışa Etkisi. *Ph,D thesis*, İstanbul Technical University, Istanbul, Turkey. (in Turkish)

Doğangün A (2018). Betonarme Yapıların Hesap ve Tasarımı. *Birsen Yayınevi*, İstanbul, Turkey. (in Turkish)

El-Shaer MA (2013). Seismic load analysis of different RC slab systems for tall building. *International Journal of Current Engineering and Technology,* 5(3), 65.

ideCAD Static V10 (2021). Integrated Software for Structural Analysis and Design. ideYAPI, İstanbul, Turkey.

Martinez A, Ventura CE (2016). Seismic response of a ten story concrete building subjected to different earthquakes. *Challenge Journal of Structural Mechanics*, 2(1), 60-68.

Nasery MM, Ağacakoca E, Yaman Z (2020). Experimental and numerical analysis of impactor geometric shape effects on steel beams under impact loading. *Structures,* 27, 1118-1138.

Özlü B (2015) Çok Katlı Betonarme Binalarda Taşıyıcı Sistem Türlerinin Davranışlarının Incelenmesi. *Ph.D thesis*, İstanbul Technical University, İstanbul, Turkey. (in Turkish)

Paripour MB, Budak A, Düzgün OA (2018). Numerical investigation of reinforced concrete frame behavior subjected to progressive collapse. *Challenge Journal of Structural Mechanics*, 4(3), 117-125.

SAP2000 V20 (2021). IntegratedSoftware for Structural Analysis and Design. Computers & Structures, Inc., California, USA.

Sümer Y, Aktaş M (2015). Defining parameters for concrete damage plasticity model. *Challenge Journal of Structural Mechanics*, 1(3), 149-155.

TBDY (2018). Turkey Building Earthquake Code. Disaster and Emergency Management Presidency, Ankara, Turkey.

Topçu A (2019). Betonarme-II. *Eskişehir Osmangazi Üniversitesi Mühendislik Mimarlık Fakültesi, İnşaat Mühendisliği Bölümü*, Eskişehir, https://mmf2.ogu.edu.tr/atopcu. (in Turkish)

TS498 (1997). Calculation Values of Loads to be taken in the Dimensioning of Structural Elements. Turkish Standards Institute, Ankara, Turkey.

TS500 (2000). Design and Construction Rules of Reinforced Concrete Structures. Turkish Standards Institute, Ankara, Turkey.

Uray E, Çarbaş S, Erkan İH, Tan Ö (2019). Parametric investigation for discrete optimal design of a cantilever retaining wall. *Challenge Journal of Structural Mechanics,* 5(3), 108-120.

Uyar H, Ağcakoca E (2020a). Artic determination of dynamic characteristics the structure with ARX and ARMAX estimation methods. *Sakarya University Journal of Science*, 24(3), 460-471.

Uyar H, Ağcakoca E (2020b). Sensör ve akıllı telefon kayıtları yardımı ile yapının dinamik karakteristiklerin belirlenmesi*. Iğdır Üniversitesi Fen Bilimleri Enstitüsü Dergisi,* 10(2), 1053-1065. (in Turkish)

Yaşoğlu FG (2015). Taşıyıcı sistemleri farklı olan betonarme yapılarda döşeme türlerinin davranışa etkisi. *Ph.D thesis*, İstanbul Technical University, İstanbul, Turkey. (in Turkish)

Yepes V, Alcala J, Perea C, González-Vidosa F (2008). A parametric study of optimum earth-retaining walls by simulated annealing. *Engineering Structures*, 30(3), 821-830.

Yeşilyurt A (2016). Farklı döşeme ve taşıyıcı sistemlere sahip çok katlı betonarme binaların deprem davranışlarının incelenmesi. *Ph.D thesis*, Yıldız Technical University, İstanbul, Turkey. (in Turkish)

CHALLENGE JOURNAL OF STRUCTURAL MECHANICS 7 (2) (2021) 84–92

Challenge Journal of Structural Mechanics

Research Article

Rapid power outage estimation for typical electric power systems in Turkey

Ali Yesilyurt [a,*], Seyhan Okuyan Akcan [b], Abdullah Can Zulfikar [a]

[a] *Department of Civil Engineering, Gebze Technical University, 41400 Kocaeli, Turkey*
[b] *Department of Civil Engineering, Boğaziçi University, 34342 İstanbul, Turkey*

ABSTRACT

Electric power systems have critical importance in the sustainability of social life and economy. The past and recent earthquakes showed clearly that these systems have high vulnerability due to earthquakes. In this study, the typical electric power systems which are commonly preferred and located at five different sites in high seismic zone of Turkey, Marmara region, have been examined. In the first part of the study, the earthquake hazard for Marmara region has been accomplished. The earthquake hazard curves at five different sites for two different earthquake levels, and two different site conditions as soft and stiff site classes according to the Turkish Building Seismic Design Code 2018 have been obtained. The seismic vulnerability assessment of substation and distribution circuits for two different design states, namely anchored and unanchored, achieved by the fragility functions. The probability of power outage durations have been evaluated based on the restoration curves. It has been observed that the results obtained within the scope of the study are highly consistent with post-earthquake studies in the literature. The proposed methodology through the power outage graphics enable a quick preliminary evaluation of the power outage based on the current design status and location for any electric power systems in the Marmara region.

ARTICLE INFO

Article history:
Received 4 November 2020
Revised 26 December 2020
Accepted 20 January 2021

Keywords:
Electric power systems
Seismic vulnerability
Power outage
Fragility curve

1. Introduction

Electric power systems (EPSs) are one of the critical infrastructures, exposed to threat of natural hazards, especially earthquakes. In general, EPSs contain generation facilities, substations, and distribution circuits. The EPSs are considered as the lifeline systems, which are essential for the modern life and maintaining the functionality of emergency services and other lifelines such as water supply, fuel supply, wastewater treatment, and communications. The EPSs have direct relation with the economy. An interruption in the EPSs due to an earthquake event will cause serious loss in economic and social life (Kwasinski et al., 2014). Any earthquake damage on the substations, distribution circuits and/or on their specific components will lead to disruption in the whole system. Such a disruption in the EPSs will certainly affect the commercial and industrial activities in the region (Shinozuka et al., 1999). The observations in the recent earthquakes showed that EPSs and their sub-elements, including components of high/low-voltage substations and power transmission systems, have suffered damages and subsequently stoppage in power transmission. The seismic vulnerability of these sub-elements has been studied by researchers in recent years (Watson, 2010; Massie and Watson, 2011).

Fujisaki et al. (2014) has studied seismic performance of high-voltage electric substation equipment and transmission lines after major worldwide earthquakes. He had comprehensive observations and had some component based recommendations. A significant damage was observed after the 11 March 2011 Tohoku Earthquake in Japan in the two important EPSs in their high voltage transformers, circuit breakers, air disconnects, instrument

---

* *Corresponding author.* Tel.: +90-262-605-1638 ; E-mail address: aliyesilyurt@gtu.edu.tr (A. Yesilyurt)

ISSN: 2149-8024 / DOI: https://doi.org/10.20528/cjsmec.2021.02.004

transformers and cable terminations elements. All these electric power components were restored in 90% within six days (Eidinger et al., 2012). The EPSs component such as 220kV CVT, 66kV transformer bushings, 11kV switchgear, porcelain surge arresters and non-structural elements in the substation buildings showed mainly slight and partly moderate damages after the 4 September 2010, MW 7.1 Darfield (Canterbury) earthquake, the 22 February 2011, Mw 6.3 Christchurch earthquake and the 13 June 2011, MW 6.0 Christchurch earthquakes in the city Christchurch in New Zealand. The restoration of the transmission systems was completed within less than 6 hours after each earthquake events (Eidinger et al., 2010; Giovinazzi et al., 2011; Transpower, 2011a; Transpower, 2011b). Park et al. (2006) studied the performance of urban electric utility distribution system after the February 28, 2001, MW 6.8 Nisqually earthquake. They estimated the distribution of outage durations and proposed fragility curves for lifelines.

Significant damages to the bus support connectors (Fig. 1-a), surge arrestors (Fig. 1-b), transformer bushings (Fig. 1-c) and disconnect switch corona rings (Fig. 1-d) of 500kV yard of San Diego Gas & Electric's (SDG&E) Imperial Valley Substation were observed after the 4 April 2010, MW 7.2 Mexico earthquake. In the Howard et al. (2015) study, the critical elements for the SDG&E substation were identified and alternative retrofitting approaches were investigated through the nonlinear analysis.

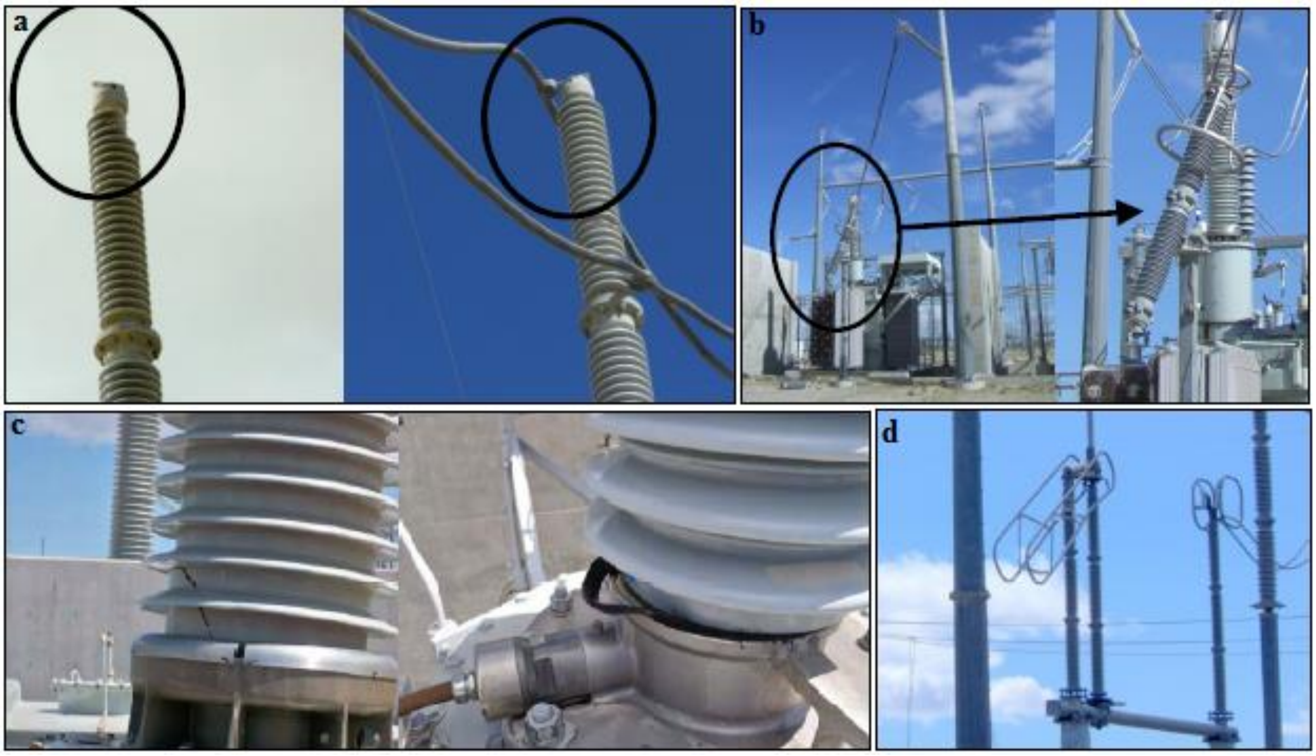

Fig. 1. Common failure types in the typical EPS components.

Buritica´ Corte´s et al. (2015) studied seismic vulnerability of bulk electric power systems by considering form and strength parameters with the hierarchical decomposition method. Different scenarios were considered and obtained results were compared with the traditional methods. Shinozuka et al. (2005) proposed a method for performance evaluation of EPSs of the Los Angeles Department of Water and Power's (LADWP's). 47 earthquake scenarios were used to develop the risk curves and relations with economical parameters were established. In the study of Liu and Feng (2006), seismic safety assessment method of electric power system was evaluated and alternative system flow load control method was proposed. Similarly, seismic vulnerability assessment studies for EPSs and its network with different approaches and methodologies exist in the literature (Bompard et al., 2011; Kwasinski et al., 2014; Li et al., 2008; Ma et al., 2010; Holmgren and Molin, 2006).

In this study, rapid seismic vulnerability assessment has been realized for a typical EPS in Turkey and accordingly probabilities of possible restoration durations have been evaluated. Marmara region which has a high seismic hazard and locates many EPS facilities have been considered. The probability of seismic vulnerability of EPSs, mainly substations and distribution circuits have been assessed based on the fragility curves due to two levels of seismic hazard and two different site conditions of stiff (ZB) and soft (ZD) site classes according to the Turkish Building Seismic Design Code 2018 (TBSDC-2018). The probability of power outage duration has been calculated for different periods using the damage probability matrices and restoration curves.

This study will provide a reliable foresight for possible power outage duration in the typical EPSs in Marmara region and it will also give insight to energy producers to develop their post-earthquake activity plans.

2. Typical Electric Power System and Seismicity of Marmara Region

In general, EPSs consist of substations, distribution circuits and generation facilities. All of these components are exposed to structural damages during major earthquakes. These potential damages may cause significant disruption of power supply. Comparing to conventional building structures, the EPSs comprise rather complex contents due to their sub-elements such as; busbar system, bypass bus, busbar disconnector, circuit breaker, feeder disconnector, bypass disconnector, current transformer, voltage transformer, earthing switch, surge arrester and post insulator, etc. Especially in the high seismic zones, a damage to any sub-element of the EPSs will lead to break entire network's functionality (Nuti and Vanzi, 2004; Wang et al., 2019).

In this study, the substations and distribution circuits as the components of EPSs are considered in the analysis for the power outage estimation methodology. A substation is located in a region where it supplies energy. The key tasks of a substation are changing/switching/regulating voltage level, housing disconnect switches, circuit breakers etc, providing protection from lightening and switching surges, in case of necessity frequency change and AC/DC conversion. A distribution system can be considered as the number of circuits including poles, wires, in-line equipment and utility-specific devices.

In this study, five typical EPSs with different design forms located in Marmara region have been considered for the power outage estimation due to different earthquake hazard levels. The main assessment steps considered are shown in the flowchart in Fig. 2.

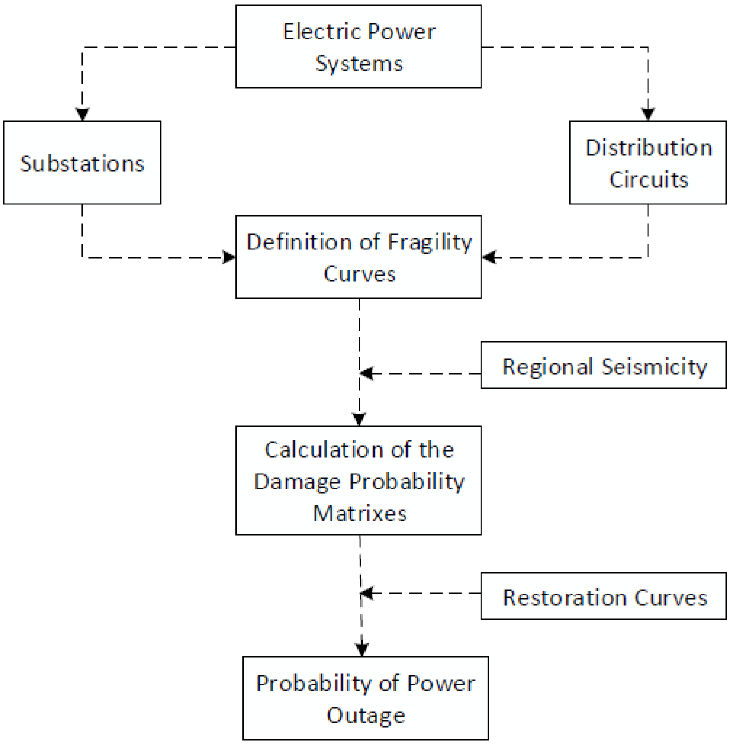

Fig. 2. Assessment methodology for EPSs performance evaluation and power outage estimation.

The seismic vulnerability of substations and distribution circuits are well correlated with the Peak Ground Acceleration (PGA) parameter (HAZUS-MH., 2011).

In the current study, Probabilistic Seismic Hazard Assessments (PSHAs) have been performed in order to evaluate seismic hazard in Marmara region by considering seismic characteristics of the region, and ground motion attenuation models. The PGA distribution has been calculated as the ground motion intensity measure. The EC-FP7 SHARE project delivered a comprehensive seismic hazard model referred as 2013 European Seismic Hazard Model (ESHM2013) for the region (Woessner et al., 2015). In the hazard analyses, reference shear wave velocities, $V_{s,30}$=760m/s and $V_{s,30}$=300m/s, have been used for stiff and soft sites, respectively as shown in Figs. 3 and 4. The PGA distribution maps corresponding to 475 years (DD2) and 72 years (DD3) return period of earthquakes have been derived from hazard analyses results. These results have been used in seismic risk assessment of EPSs.

Probabilistic seismic hazard analyses of EPSs located on the Marmara region have been performed by considering Poisson model (time independent model) under assumption that earthquakes occur with constant average frequency, but independently of each other (Woessner et al., 2015; Cornell, 1968; Scherbaum et al., 2009). Computational model has been implemented in OpenQuake engine for seismic hazard calculations (Pagani et al., 2014). PSHA model includes two important parts; definition of seismic source model that gives information about seismicity of the region and; ground motion model that conducts with attenuation of ground motions by ground motion prediction equations (GMPEs) (Woessner et al., 2015). In this study, source model has been constructed with area sources, background sources and line sources for the region. Area sources were included in the analyses with 0.60 weight, line sources and background sources were included in analyses with 0.40 weight. As the ground motion attenuation models, Abrahamsan and Silva (2008), Boore and Atkinson (2008), Chiou and Youngs (2008), Campbell and Bozorgnia (2008) ground motion prediction equations (GMPEs) were included with 0.25 weight in the probabilistic hazard analyses. Probabilistic seismic hazard curves for EPSs located on Kirklareli, Kocaeli, Balikesir, Bandirma and Canakkale were calculated by seismic hazard analysis based on local site conditions shown at Fig. 5 (Site Class ZD and Site Class ZB).

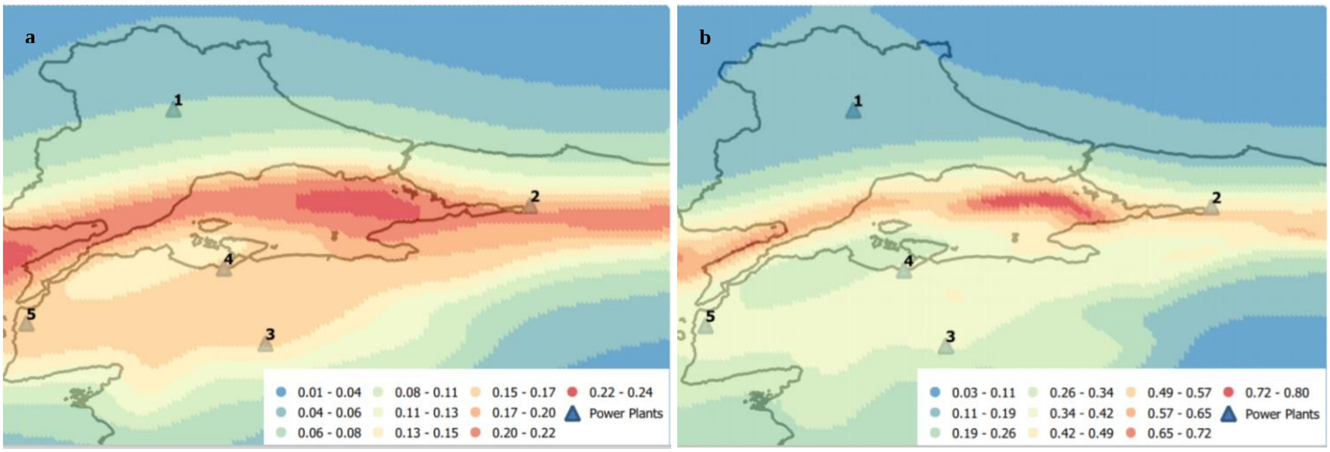

Fig. 3. PGA distribution map for $V_{s,30}$=760m/s:
a) 50 % probability of exceedance in 50 years; b) 10 % probability of exceedance in 50 years.

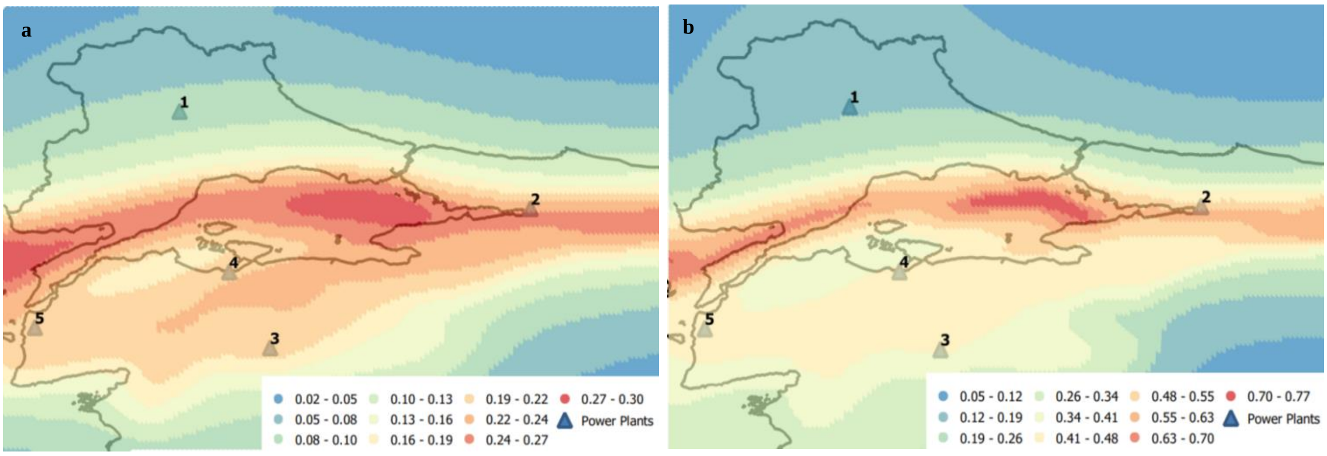

Fig. 4. PGA distribution map for $V_{s,30}$=300m/s:
a) 50 % probability of exceedance in 50 years; b) 10 % probability of exceedance in 50 years

3. Seismic Damage Assessment Based on Fragility Curves

EPSs are one of the vital facilities supplying functionality to other critical infrastructures, lifelines and community. They have also economic and social impact in regional level. The performance assessment of these types of facilities can be achieved by the fragility functions. These curves express the probability of reaching or exceeding structural damage value 'D' for the d_i damage state at that given intensity parameter measure 'Y'. The fragility curve can be considered as a formula of two parameters (median and standard deviation) lognormal distribution functions, is modelled as:

$$P(D \geq d_i|Y) = \phi\left(\frac{lnY - lnY_{mi}}{\xi}\right) \qquad (1)$$

where, Y_{mi} is median threshold value of i^{th} damage state, ξ is the lognormal standard deviation and ϕ represents the standard normal cumulative distribution probability function.

In this study, the fragility functions developed for typical substations and distribution circuits have been adapted for seismic assessment of existing EPSs in Marmara region, Turkey by considering two different design states as proposed in HAZUS-MH (2011). Subsequently, the power outage duration has been estimated by restoration curves depending on the regional seismicity and exposed damage distribution (G&E Engineering Systems, 1994). The adapted fragility curves for the substations(S) and distribution circuits (DC) located in the EPSs for the anchored design (AD) and unanchored design (UD) states are given in Fig. 6.

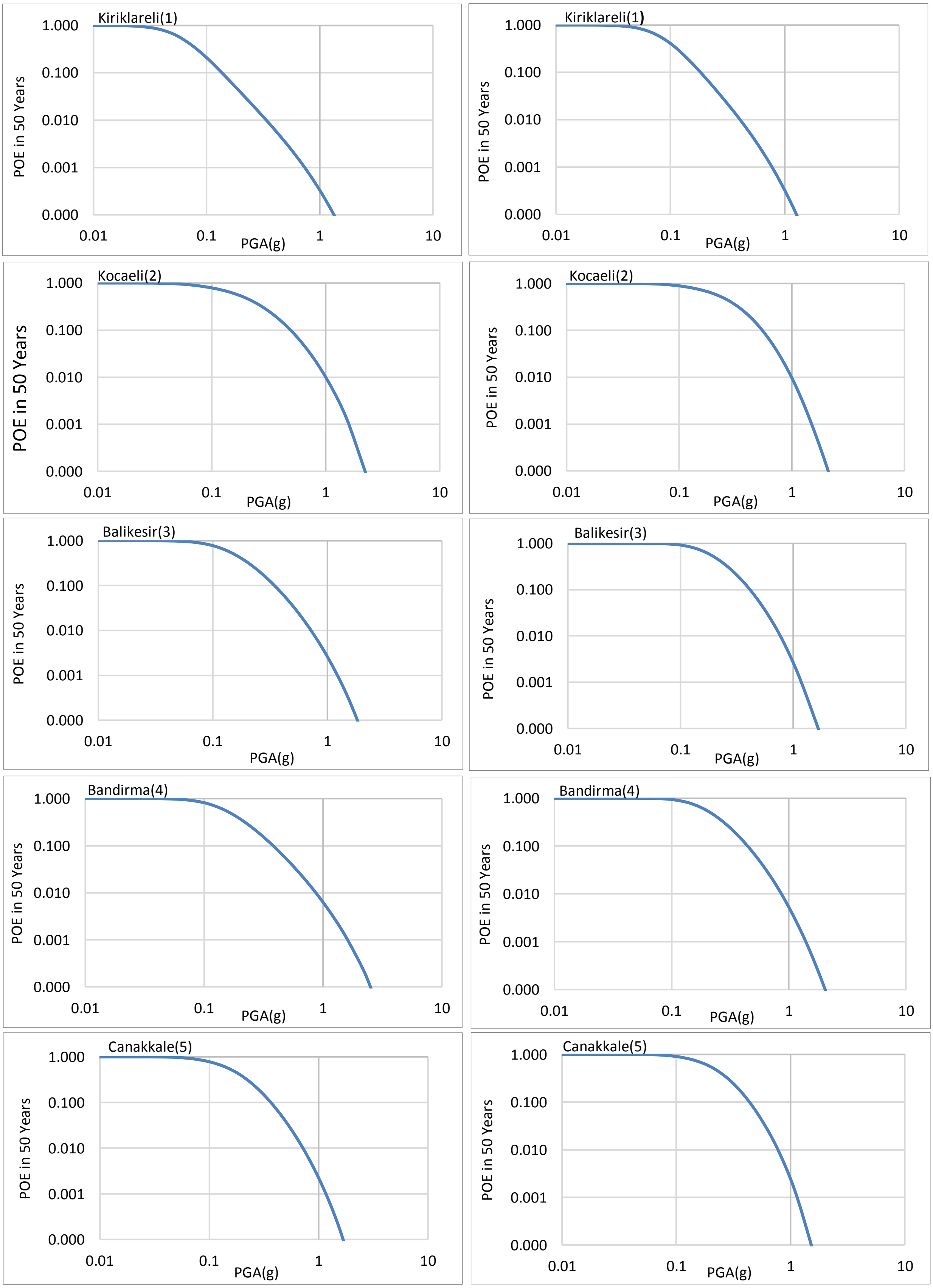

Fig. 5. Considering each location, hazard curves in 50 years of PGA for ZB site class (left side) and ZD site class (right side).

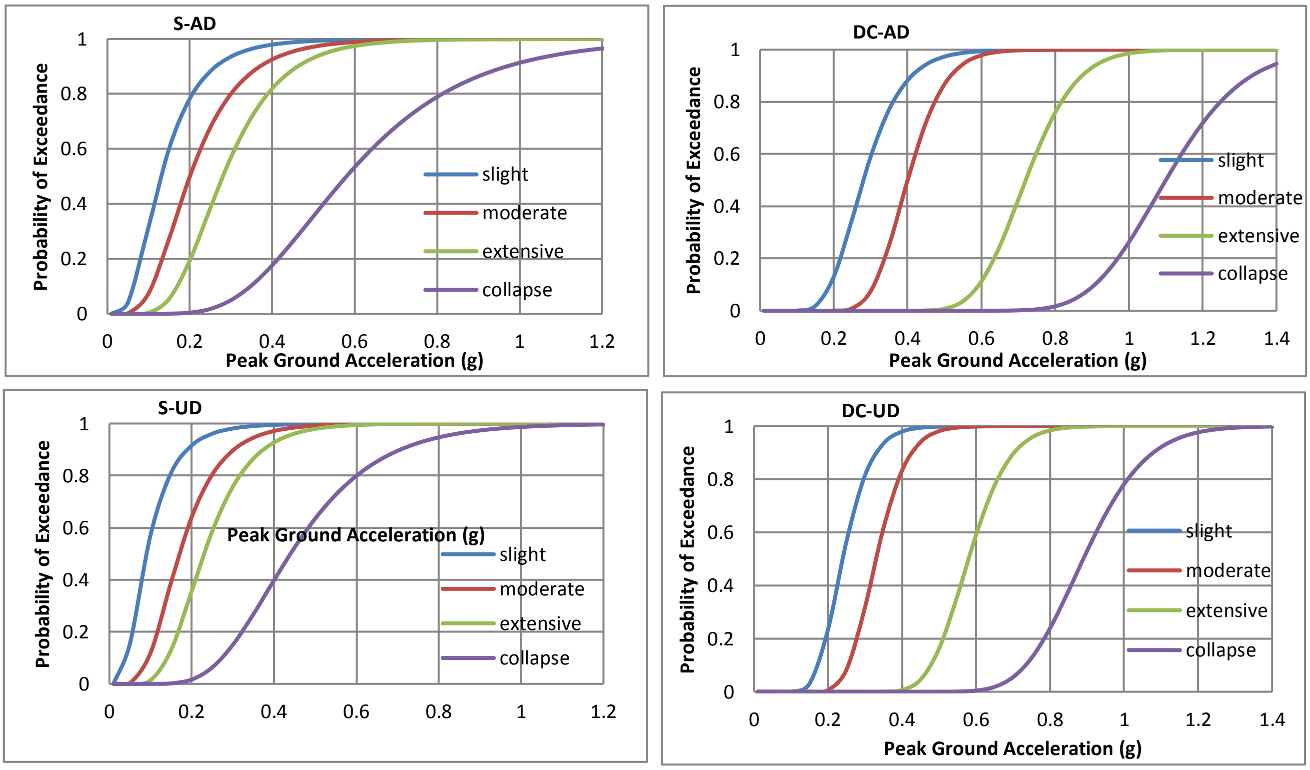

Fig. 6. The adapted fragility curves of the substations (S) and distribution circuits (DC) for the rapid risk assessment.

A total of five damage states as "none, slight, moderate, extensive, and collapse" have been identified in the Fig. 6. In the development of fragility curves, all sub-elements' vulnerability have been considered and mean damage have been extracted for the substations and distribution circuits in each damage state (HAZUS-MH., 2011). Therefore, it is acknowledged that these curves are suitable for the rapid seismic risk assessment of EPSs. In this study, the calculation of power outage in the target facilities have been achieved by considering the restoration curves as shown in Fig. 7 proposed by the G&E report (1994).

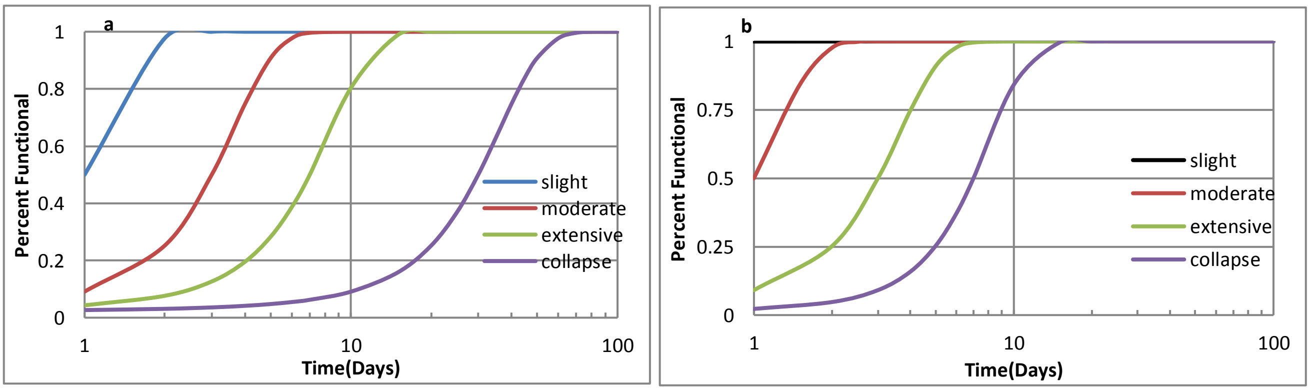

Fig. 7. Restoration curves for electric power systems: a) substations; b) distribution circuits.

The power outages duration at the target sites are defined as the interval of non-functionality of substations and distribution circuits. As it has been mentioned earlier, the substations and distribution circuits are sensitive to earthquake ground motion and in the case of a potential damage it will affect the wide region where these facilities are located.

4. Power Outage Estimation of Electric Power Systems

As described earlier, rapid risk assessment has been applied depending on the seismic hazard for the region and implementing main steps for the assessment as shown in the flowchart in Fig. 2. Using earthquake demand and fragility curves, probability of damage at different damage states (P_{ds_i}) has been calculated. Afterwards, the probability of power outage (PPO) has been calculated based on the Eq. (2) through different days period (T_k) dependent restoration curves (RC).

$$PPO_{T_k} = \sum_{i=1}^{i=5} RC_{d_i,k} \cdot P_{ds_i} \tag{2}$$

The PPO_{T_k} has been calculated and illustrated in Figs. 8 and 9 for ‘S’ and ‘DC’, respectively for DD2 earthquake level (probability of exceedance 10% in 50 years corresponding to 475 years return period earthquake) which is the standard design earthquake level. PSHA has been carried out for ZB ($V_{S,30}$=760m/s) and ZD ($V_{S,30}$=300m/s) site classes representing the stiff and soft site conditions, respectively.

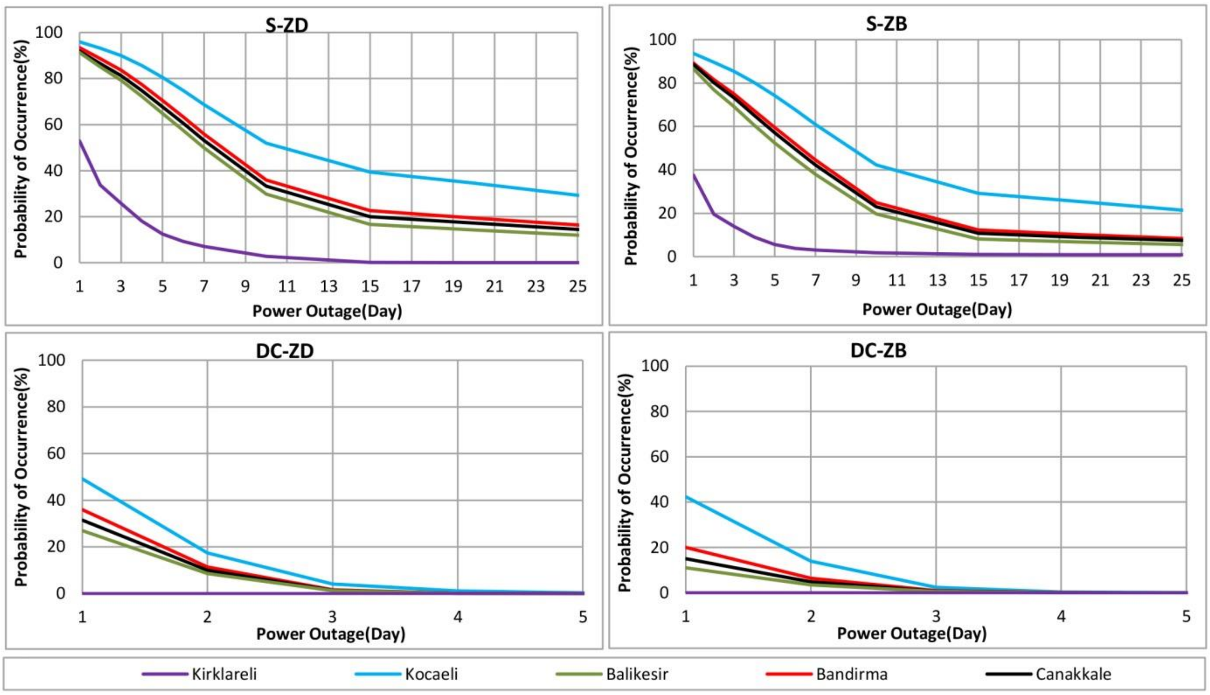

Fig. 8. Power outage estimation for DD2 earthquake level for anchored design substations and distribution circuits.

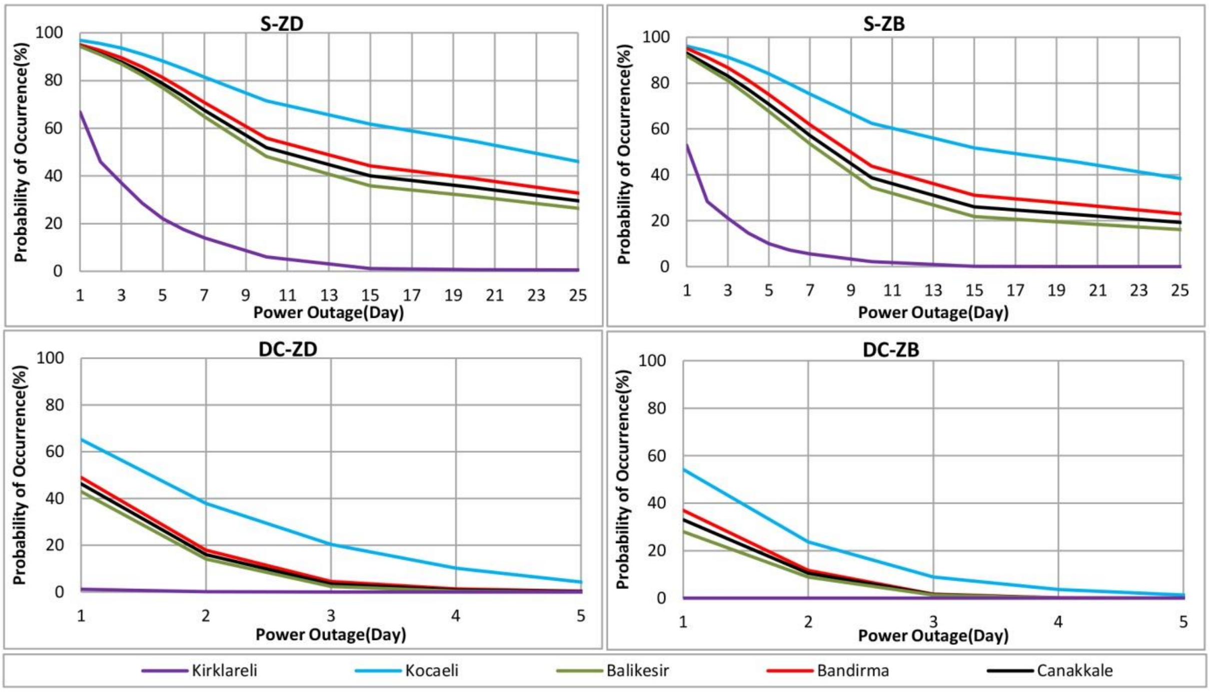

Fig. 9. Power outage estimation for DD2 considering unanchored design substations and distribution circuits.

As it can be seen from Fig. 8 clearly, ‘S’ has higher probability comparing with the ‘DC’ in different period duration of power outage. In this regard, the substations can be considered as critical elements in the current assessment. In the evaluation of five typical EPSs located in Marmara region, the estimated power outages vary dramatically especially in Kocaeli (2) and Kirklareli (1) sites. For example, for 7 days of *PPO* at ‘S’ on ZB site class in Kocaeli (2) is 61% whereas it is 3% in Kirklareli (1).

In Fig. 9, the evaluation of 'UD' case for 'S' and 'DC' at two site classes are given. In ZD site class, the probability of two-days of Power Outage occurrence is obtained as above 90% for the 'S' in all sites except Kirklareli site in which the Power Outage occurrence is found as 45%. For the 'DC', whereas the highest value was 38% in Kocaeli site. There was no Power Outage expected in Kirklareli site. At the other sites, the expected power outage values become between 14% - 20%. The evaluation for DD3 earthquake level (probability of exceedance 50% in 50 years corresponding to 72 years return period earthquake) which is the frequent earthquake as described in TBSDC-2018 has been illustrated in Figs. 10 and 11.

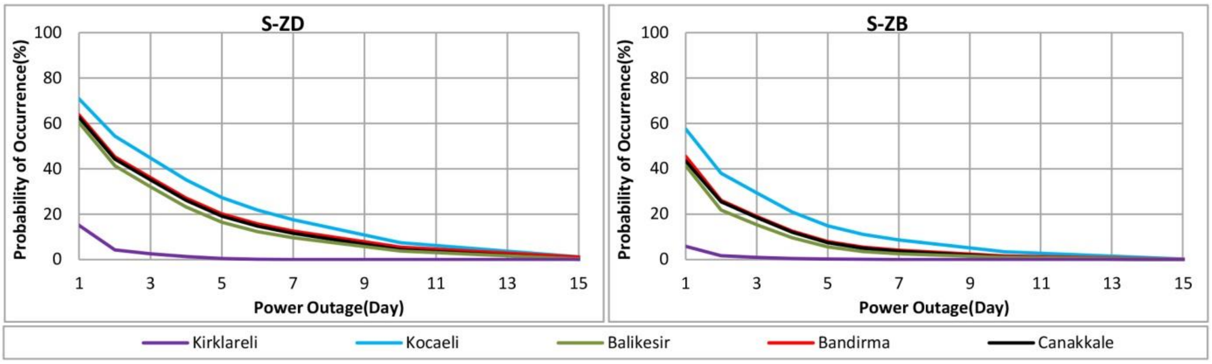

Fig. 10. Power outage estimation for DD3 level considering anchored design substations.

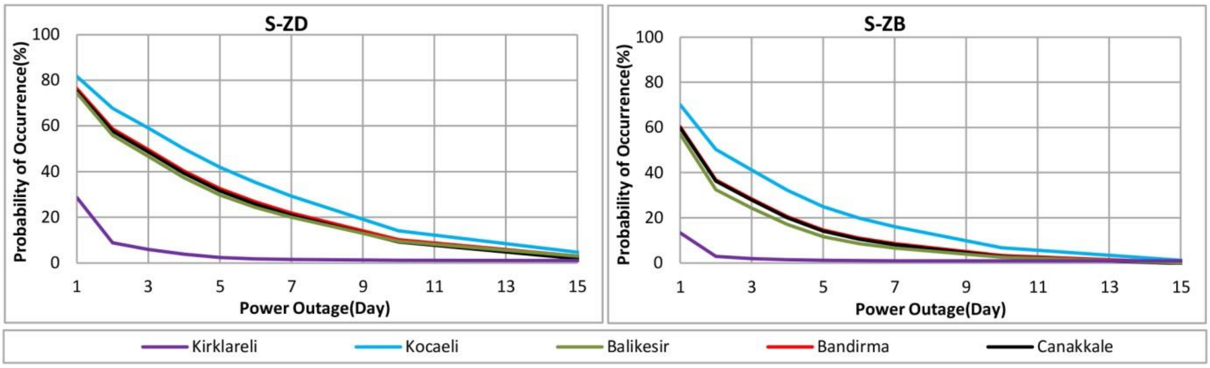

Fig. 11. Power outage estimation for DD3 considering substations with unanchored.

For the typical EPSs in 5 different locations, in the frequent earthquake level in two different site conditions of ZB and ZD, the performance of 'S' is shown in Fig. 10. In the first day, except the Kirklareli site, the *PPO* varies between 60% and 71% in ZD site conditions. In the ZB site condition, this value ranges between 41%-58%. However, in the fifth day after the earthquake the *PPO* varies between 16% and 27% for the ZD site class. It varies between 6% and 14% for ZB site Class. For the Kirklareli site, the first day the *PPO* value becomes 15% for the ZD site and 6% for the ZB site. In the fifth day after the earthquake case it is seen that the facility will be operational in 100% for ZB and ZD site conditions.

In Fig 11, results for the 'S' are taken into account and it is seen that *PPO* values at the end of the 10th day becomes lower than 15% for both site conditions. In the DD3 earthquake level, in the case of 'DC' ('AD' and 'UD' states) with different site conditions *PPO* value is obtained less than 1% and only slight damage is expected for all sites. It is estimated that the possible repairing duration is less than 1 day. It is observed that the acquired results for the two earthquake design levels are compatible with the past earthquake damage data (Eidinger et al., 2012; Giovinazzi et al., 2011).

5. Conclusions

EPSs have critical importance in the sustainability of social life and economy. The past and recent earthquakes showed clearly that these systems have high vulnerability due to earthquakes. In this study, the typical EPSs which are commonly preferred and located at 5 different sites in Marmara region in Turkey have been examined. The vulnerabilities for the two design states of (anchored-unanchored) cases have been assessed. In the first part of the study, the earthquake hazard for Marmara region has been accomplished. The earthquake hazard curves at 5 different sites for two different earthquake levels of DD2 and DD3, and two different site conditions of ZD and ZB site classes according to the TBSDC-2018 have been obtained. In the calculation of *PPO* due to a potential future earthquake, the assessments have been carried out through the substations (S) and distribution circuits (DC). The *PPO* values have been calculated for different durations using the fragility curves and restoration curves.

The obtained results showed that there is significant variation in the *PPO* values in different sites in Marmara region. Considering the *PPO* values obtained depending on the vulnerability, it is seen that 'S' is in a much more critical situation when compared with 'DC'. In general, considering the seismicity of the target region for the earthquake level DD2, the probability of interruption for the 7-days restoration period in the anchored (AD) design of the substations in all locations except Kirklareli on the ZD site condition is 50%-69%, whereas in unanchored (UD) case it becomes 65% -82%. At DD3 level, this value was obtained around 9% -17% for 'AD' and 20% -29% for 'UD'. In Kirklareli location for the DD2 earthquake level and ZD site condition, the *PPO* value of 'S' is 7% for 'AD' and 14% for 'UD'. At the same location, at DD3 level, there is no power outage probability for 'AD', but 1.5% for 'UD'.

It has been observed that the results obtained within the scope of the study are highly consistent with post-earthquake studies in the literature. Therefore, for any EPSs to be considered in the Marmara region, the results of this study through the power outage graphics enable a quick preliminary evaluation of the power outage for the current design status and location in a very practical way. This allows the development of action plans for the EPS facilities before the potential future earthquake.

REFERENCES

Abrahamson N, Silva W (2008). Summary of the Abrahamson & Silva NGA ground-motion relations. *Earthquake Spectra*, 24(1), 67-97.

Bompard E, Wu D, Xue F (2011). Structural vulnerability of power systems: A topological approach. *Electric Power Systems Research*, 81(7), 1334-1340.

Boore DM, Atkinson GM (2008). Ground-motion prediction equations for the average horizontal component of PGA, PGV, and 5%-damped PSA at spectral periods between 0.01 s and 10.0 s. *Earthquake Spectra*, 24(1), 99-138.

Buriticá Cortés JA, Sánchez-Silva M, Tesfamariam S (2015). A hierarchy-based approach to seismic vulnerability assessment of bulk power systems. *Structure and Infrastructure Engineering*, 11(10), 1352-1368.

Campbell KW, Bozorgnia Y (2008). NGA ground motion model for the geometric mean horizontal component of PGA, PGV, PGD and 5% damped linear elastic response spectra for periods ranging from 0.01 to 10 s. *Earthquake Spectra*, 24(1), 139-171.

Chiou BJ, Youngs RR (2008). An NGA model for the average horizontal component of peak ground motion and response spectra. *Earthquake Spectra*, 24(1), 173-215.

Cornell CA (1968). Engineering seismic risk analysis. *Bulletin of the Seismological Society of America,* 58, 1583-1606.

Eidinger J, Tang A, O'Rourke T (2010). Technical Council on Lifeline Earthquake Engineering (TCLEE), Report of the 4 September 2010 Mw 7.1 Canterbury (Darfield), New Zealand Earthquake. *American Society of Civil Engineers,* 1-49.

Eidinger J, Davis C, Tang A, Kempner L (2012). M 9.0 Tohoku earthquake March 11 2011 performance of water and power systems. G & E Engineering Systems Inc, Oakland, CA.

Fujisaki E, Takhirov S, Xie Q, Mosalam KM (2014). Seismic vulnerability of power supply: lessons learned from recent earthquakes and future horizons of research. *In Proceedings of 9th International Conference on Structural Dynamics (EURODYN 2014)*. European Association for Structural Dynamics, Porto, Portugal, 345-350.

G&E Engineering Systems, Inc. (1994). NIBS Earthquake Loss Estimation Methods. Technical Manual, (Electric Power Systems), June.

Giovinazzi S, Wilson TM, Davis C, Bristow D, Gallagher M, Schofield A, Tang A (2011). Lifelines performance and management following the 22 February 2011 Christchurch Earthquake, New Zealand: Highlights of Resilience.

HAZUS-MH (2011). Multi-Hazard Loss Estimation Methodology: Earthquake Model Hazus-MH MR5 Technical Manual.

Holmgren ÅJ, Molin S (2006). Using disturbance data to assess vulnerability of electric power delivery systems. *Journal of Infrastructure Systems*, 12(4), 243-251.

Howard S, Riker C, Knight B, Knoles S (2015). Innovative Analysis and Seismic Retrofit of 500kV Flexible Bus Substation Support Structures. *Electrical Transmission and Substation Structures,* 438-451.

Kwasinski A, Eidinger J, Tang A, Tudo-Bornarel C (2014). Performance of electric power systems in the 2010-2011 Christchurch, New Zealand, earthquake sequence. *Earthquake Spectra*, 30(1), 205-230.

Li W, Zhou J, Xie K, Xiong X (2008). Power system risk assessment using a hybrid method of fuzzy set and Monte Carlo simulation. *IEEE Transactions on Power Systems*, 23(2), 336-343.

Liu C, Feng F (2006). Seismic security analysis and flow load control of power supply system. *2006 IEEE International Conference on Information Acquisition*, 1239-1243.

Ma J, Huang Z, Wong PC, Ferryman T, Northwest P (2010). Probabilistic vulnerability assessment based on power flow and voltage distribution. *Transmission and Distribution Conference and Exposition*, 2010 IEEE PES 1- 8, Chicago, IL, May 7-10.

Massie A, Watson NR (2011). Impact of the Christchurch earthquakes on the electrical power system infrastructure. *Bulletin of the New Zealand Society for Earthquake Engineering*, 44(4), 425-430.

Nuti C, Vanzi I (2004). Earthquake structural retrofitting of electric power networks under economic constraints. *2004 International Conference on Probabilistic Methods Applied to Power Systems*, 987-992.

Pagani M, Monelli D, Weatherill G, Danciu L, Crowley H, Silva V, Simionato M (2014). OpenQuake engine: An open hazard (and risk) software for the global earthquake model. *Seismological Research Letters*, 85(3), 692-702.

Park J, Nojima N, Reed DA (2006). Nisqually earthquake electric utility analysis. *Earthquake Spectra*, 22(2), 491-509.

Scherbaum F, Delavaud E, Riggelsen C (2009). Model selection in seismic hazard analysis: an information theoretic perspective. *Bulletin of the Seismological Society of America*, 99, 3234-3247.

Shinozuka M, Cheng TC, Feng M, Mau ST (1999). Seismic performance analysis of electric power systems. *Research Progress and Accomplishments*, 1997-1999, 61-69.

Shinozuka M, Dong X, Jin X, Cheng TC (2005). Seismic performance analysis for the ladwp power system. *2005 IEEEPES Transmission & Distribution Conference & Exposition Asia and Pacific,* 1-6.

TBSDC (2018). Turkish Building Seismic Design Code. Disaster and Emergency Management Authority, Ankara, Turkey.

Transpower (2011a). 4 September 2010 Darfield earthquake. Lessons learned. Transpower New Zealand Limited Internal Report, 30 March.

Transpower (2011b). 22 February 2011 Christchurch earthquake Key findings and lessons learned. Transpower New Zealand Limited Internal Report, 30 June.

Wang C, Feng K, Zhang H, Li Q (2019). Seismic performance assessment of electric power systems subjected to spatially correlated earthquake excitations. *Structure and Infrastructure Engineering*, 15(3), 351-361.

Watson NR (2010). Impact of the Darfield earthquake on the electrical power system infrastructure. *Bulletin of the New Zealand Society for Earthquake Engineering*, 43(4), 421-424.

Woessner J, Laurentiu D, Giardini D, Crowley H, Cotton F, Grünthal G, Hiemer S (2015). The 2013 European seismic hazard model: key components and results. *Bulletin of Earthquake Engineering*, 13(12), 3553-3596.

CHALLENGE JOURNAL OF STRUCTURAL MECHANICS 7 (2) (2021) 93–106

Research Article

A comparative study on yield line mechanisms for four bolted extended end-plated connection

Yasin Onuralp Özkılıç [a,*]

[a] *Department of Civil Engineering, Necmettin Erbakan University, 42090 Konya, Turkey*

ABSTRACT

Extended end-plated connections are preferred in moment resisting frames due to their advantages such as no required in-situ welding, accurate fabrication and economic feasibility compared to flange welded moment connections. The capacity of the extended end-plated connections depends on bolt configurations, end-plate thickness, bolt diameter and their material properties excluding column part. The thickness of end-plate can be computed using yield line mechanisms. Different yield line patterns are available in the literature and some of these are adopted in seismic codes to estimate the thickness of end-plate. In this study, the accuracy of different yield line patterns is compared using collected experimental data and numerical analysis. A parametric numerical analysis was conducted utilizing the finite element tool, ABAQUS. The results of experimental data and parametric study were evaluated for both unstiffened and stiffened four bolted extended end-plated connections. The results revealed that the capacity of the end-plate connections significantly depends on the yield line mechanism. Therefore, selecting an accurate yield line mechanism is essential in order not to overestimate the thickness of the end-plate. More importantly is that these yield line mechanisms can be directly implemented to AISC 358 and Turkish Building Earthquake Code 2018 (TBEC-2018).

ARTICLE INFO

Article history:
Received 31 October 2020
Revised 31 January 2021
Accepted 2 March 2021

Keywords:
Extended end-plate connection
Stiffened
Unstiffened
Yield line mechanism
Numerical analysis

1. Introduction

End-plated connections are composed of a plate welded to a beam and attached to a beam or a column with pretensioned bolts. End-plated connections are classified into two categories: flush end-plate or extended end-plate. In extended end-plated connections, end-plates extend beyond the beam flanges so that at least one bolt row can be attached beyond the beam flanges. In flush end-plated connection, an extension of the plate is limited. Extended end-plated and flush end-plated connections are given in Fig. 1.

Extended end-plated connections are used in beam to column connections in moment-resisting frames. One of the most common extended end-plated configurations is shown in Fig. 2(a). In some cases, an additional plate is welded between end-plate and beam flanges. This plate is called stiffener or rib. This stiffener is used to reduce end-plate thickness. In other words, this stiffener is used to increase the moment capacity of the connection. Stiffened extended end-plated configurations are shown in Fig. 2(b).

End-plated connections are preferred due to eliminating welding process in field, easy and fast erection, cheap installation, and suitable for winter erection. Research related to end-plated connections has been studying since 1950 and the studies are still ongoing (Karasu and Vatansever, 2021; Akgönen and Güneş, 2017; Sağıroğlu, 2018; Yılmaz and Bekiroğlu, 2016; Özkılıç, 2021). The earlier connection designs result in thick end plates and large bolts since these designs were based on only statics. Later, design methods were developed thanks to finite element analyses. Other studies related to yield line theory improved the design methods.

Kennedy et al. (1981) developed design guidelines for tee sub connections including three stages of plate behavior: thick plate, intermediate plate and thin plate.

---

* *Corresponding author.* Tel.: +90-332-325-2024 ; E-mail address: yozkilic@erbakan.edu.tr (Y. O. Özkılıç)

ISSN: 2149-8024 / DOI: https://doi.org/10.20528/cjsmec.2021.02.005

In thick plates, no prying forces are available. When the load increase, plastic hinge occur in the plate and the prying forces are formed. The plate is called an intermediate plate when prying forces are present. If the prying forces reach maximum, the plate is called a thin plate.

Nomenclature

b_{fp}	Width of beam flange
b_p	Width of end-plate
C	Cyclic
d	Depth of beam excluding flange thickness
d_b	Bolt diameter
d_e	Vertical edge distance for outside holes
d_h	Sum of bolt hole diameters across width of end-plate
F_y	Yield strength of end-plate
F_u	Ultimate strength of end-plate
g	Horizontal distance between the bolts
h_o	Distance from the centerline of the compression flange to the tension side outer bolt row
h_i	Distance from the centerline of the compression flange to the tension side inner bolt row
L	Loading type
M	Monotonic
M_A	Moment capacity predicted by Adey et al. (1997)
M_S	Moment capacity predicted by Srouji et al. (1983)
$M_{\ddot{O}}$	Moment capacity predicted by Özkılıç (2020a)
M_u	Required flexural strength
p	The length of yield line which extends to web (0.35d)
p_{fi}	Vertical distance from inside of a beam tension flange to nearest inside bolt row
p_{fo}	Vertical distance from inside of a beam tension flange to nearest outside bolt row
Stif.	Stiffening
S	Stiffened
t_f	Flange thickness
t_p	End-plate thickness
t_s	Stiffener thickness
t_w	Weld thickness
U	Unstiffened
w_f	Flange weld thickness
w_s	Stiffener weld thickness
w_w	Web weld thickness

Murray (1988) reviewed previous studies for flush end-plated and extended end plated configurations and design guidelines were presented. Murray (1990) developed design procedures for unstiffened four bolt case and stiffened extended eight bolt case. Chasten (1992) conducted seven experiments with extended end plate connections. The effects of prying forces were investigated. A simple design guideline was presented in addition to the existing design procedure. Hendrick and others (1995) modified the Kennedy methods to predict bolt forces. The modified Kennedy methods were compared with experimental results. The results indicated that the modified Kennedy methods predict bolt forces accurately.

Borgsmiller (1995) developed new and simple design methods for flush end-plate and extended end plate connections. The bolt design methods were improved using Kennedy methods. The thickness of end-plates was determined using yield line theory. In previous test results, it was observed that prying forces should be taken into account when ninety percent of end-plate strength is achieved. If applied loads exceed 90% of plate strength, the end plate is considered as thin plate and if applied loads are less than 90% of plate strength, the end-plate is considered as thick plate. In thick plates, prying forces are neglected and in thin plates, prying forces are taken as maximum. This simplified method is used in the current AISC provision with slight changes.

Summer and Murray (2001) developed new design methods including thin and thick plate designs. Six test specimens designed according to these methods were tested under monotonic loading. The results indicated that proposed design methods conservatively predict the strength of connections. Summer and Murray (2002) tested seven extended end plate specimens under cycling loading. It was concluded that extended end plate connections can be used in seismic region and the connections should be stronger than the beam so that failure will occur in the beam section. Murray and Shoemaker (2002) published a new design procedure for flush end-plated and extended end-plated connections based on Borgimiller's (1995) study. However, these procedures were valid only for low seismic forces and wind. Thickness of end plates were determined from yield line analysis and bolt forces were determined from the simplified Kennedy method. Summer (2003) conducted experimental and analytical studies to develop design guidelines for eight bolted extended end-plated connections exposed to cyclic loading. Eleven specimens were tested under cyclic loading and nine specimens were tested under monotonic loading. The proposed design methods were compared with the previously tested ninety experiments. The proposed guideline was a good correlation with previous experimental results.

2. Yield Line Mechanisms

Yield line method was firstly developed in order to calculate the strength of concrete slabs. This method basically relies on the virtual work method. It is important to accurately determine failure patterns, in other words, yield lines. Inaccurate yield lines may result in conservative or unconservative results depends on the length of the yield line. This method is utilized for the calculation of end-plate resistance. End-plate fracture and bolt fracture are the main failure modes of the end-plated connection. The prediction of the moment capacity of the end-plate connection is calculated as virtual work produced by end-plate yield lines for yield mechanism.

Surtress and Man (1970) conducted the first study to predict the capacity of end-plate using yield lines. Then, Packer and Morris (1977) used yield line mechanism. Later, Mann and Morris (1979) modified the equation proposed by Packer and Morris. Whittaker and Walpole (1982) modified the yield line proposed by Surtress and

Man (1970) in order to take into account weld thickness. These yield lines are only applicable to unstiffened four bolted end-plated connections. Srouji et al. (1983) proposed yield line mechanisms for both unstiffened and stiffened four bolted end plated connections. This yield line mechanism is currently used by AISC 358. Two different yield lines were developed depends on the length of end-plate extension beyond the outside bolt line. The calculation of end-plate thickness is not related to diameter of bolts, instead, yield line pattern and yield strength of end-plates are only parameters that affect the thickness of end-plate. Different from Srouji et al. (1983), AISC 358 guideline includes a constant value of 1.11 to numerator.

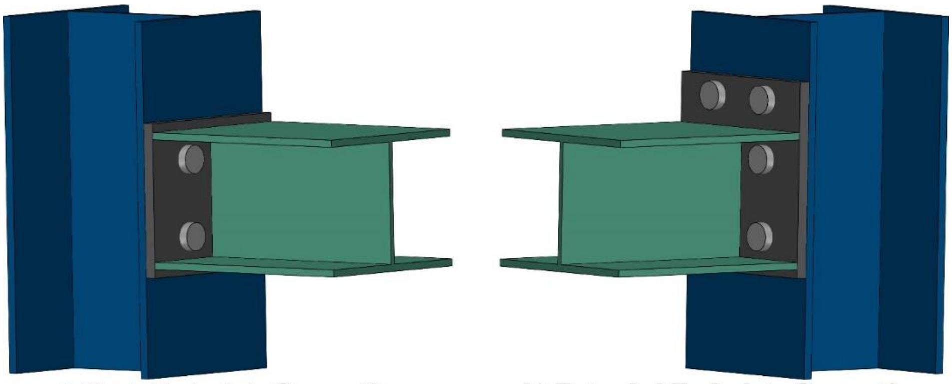
a) Flush End-plate Connection b) Extended End-plate Connection

Fig. 1. End plated connections: (a) flush; (b) extended.

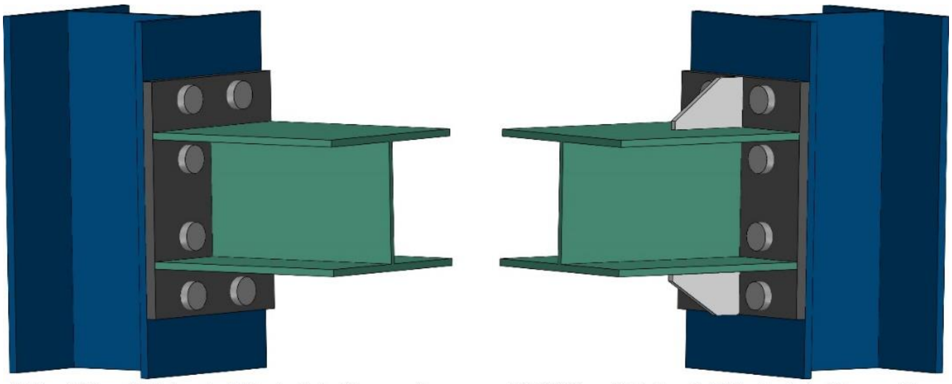
a) Unstiffened Extended End-plate Connection b) Stiffened Extended End-plate Connection

Fig. 1. Extended end plate connections: (a) Unstiffened; (b) Stiffened.

Adey et al. (1997) modified Whittaker and Walpole's yield line equations to obtain more accurate results for both unstiffened and stiffened four bolted end-plated connections. In the yield line mechanism of Whittaker and Walpole, yield line between the inner bolts reached 0.6d. However, Adey et al. (1997) changed the distance of this yield line to 0.35d. Moreover, the yield line mechanism of Whittaker and Walpole only takes into account weld thickness; however, the yield line mechanism of Adey et al. (1997) takes into account both weld thickness and diameter of bolt.

Özkılıç (2020a) and Özkılıç and Topkaya (2021a) proposed yield mechanism which takes into account reductions due to weld length and diameter of bolts for both unstiffened and stiffened four bolted end plated connection. Özkılıç (2020a) modified yield mechanism developed by Srouji et al. (1983) for unstiffened case while Özkılıç (2020a) modified yield mechanism developed by Shi et al. (2007) for stiffened case by taking into account reductions due to weld length and diameter of bolts.

The calculation of end-plate thickness using the aforementioned yield lines for unstiffened and stiffened four bolted cases are depicted in Tables 1 and 2, respectively. Moreover, the yield mechanisms proposed by Srouji et al. (1983), Aday et al. (1997) and Özkılıç (2020a) are illustrated in Fig. 3 for both unstiffened and stiffened four bolted cases.

Currently, Turkish Building Earthquake Code 2018 (TBEC-2018) defines four bolted extended end-plated connections as moment connections. However, the calculation of the capacity of the extended end-plated connections is not currently included in Turkish Building Earthquake Code 2018 (TBEC-2018). AISC 358-16 utilizes the yield mechanism of Srouji (1983) to calculate the end-plate thickness for four bolted extended end-plated connections which results in very conservative estimation.

In this present study, three different yield line mechanisms are evaluated using the collected experimental data and numerical analysis. The accuracy of these yield lines are compared and their conservatisms are presented. These yield lines can be directly adopted in TBEC-2018 and AISC 358-16 with proposed safety and overstrength factors.

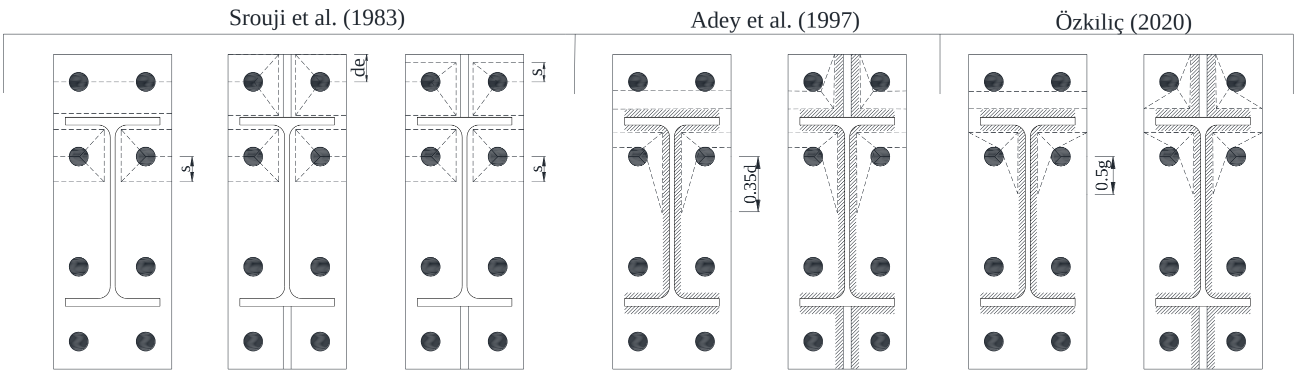

a) Unstiffened b) Stiffened $d_e \leq s$ c) Stiffened $d_e > s$ a) Unstiffened b) Stiffened a) Unstiffened b) Stiffened

Fig. 3. Yield line mechanisms.

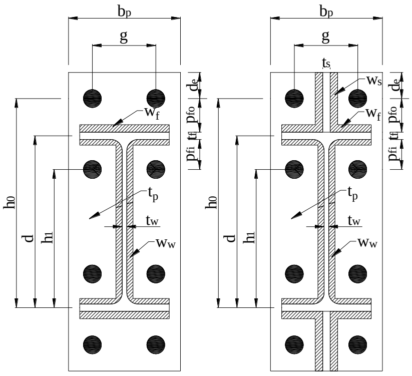

a) Unstiffened b) Stiffened

Fig. 4. Parameters used in the calculation of yield line mechanism.

Table 1. Calculation of end-plate thickness for unstiffened four bolted extended end-plate.

Surtress and Man (1970)	$t_{p,reqd} = \sqrt{\frac{M_u}{F_{py} d (2\frac{b_p}{c} + \frac{d_f}{g})}}$
Packer and Morris (1977)	$t_{p,reqd} = \sqrt{\frac{\alpha M_u}{F_{py} d (b_p - d_h)}}$
Mann and Morris (1979)	$t_{p,reqd} = \sqrt{\frac{\alpha M_u}{F_{py} d b_p}}$
Whittaker and Walpole (1982)	$t_{p,reqd} = \sqrt{\frac{M_u}{F_{py} d \left[2\frac{b_p}{c - t_f - w_f} + \frac{2p}{g - t_w - 2w_w}\right]}}$
Srouji et al. (1983)	$t_{p,reqd} = \sqrt{\frac{M_u}{F_{py} \frac{b_p}{2}\left[h_1\left(\frac{1}{p_{fi}} + \frac{1}{s}\right) + h_0\left(\frac{1}{p_{fo}}\right) - \frac{1}{2}\right] + \frac{2}{g}\left[h_1(p_{fi} + s)\right]}}$
Adey et al. (1997)	$t_{p,reqd} = \sqrt{\frac{M_u}{F_{py} d \left[\frac{b_p}{2(p_{fo} - \frac{d_b}{2} - w_f)} + \frac{2p}{g - t_b - 2w_w - d_b} + \frac{b_p - t_f - 2w_w}{2(p_{fi} - \frac{d_b}{2} - w_f)}\right]}}$
Özkılıç (2020a)	$t_{p,reqd} = \sqrt{\frac{M_u}{F_{py}\left[h_o\left[\frac{b_p}{2}\frac{1}{p_{fo} - 0.5d_b - w_f}\right] + 2h_1\left[\frac{b_p - t_{web} - 2w_w}{4(p_{fi} - 0.5d_b - w_f)} + \frac{p_{fi} - w_f + 0.5g}{g - t_{web} - 2w_w - d_b}\right]\right]}}$

Table 2. Calculation of end-plate thickness for stiffened four bolted extended end-plate.

Srouji et al. (1983)	when $d_e \leq s$ $t_{p,reqd} = \sqrt{\dfrac{M_u}{F_{py}\left[\frac{b_p}{2}\left[h_1\left(\frac{1}{p_{fi}}+\frac{1}{s}\right)+h_0\left(\frac{1}{p_{fo}}+\frac{1}{2s}\right)\right]+\frac{2}{g}\left[h_1(p_{fi}+s)+h_0(p_{fo}+d_e)\right]\right]}}$ when $d_e > s$ $t_{p,reqd} = \sqrt{\dfrac{M_u}{F_{py}\left[\frac{b_p}{2}\left[h_1\left(\frac{1}{p_{fi}}+\frac{1}{s}\right)+h_0\left(\frac{1}{p_{fo}}+\frac{1}{s}\right)\right]+\frac{2}{g}\left[h_1(p_{fi}+s)+h_0(p_{fo}+s)\right]\right]}}$ $s = \frac{1}{2}\sqrt{b_p g}$
Adey et al. (1997)	$t_{p,reqd} = \sqrt{\dfrac{M_u}{F_{py}d\left[\frac{b_p-t_s}{2\left(p_{fo}-\frac{d_b}{2}-w_f\right)}+\frac{2(p_{fo}+d_e)}{g-t_s-2w_s-d_b}+\frac{2p}{g-t_b-2w_w-d_b}+\frac{b_p-t_f-2w_w}{2\left(p_{fi}-\frac{d_b}{2}-w_f\right)}\right]}}$
Özkılıç (2020a)	$t_{p,reqd} = \sqrt{\dfrac{M_u}{F_{py}\begin{bmatrix}2h_o\left[\frac{b_p-t_s-2w_s}{4(p_{fo}-0.5d_b-w_f)}+\frac{p_{fo}-w_f+d_e}{g-t_s-2w_s-d_b}\right]+\\ 2h_1\left[\frac{b_p-t_w-2w_w}{4(p_{fi}-0.5d_b-w_f)}+\frac{p_{fi}-w_f+0.5g}{g-t_{web}-2w_w-d_b}\right]\end{bmatrix}}}$

Currently, Turkish Building Earthquake Code 2018 (TBEC-2018) defines four bolted extended end-plated connections as moment connections. However, the calculation of the capacity of the extended end-plated connections is not currently included in Turkish Building Earthquake Code 2018 (TBEC-2018). AISC 358-16 utilizes the yield mechanism of Srouji (1983) to calculate the end-plate thickness for four bolted extended end-plated connections which results in very conservative estimation. In this present study, three different yield line mechanisms are evaluated using the collected experimental data and numerical analysis. The accuracy of these yield lines are compared and their conservatisms are presented. These yield lines can be directly adopted in TBEC-2018 and AISC 358-16 with proposed safety and overstrength factors.

3. Data Collection

The experimental data is collected for both the unstiffened and stiffened extended end-plated connections (Özkılıç and Topkaya, 2021b). The experimental data is selected based on two important criteria. The first criterion is that the main failure mode of the experiment should be end-plate related failure. Bolt failures, column failures, beam failures and welding failure may lead to making inaccurate interpretations for comparing the capacity of the end-plate. In other words, the specimens that failed due to non-related failures of end-plate are most probably failed before reaching the capacity of the end-plate. The second criterion is that the moment capacity of the beam section should be higher than the ultimate capacity of the experiment. This criterion is set in order to limit or prevent the contribution of the beam on the capacity. Similarly, if the capacity of the beam is much less than the ultimate capacity, the specimen is most probably failed before reaching the capacity of the end-plate.

The collected experimental data for the unstiffened case is shown in Table 3. A total of 34 experiments from 14 studies are selected based on the aforementioned criteria. Within the experimental data, the thickness of end-plate varies between 8 and 23 mm. Both cyclic and monotonic loadings are included. The diameter of bolt ranges between 12.7 mm and 31.8 mm. The depth of beams varies between 225 mm and 580 mm (except #26, 28).

The collected experimental data for the stiffened case is shown in Table 4. A total of 8 experiments from 4 studies are selected based on the aforementioned criteria. Unfortunately, very limited experiments are available accompanying the aforementioned criteria. Within the experimental data, the thickness of end-plate varies between 12-16 mm. Only cyclic loadings are available. The diameter of bolt ranges between 20.0 mm and 31.8 mm. The depth of beams varies between 225 mm and 580 mm.

4. Results and Discussions on the Collected Experimental Data

Two important capacities which are ultimate moment capacity (M_u) and plastic moment capacity (M_{pl}) are reported. The ultimate moment capacity (M_u) is the maximum moment that occurred during the experiments. On the other hand, plastic moment capacity (M_{pl}) is the moment at the intersection of tangent lines passing elastic and plastic zones. Fig. 5 demonstrates the typical moment rotation relationship for end-plated connection. The strength of the end-plated connection can be defined using M_u or M_{pl} and no absolute definition is available in the literature. It is accepted that all yield lines are formed at M_{pl}. Strain hardening and second order effects are included in M_u.

Table 5 shows the results for unstiffened extended end-plated connections. The ratio of M_p/M_u is equal or larger than 1.0 indicating that the extended end-plate connection reached its ultimate capacities without reaching plastic moment capacity of the beam. The ratio of M_u/M_{pl} ranges between 1.05 and 2.11. It means that the extended end-plated connection can perform more than two times plastic moment capacity. It is a direct indication that design guidelines that utilize plastic moment capacities overly underestimate the capacity of the extended end-plate connection.

Table 3. Properties of experimented specimens for unstiffened four bolted case.

#	Specimens	L	t_p	F_y	F_u	d_b	t_f	t_w	b_{fp}	b_p	w_f	w_w	g	p_{fi}	p_{fo}	d_e	h_o	h_i
1	SP6	C	12	325	388	24	9.8	6.2	120	150	10	10	85	40	45	35	280	185
2	SP7	C	10	313	387	24	9.8	6.2	120	150	10	10	85	40	45	35	280	185
3	FS1a	M	10	340	481	20	10.7	7.1	150	150	6	4	90	40	40	30	335	245
4	FS1b	M	10	340	481	20	10.7	7.1	150	150	6	4	90	40	40	30	335	245
5	FS4a	M	10	698	741	20	10.7	7.1	150	150	6	4	90	40	40	30	335	245
6	FS4b	M	10	698	741	20	10.7	7.1	150	150	6	4	90	40	40	30	335	245
7	S2	C	13.3	295	501	25.4	11.6	7.2	171	200	10	10	100	44	44	30	390	290
8	S3	C	13	285	510	25.4	11.6	7.2	171	200	10	10	100	44	82	30	428	290
9	M1	C	15.9	340	510	28.6	19	11	193	230	12	12	125	45	45	60	500	390
10	M2	C	15.9	340	510	28.6	19	11	193	230	12	12	125	45	100	60	555	390
11	M3	C	19	356	504	31.8	19.0	11.4	193	230	12	12	125	45	100	60	555	390
12	L1	C	15.9	340	510	25.4	19.6	12	229	270	12	12	150	44	45	60	645	536
13	L2	C	15.9	340	510	25.4	19.6	12	229	270	12	12	150	45	135	60	735	535
14	L3	C	19	356	504	31.8	19.6	12	229	270	12	12	150	45	135	60	735	535
15	EPB 1-1	M	12	227	318	20	10.7	7	150	180	10	10	105	50	60	50	355	235
16	EPB 2-1	M	12	227	318	20	10.7	7	150	180	10	10	105	50	60	50	355	235
17	EP 1-1	M	12	227	318	20	10.7	7	150	180	10	10	105	50	60	50	355	235
18	EP 2-1	M	12	227	318	20	10.7	7	150	180	10	10	105	50	60	50	355	235
19	Beam10	M	10	331	506	20	10.2	6.1	180	180	10	6	100	58	58	50	357	237
20	Beam12	M	12	306	510	20	10.2	6.1	180	180	10	6	100	58	58	50	357	237
21	Jenkins	M	15	275	-	20	13.7	7.7	167	200	6	6	120	55	55	60	355	235
22	S10	M	10	425	567	24	11.8	6.7	166	270	8	5	140	40	40	36	341	249
23	EP-1-8	M	8	250	-	16	13.1	7.7	140	140	8	6	80	50	50	40	350	240
24	EP-3-10	M	10	250	-	16	13.1	7.7	140	140	8	6	80	50	50	40	350	240
25	EP-4-10	M	10	250	-	16	13.1	7.7	140	140	8	6	80	70	70	40	370	220
26	4E	C	13	427	-	22	12.7	9.5	203	203	6	6	102	64	38	57	1429	1314
27	E36	M	23	320	-	28.6	16.7	10	260	260	6	6	152	51	51	35	455	335
28	E55	M	19	408	-	25.4	25	16	205	205	6	6	127	102	35	45	1650	1405
29	P4	M	10	295	418	20	10.7	7.1	150	150	6	6	90	30	30	30	350	285
30	JD1	M	12	763	796	27	12	10	180	200	10	10	100	50	50	50	345	233
31	JD2	M	12	763	796	27	12	10	180	200	10	10	100	50	50	50	345	233
32	BC1-1	M	12	332	496	20	11.8	6.7	166	200	10	10	124	50	50	70	351	239
33	BCJ-2	M	12	332	496	20	11.8	6.7	166	200	10	10	124	50	50	70	351	239
34	BCJ-4	C	12	332	496	20	11.8	6.7	166	200	10	10	124	50	50	70	351	239

#1-2: Özkılıç (2020a); #3-6: Coelho et al. (2004); #7-14: Adey et al. (1997); #15-18: Bursi and Jaspart (1997); #19-20: Adegoke (2009); #21: Shi et al. (1996); #22: Zhu et al. (2019); #23-25: Arul Jayachandran et al. (2009); #26: Summer (2003); #27: Abel and Murray (1994); #28: Borgsmiller et al. (1995); #29: Aleksander and Damian (2019); #30-31: Qiang et al. (2018); #32-34: Wang et al. (2018)

Table 4. Properties of experimented specimens for stiffened four bolted case.

#	Specimens	L	t_p	F_y	F_u	d_b	t_f	t_w	b_{fp}	b_p	t_s	w_f	w_w	w_s	g	p_{fi}	p_{fo}	d_e	h_o	h_i
1	SP9	C	12	325	388	24.0	9.8	6.2	120	150	10	10	10	10	85	40	45	35	280	185
2	SP10	C	10	313	387	24.0	9.8	6.2	120	150	10	10	10	10	85	40	45	35	280	185
3	M4	C	15.9	340	510	31.8	19.0	11.4	193	230	19	10	10	10	125	50	100	60	560	395
4	M6	C	15.9	340	510	31.8	19.0	11.4	193	230	19	10	10	10	125	50	100	60	560	395
5	L4	C	15.9	340	510	31.8	19.6	11.9	229	270	19	12	12	12	150	45	135	60	735	535
6	4ES	C	13	386	601	25.4	9.5	6.4	203	203	6	6	5	6	114	45	45	44	586	507
7	JC4	C	16	282	588	20.0	12.0	8.0	200	200	8	10	10	10	108	50	50	50	344	232
8	JC5	C	12	318	611	20.0	12.0	8.0	200	200	8	10	10	10	108	50	50	50	344	232

#1-2: Özkılıç (2020a); #3-5: Adey et al. (1997); #6: Ryan (1999); #7-8: Bu et al. (2019)

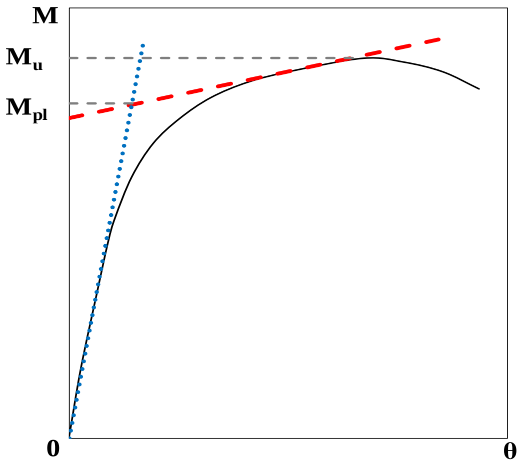

Fig. 5. Typical moment-rotation relationship.

Fig. 6 shows the comparison of the predicted and actual plastic moment capacities. The average ratios of actual plastic and predicted moment capacities are 1.27, 0.84 and 0.96 according to yield mechanisms of Srouji et al. (1983), Adey et al. (1997) and Özkılıç (2020a), respectively. The accuracy of the latter is better than those of formers. Except for three test specimens, the yield mechanism of Srouji et al. (1983) underestimates the plastic moment capacity. On the other hand, the yield mechanism of Adey et al. (1997) overestimates the plastic moment capacities except for 10 test specimens. It should also be mentioned that the yield mechanism of Adey et al. (1997) significantly overestimates plastic moment capacities of #14, 26 and 28 where the depth of the beam is relatively higher. This behavior is expected since the yield mechanism of Adey et al. (1997) extends the yield line up to 0.35 times the depth of the beam. Compared to those yield line mechanisms, the results of the yield line mechanism proposed by Özkılıç (2020a) give more balanced results.

The average ratio of ultimate moment capacity to moment capacity calculated using the yield line mechanism proposed by Srouji et al. (1983) is 1.92. The maximum ratio can reach 2.84, which is a significant underestimation of the ultimate capacity. The average ratios modify to 1.30 and 1.47 for the yield line mechanism proposed by Adey et al. (1997) and Özkılıç (2020a). The fact that the minimum ratio of ultimate moment capacity to moment capacity calculated using the yield line mechanism proposed by Srouji et al. (1983) is 1.03 indicates that for all cases this yield mechanism gives conservative results. The ratio of ultimate moment capacities to moment capacity predicted by Adey et al. (1997) for #14, 26 and 28 is significantly low due to the depth of the beam.

The relation between end-plate thickness and the ratio of actual ultimate and predicted moment capacities is shown in Fig. 7. It is seen that only for two cases the ratio is higher than 2.0 for the cases where thickness of end-plate is higher than 12 mm. On the other hand, the highest ratio is observed when the thickness of end-plate is 8 mm.

Table 6 shows the results for stiffened extended end-plated connections. Due to the very limited availability of experimental data for the stiffened case, the cases where the ratio of M_p/M_u is higher than 0.75 are also utilized provided that the main failure is related to the end-plate. The ratio of M_u/M_{pl} ranges between 1.46 and 1.93. A similar conclusion can be drawn also here that the stiffened extended end-plated connection can perform up to almost two times plastic moment capacity. The average ratios of predicted and actual plastic moment capacities are 1.16, 0.87 and 0.87 according to the yield mechanisms of Srouji et al. (1983), Adey et al. (1997) and Özkılıç (2020a), respectively. The prediction of Özkılıç (2020a) is slightly better than the others. This can also be seen in Fig. 8. On the other hand, the average ratios of ultimate plastic moment capacities and predicted capacities are 1.99, 1.36 and 1.48 according to the yield mechanisms of Srouji et al. (1983), Adey et al. (1997) and Özkılıç (2020a), respectively.

5. Numerical Study

Numerical study was conducted in order to evaluate further the prediction of the yield line mechanism for the parameters which did not particularly examined in the collected experimented specimens given in the previous section. Numerical analyses were performed using the finite element tool, ABAQUS. The experimental program conducted by Zhu et al. (2019) was adapted. After the verification model, a parametric study was carried out. Nonlinear geometry and material were considered. C3D8R type of elements was utilized for meshing all members. The end-plate was divided into four elements through the thickness, which was recommended by Özkılıç (2020b) in order to simulate the bending and buckling behavior accurately. Mesh sizes of 10 and 5 mm were utilized for the end-plate and bolts whereas a slightly larger mesh size of 20 mm was used for the beam and column face. The column was not modeled explicitly; instead, the column face was modeled in order to reduce computational cost. The welds were explicitly implemented in the model. Mesh configuration is depicted in Fig. 9. All degrees of freedom of the bottom surface of the column face were restrained. Loading was applied to the end of the beam where MPC constraint was defined. The finite sliding surface-to-surface contact with tangential contact behavior was defined to model contact between bolts and end-plate and between end-plate and the column face. The bolts were pre-tensioned using "Bolt Load" option in ABAQUS.

Table 5. Results for unstiffened extended end-plated connections.

#	M_{pl}	M_u	M_p	M_p/M_u	M_u/M_{pl}	M_S	M_A	$M_{\ddot{O}}$	M_{pl}/M_S	M_{pl}/M_A	$M_{pl}/M_{\ddot{O}}$	M_u/M_S	M_u/M_A	$M_u/M_{\ddot{O}}$
1	75	138	147	1.06	1.84	68	115	106	1.11	0.65	0.71	2.04	1.20	1.30
2	55	116	147	1.27	2.11	45	77	71	1.21	0.72	0.77	2.56	1.51	1.63
3	106	142	189	1.33	1.34	66	90	83	1.61	1.17	1.28	2.16	1.57	1.71
4	109	161	189	1.17	1.48	66	90	83	1.65	1.21	1.31	2.44	1.78	1.94
5	166	185	189	1.02	1.11	135	185	170	1.23	0.90	0.97	1.37	1.00	1.09
6	164	188	189	1.00	1.15	135	185	170	1.21	0.88	0.96	1.39	1.01	1.10
7	180	203	327	1.61	1.13	135	233	208	1.33	0.77	0.87	1.50	0.87	0.98
8	140	191	327	1.71	1.36	107	167	139	1.30	0.84	1.01	1.78	1.14	1.37
9	460	700	761	1.09	1.52	298	590	520	1.54	0.78	0.89	2.35	1.19	1.35
10	255	483	761	1.58	1.89	246	422	340	1.04	0.60	0.75	1.96	1.14	1.42
11	320	596	761	1.28	1.86	579	674	541	0.55	0.48	0.59	1.03	0.88	1.10
12	520	774	1310	1.69	1.49	437	838	719	1.19	0.62	0.72	1.77	0.92	1.08
13	344	551	1310	2.38	1.60	337	558	432	1.02	0.62	0.80	1.64	0.99	1.27
14	385	742	1310	1.77	1.93	504	938	731	0.76	0.41	0.53	1.47	0.79	1.01
15		94	272	2.89		58	75	69				1.63	1.26	1.36
16		96	169	1.76		58	75	69				1.67	1.28	1.39
17		120	168	1.40		58	75	69				2.08	1.61	1.74
18		98	168	1.71		58	75	69				1.70	1.31	1.42
19	80	158	216	1.37	1.98	61	75	70	1.32	1.07	1.15	2.60	2.12	2.27
20	96	155	216	1.39	1.61	81	99	93	1.19	0.97	1.04	1.92	1.56	1.67
21	150	198	233	1.18	1.32	114	128	126	1.32	1.17	1.19	1.74	1.54	1.57
22	152	245	252	1.03	1.61	91	180	137	1.67	0.84	1.11	2.69	1.36	1.78
23	43	80	143	1.79	1.86	28	38	33	1.53	1.14	1.32	2.84	2.12	2.46
24	61	112	143	1.28	1.84	44	59	51	1.39	1.03	1.20	2.54	1.90	2.20
25	52	96	143	1.49	1.85	39	49	43	1.34	1.06	1.20	2.47	1.95	2.21
26	850	1229			1.45	775	2193	986	1.10	0.39	0.86	1.59	0.56	1.25
27	476	681	1365	2.00	1.43	506	655	656	0.94	0.73	0.73	1.35	1.04	1.04
28	1836	1928	10002	5.19	1.05	1835	4917	2734	1.00	0.37	0.67	1.05	0.39	0.71
29	138	151	192	1.27	1.09	74	130	117	1.86	1.06	1.18	2.04	1.16	1.29
30	313	406	620	1.53	1.30	225	352	332	1.39	0.89	0.94	1.80	1.15	1.22
31	320	394	620	1.57	1.23	225	352	332	1.42	0.91	0.96	1.75	1.12	1.19
32	97	176	246	1.40	1.81	92	118	115	1.06	0.82	0.84	1.92	1.49	1.53
33	118	194	246	1.27	1.64	92	118	115	1.29	1.00	1.03	2.12	1.64	1.69
34	132	204	246	1.21		92	118	115	1.44	1.11	1.15	2.23	1.72	1.77
Mean	273	353	714	1.60	1.55	228	442	313	1.27	0.84	0.96	1.92	1.30	1.47
Min	43	80	143	1.00	1.05	28	38	33	0.55	0.37	0.53	1.03	0.39	0.71
Max	1836	1928	10002	5.19	2.11	1835	4917	2734	1.86	1.21	1.32	2.84	2.12	2.46

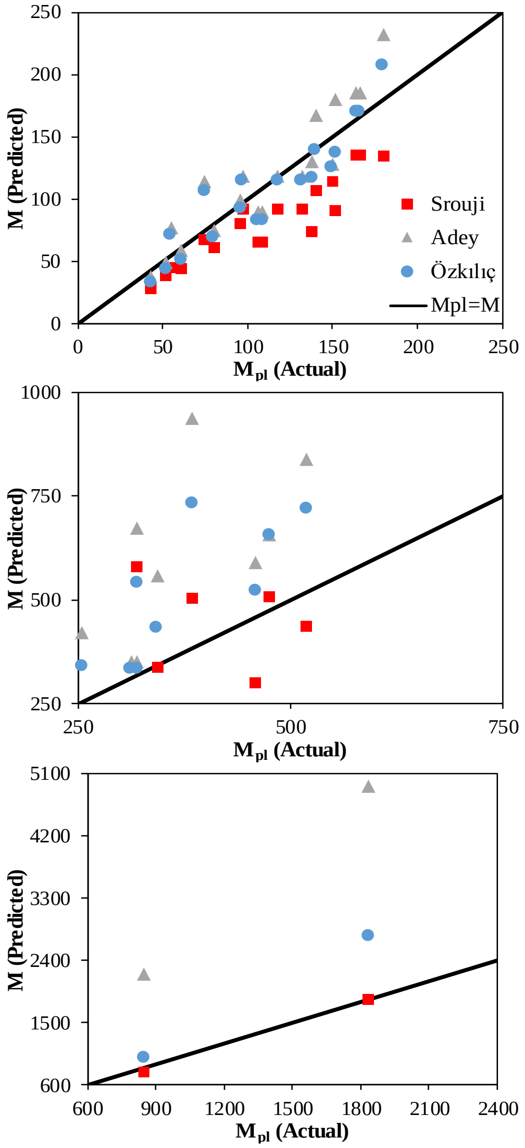

Fig. 6. The comparison of actual and predicted moment capacities for unstiffened cases.

In order to verify the assumed boundary conditions, mesh configuration and material model, the specimen S10BP of the study performed by Zhu et al. (2019) was simulated. This specimen is the same as with #22 specimen in Table 3 except that a backing plate was included, which resulted in an increase in the rigidity of the column face. For the verification model, the material properties of the specimen given by Zhu et al. (2019) were used. Fig. 10 compares the experimental findings and numerical results in terms of moment-rotation. It is observed that the numerical models exhibit slightly rigid behavior. This can be attributed to the behavior of the column which may act inelastic during the experiments. However, very slight differences of 4% and 5% between numerical and experimental results were observed for M_u and M_{pl} capacities, respectively. Fig. 11 demonstrates the failure mode at the end of the experiment at 0.10 rad rotation and PEEQ distribution at 0.10 rad rotation. In numerical models, high strain concentration was observed at the edge of the flange where failure was observed in the experiments. Moreover, the numerical model exhibited similar deformed shapes with the experimented specimen. Therefore, it can be concluded that a good agreement is observed between numerical and experimental findings.

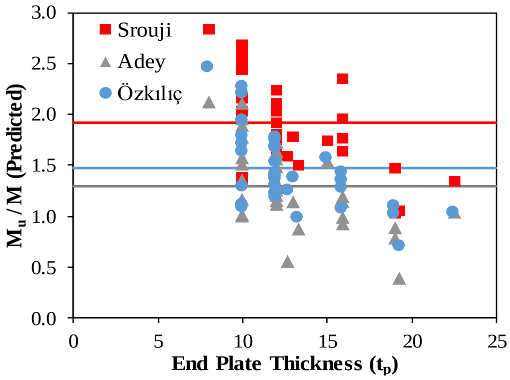

Fig. 7. The ratio of actual ultimate and predicted moment capacities.

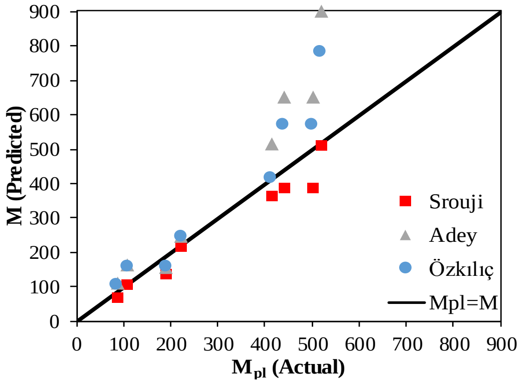

Fig. 8. The comparison of actual and predicted moment capacities for stiffened cases.

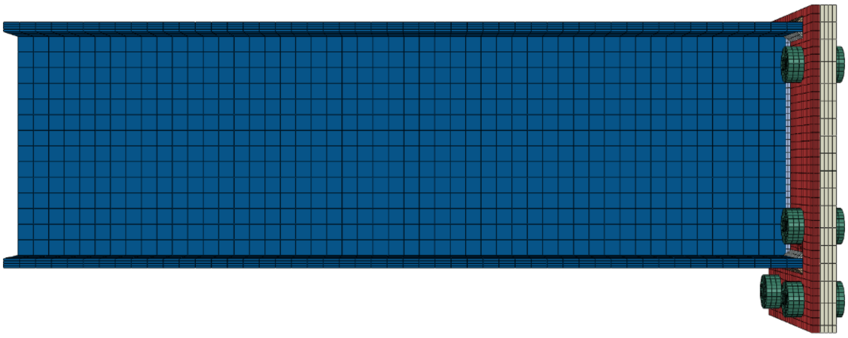

Fig. 9. Mesh configuration.

Table 6. Results for stiffened extended end-plated connections.

#	M_{pl}	M_u	M_p	M_p/M_u	M_u/M_{pl}	M_S	M_A	$M_Ö$	M_{pl}/M_S	M_{pl}/M_A	$M_{pl}/M_Ö$	M_u/M_S	M_u/M_A	$M_u/M_Ö$
1	109	191	147	0.77	1.75	104	165	157	1.04	0.66	0.69	1.83	1.16	1.22
2	87	168	147	0.87	1.93	70	110	105	1.25	0.79	0.83	2.41	1.53	1.60
3	502	734	761	1.04	1.46	386	654	569	1.30	0.77	0.88	1.90	1.12	1.29
4	440	796	761	0.96	1.81	386	654	569	1.14	0.67	0.77	2.06	1.22	1.40
5	520	999	1310	1.31	1.92	512	901	784	1.02	0.58	0.66	1.95	1.11	1.27
6	414	623	716	1.15	1.50	364	516	415	1.14	0.80	1.00	1.71	1.21	1.50
7	222	362	268	0.75	1.63	218	247	246	1.02	0.90	0.90	1.66	1.46	1.47
8	191	331	268	0.81	1.73	138	157	156	1.38	1.22	1.22	2.39	2.11	2.12
Mean	311	526	547	0.96	1.72	272	425	375	1.16	0.80	0.87	1.99	1.36	1.48
Min	87	168	147	0.74	1.46	70	110	105	1.02	0.58	0.66	1.66	1.11	1.22
Max	520	999	1310	1.31	1.93	512	901	784	1.38	1.22	1.22	2.41	2.11	2.12

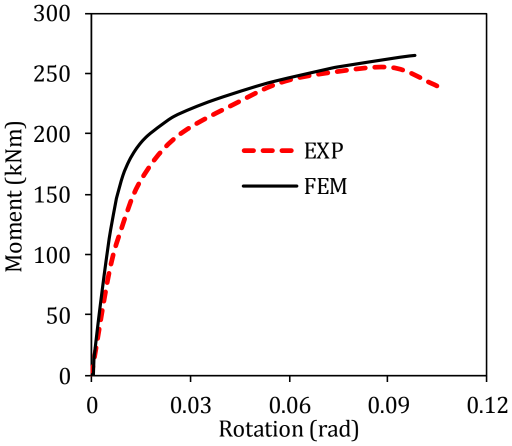

Fig. 10. Comparison of moment-rotation curves.

After the verification of the numerical model, a parametric study was conducted. The main aim of the parametric study was to explore the effects of the parameters on the accuracy of the yield line mechanisms. These parameters were selected based on the collected experimental data. The parameters which were not emphasized during the experiments were included in the parametric study. The parametric study was conducted for unstiffened and stiffened cases. A total of twenty models given in Table 7 were constructed. Models 1-10 were built for unstiffened cases whereas Models 11-20 were constructed for stiffened cases. Models 1 and 11 represent the reference models. Diameters of bolt were increased to 30 mm for Models 2 and 12. Gage distance was decreased to 100 mm for Models 3 and 13. Thickness of weld was double for Models 4 and 14. For Models 5 and 15, depth of beam was increased. Edge distance was increased to 60 mm for Models 6 and 16. Width of beam flange was increased to 250 mm for Models 7 and 17. Vertical distance from inside of a beam tension flange to nearest inside bolt row was reduced to 35 mm for Models 8 and 18 whereas vertical distance from inside of a beam tension flange to nearest outside bolt row was decreased to 35 mm for Models 9 and 19. Thickness of end-plate was reduced to 8 mm for Models 10 and 20.

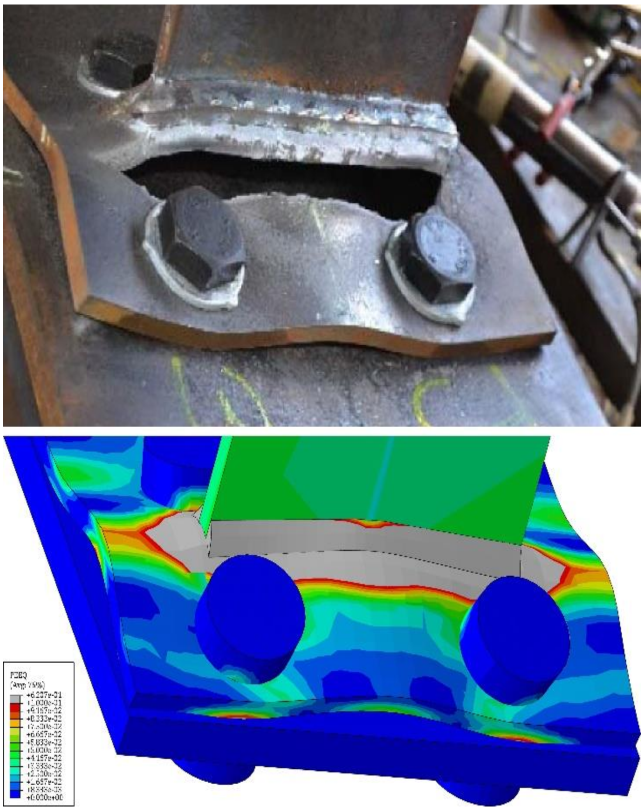

Fig. 11. Comparison of failure modes.

In the parametric study, the negative contribution of the beam, column and bolts to the capacity was eliminated. This was achieved by avoiding any failure or yielding of the bolts, beam and columns. Pursuant to this goal, yield strength of 235 MPa and 420 MPa were selected for the end-plate and beam, and the column face was modeled as elastic. Moreover, a slightly larger bolt diameter of 27 mm with 10.9 Grade was selected. The multilinear stress-strain curve recommended by Yun and Gardner (2017) was employed. Isotropic hardening was implemented to simulate the material model. The numerical modes were loaded up to 0.10 rad rotation which is the rotation capacity of the experimented specimen.

Table 7. Properties of experimented specimens for unstiffened four bolted case.

#	*Stif.*	t_p	d_b	t_f	t_w	b_{fp}	b_p	w_f	w_w	g	p_{fi}	p_{fo}	d_e	h_o	h_i
1	U	10	27	11.8	6.7	166	270	8	5	140	40	40	36	341	249
2	U	10	30	11.8	6.7	166	270	8	5	140	40	40	36	341	249
3	U	10	27	11.8	6.7	166	270	8	5	100	40	40	36	341	249
4	U	10	27	11.8	6.7	166	270	16	10	140	40	40	36	341	249
5	U	10	27	11.8	6.7	166	270	8	5	140	40	40	36	541	449
6	U	10	27	11.8	6.7	166	270	8	5	140	40	40	60	341	249
7	U	10	27	11.8	6.7	250	270	8	5	140	40	40	36	341	249
8	U	10	27	11.8	6.7	166	270	8	5	140	35	40	36	341	254
9	U	10	27	11.8	6.7	166	270	8	5	140	40	35	36	336	249
10	U	8	27	11.8	6.7	166	270	8	5	140	40	40	36	341	249
11	S	10	27	11.8	6.7	166	270	8	5	140	40	40	36	341	249
12	S	10	30	11.8	6.7	166	270	8	5	140	40	40	36	341	249
13	S	10	27	11.8	6.7	166	270	8	5	100	40	40	36	341	249
14	S	10	27	11.8	6.7	166	270	16	10	140	40	40	36	341	249
15	S	10	27	11.8	6.7	166	270	8	5	140	40	40	36	541	449
16	S	10	27	11.8	6.7	166	270	8	5	140	40	40	60	341	249
17	S	10	27	11.8	6.7	250	270	8	5	140	40	40	36	341	249
18	S	10	27	11.8	6.7	166	270	8	5	140	35	40	36	341	254
19	S	10	27	11.8	6.7	166	270	8	5	140	40	35	36	336	249
20	S	8	27	11.8	6.7	166	270	8	5	140	40	40	36	341	249

The parametric results for unstiffened extended end-plated connections are depicted in Table 8. The ratio of M_p/M_u is larger than 1.0 indicating that the extended end-plate connection reached its ultimate capacities without reaching the plastic moment capacity of the beam. The ratio of M_u/M_{pl} ranges between 1.37 and 1.57. It means that the extended end-plated connection can perform almost 1.5 times the plastic moment capacity. Similar to experimental data, a significant underestimation was observed in the ultimate capacity with an average range of 3.21 and 4.66.

Fig. 12 shows the comparison of the predicted and actual plastic moment capacities for the results of the unstiffened parametric study. The average ratios of actual plastic and predicted moment capacities are 3.83, 2.19 and 2.14 according to yield mechanisms of Srouji et al. (1983), Adey et al. (1997) and Özkılıç (2020a), respectively. For all cases, the yield mechanism of Srouji et al. (1983) significantly underestimates the plastic and ultimate moment capacity. The yield mechanisms of Adey et al. (1997) and Özkılıç (2020a) exhibited similar conservatism for both the plastic and ultimate moment capacities. Overall, the accuracy of the yield line mechanism of Özkılıç (2020a) is slightly better than that of Adey et al. (1997).

Table 9 shows the parametric results for stiffened extended end-plated connections. Similar to unstiffened case, the ratio of M_p/M_u is also larger than 1.0. The ratio of M_u/M_{pl} ranges between 1.29 and 1.57. A similar conclusion can be drawn also herein that the stiffened extended end-plated connection can perform up to almost 1.5 times plastic moment capacity. The average ratios of predicted and actual plastic moment capacities are 3.22, 2.23 and 2.22 according to the yield mechanisms of Srouji et al. (1983), Adey et al. (1997) and Özkılıç (2020a), respectively. The prediction of Özkılıç (2020a) is slightly better than the others. This can also be seen in Fig. 13. On the other hand, the average ratios of ultimate plastic and predicted moment capacities are 4.66, 3.24 and 3.21 according to yield mechanisms of Srouji et al. (1983), Adey et al. (1997) and Özkılıç (2020a), respectively. For the ultimate moment capacity, very high underestimation is also observed.

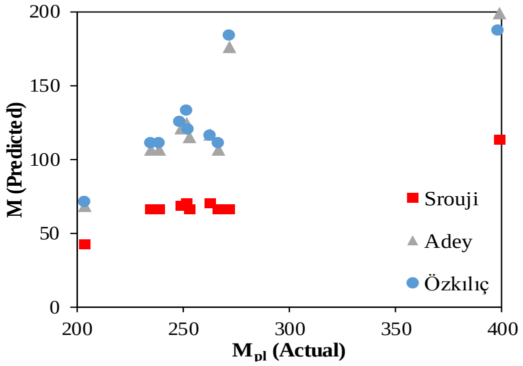

Fig. 12. The comparison of actual and predicted moment capacities for unstiffened cases.

Table 8. Results of the parametric study for unstiffened cases.

#	M_{pl}	M_u	M_p	M_p/M_u	M_u/M_{pl}	M_S	M_A	$M_{\ddot{O}}$	M_{pl}/M_S	M_{pl}/M_A	$M_{pl}/M_{\ddot{O}}$	M_u/M_S	M_u/M_A	$M_u/M_{\ddot{O}}$
1	235	349	415	1.19	1.48	66	107	111	3.54	2.19	2.12	5.25	3.25	3.14
2	253	373	415	1.11	1.47	66	116	120	3.81	2.18	2.11	5.61	3.22	3.11
3	263	372	415	1.12	1.41	71	117	116	3.72	2.25	2.28	5.26	3.17	3.22
4	272	374	415	1.11	1.37	66	177	184	4.10	1.54	1.48	5.63	2.12	2.04
5	399	614	767	1.25	1.54	114	199	187	3.50	2.00	2.13	5.40	3.08	3.28
6	239	351	415	1.18	1.47	66	107	111	3.60	2.23	2.15	5.28	3.27	3.16
7	267	400	415	1.04	1.50	66	107	111	4.02	2.49	2.41	6.03	3.73	3.61
8	249	355	415	1.17	1.43	69	121	125	3.62	2.05	1.99	5.16	2.93	2.84
9	252	358	415	1.16	1.42	70	125	133	3.59	2.01	1.90	5.10	2.86	2.70
10	204	323	415	1.28	1.59	42	69	71	4.80	2.97	2.87	7.61	4.72	4.56
Mean	263	387	450	1.16	1.47	70	125	127	3.83	2.19	2.14	5.63	3.24	3.16
Min	204	323	415	1.04	1.37	42	69	71	3.50	1.54	1.48	5.10	2.12	2.04
Max	399	614	767	1.28	1.59	114	199	187	4.80	2.97	2.87	7.61	4.72	4.56

Table 9. Results of the parametric study for stiffened cases.

#	M_{pl}	M_u	M_p	M_p/M_u	M_u/M_{pl}	M_S	M_A	$M_{\ddot{O}}$	M_{pl}/M_S	M_{pl}/M_A	$M_{pl}/M_{\ddot{O}}$	M_u/M_S	M_u/M_A	$M_u/M_{\ddot{O}}$
1	252	375	415	1.11	1.49	87	116	119	2.89	2.17	2.12	4.30	3.22	3.16
2	270	403	415	1.03	1.49	87	125	128	3.10	2.16	2.11	4.62	3.22	3.15
3	317	408	415	1.02	1.29	96	133	131	3.29	2.38	2.42	4.24	3.07	3.12
4	296	415	415	1.00	1.40	87	185	184	3.39	1.60	1.61	4.76	2.24	2.26
5	489	690	767	1.11	1.41	147	215	200	3.33	2.28	2.45	4.70	3.21	3.45
6	265	391	415	1.06	1.47	90	120	123	2.95	2.22	2.16	4.34	3.27	3.18
7	295	414	415	1.00	1.40	87	116	119	3.38	2.54	2.48	4.75	3.56	3.48
8	261	383	415	1.08	1.47	90	130	133	2.91	2.00	1.96	4.28	2.94	2.88
9	258	379	415	1.09	1.47	91	133	138	2.83	1.94	1.86	4.16	2.84	2.74
10	228	358	415	1.16	1.57	56	74	76	4.09	3.06	3.00	6.42	4.81	4.71
Mean	293	422	450	1.07	1.45	92	135	135	3.22	2.23	2.22	4.66	3.24	3.21
Min	228	358	415	1.00	1.29	56	74	76	2.83	1.60	1.61	4.16	2.24	2.26
Max	489	690	767	1.16	1.57	147	215	200	4.09	3.06	3.00	6.42	4.81	4.71

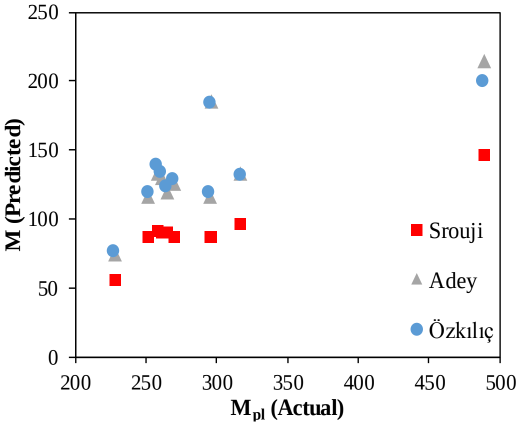

Fig. 13. The comparison of actual and predicted moment capacities for stiffened case.

6. Conclusions

In this present study, three different yield mechanisms are evaluated for both stiffened and unstiffened four bolt extended end-plated connections. Pursuant to this goal, a total of 42 experimental data is collected from 14 different studies and a parametric numerical study using ABAQUS was performed. Numerical models are capable of predicting the behavior of the extended end-plated connections. The following conclusions can be drawn based on the collected data and the parametric study:

- The prediction of plastic moment capacity by yield line mechanisms for stiffened extended end-plated connections is more accurate than that of unstiffened extended end-plated connections.

- The ultimate capacity of extended end plate connection can be averagely up to twice the plastic moment capacity.
- A general trend is observed that as the thickness of end-plate reduces, the ratio of actual moment capacities to predicted moment capacities increases. This behavior is further needed to be detailed examined.
- One should be careful about the depth of the beam while using the yield mechanism of Adey et al. (1997). If the depth of the beam is relatively high, the yield mechanism significantly overestimates the capacity.
- Numerical results revealed that the underestimation of the capacity can significantly be increased when any failure or yielding of the bolts, beam and columns is eliminated.
- The yield line mechanism proposed by Srouji underestimates the capacity. This yield mechanism is currently used by AISC 341-16 Seismic Provisions for Structural Steel Buildings with a safety factor of 0.9 which makes it more conservative.
- Among three yield mechanisms, the yield mechanism proposed by Özkılıç (2020a) gives more accurate estimation of the moment capacity. If this yield line mechanism is adopted in the guidelines (AISC 358 or TBEC 2018), it is recommended to use safety factor of 0.9 (0.9x1.67 for ASD) to predict plastic moment capacity while it is advised to utilize 1.25 (1.25x1.67 for ASD) overstrength factor to predict ultimate moment capacity.
- Based on the results of the parametric study, for future studies a new yield line mechanism to predict unstiffened and stiffened extended end-plated connections to be developed is recommended.

REFERENCES

Abel MSM, Murray TM (1994). Analytical and Experimental Investigation of the Extended Unstiffened Moment End-plate Connection with Four Bolts at the Beam Tension Flange. Jr. Department of Civil Engineering, Structures and Materials Research Laboratory, Virginia Polytechnic Institute and State University.

Adegoke IO (2009). Ductility of Thin Extended Endplate Connections. *Ph.D thesis,* University of the Witwatersrand, Johannesburg.

Adey BT, Grondin GY, Cheng JJR (1997). Behaviour of extended end plate moment connections under cyclic loading. Structural Engineering Report No. 216, Department of Civil and Environmental Engineering, University of Alberta, Edmonton, Alta.

AISC 341–16 (2016). Seismic Provisions for Structural Steel Buildings. American Institute of Steel Construction, Chicago, IL.

AISC 358–16 (2016). Prequalified Connections for Special and Intermediate Steel Moment Frames for Seismic Applications. American Institute of Steel Construction, Chicago, IL.

Akgönen Aİ, Güneş B (2017). Alın levhalı moment birleşimlerin sonlu elemanlar ile analizi. *Afyon Kocatepe Üniversitesi Fen ve Mühendislik Bilimleri Dergisi*, 17(2), 646-657. (in Turkish)

Aleksander K, Damian K (2019). Experimental tests of steel unstiffened double side joints with flush and extended end plate. *Archives of Civil Engineering*, 65(4), 127-154.

Arul Jayachandran S, Marimuthu V, Prabha P, Seetharaman S, Pandian N (2009). Investigations on the behaviour of semi-rigid endplate connections. *Advanced Steel Construction*, 5(4), 432-451.

Borgsmiller JT (1995). Simplified Method for Design of Moment End-Plate Connections, *M.Sc Thesis*, Virginia Polytechnic Institute and State University, Blacksburg, Virginia.

Borgsmiller J, Sumner E, Murray T (1995). Tests of Extended Moment End-Plate Connections Having Large Inner Pitch Distances. Research Report CE/VPI-ST-95/01 Department of Civil Engineering. Virginia Polytechnic Institute and State University. Blacksburg VA.

Bu Y, Wang Y, Zhao Y (2019). Study of stainless steel bolted extended end-plate joints under seismic loading. *Thin-Walled Structures*, *144*, 106255.

Bursi OS, Jaspart JP (1997). Calibration of a finite element model for isolated bolted end-plate steel connections. *Journal of Constructional Steel Research*, 44(3), 225-262.

Chasten CP, Lu LW, Driscoll GC (1992). Prying and shear in end-plate connection design*. Journal of Structural Engineering, ASCE*, 118(5), 1295-1311.

Coelho AMG, Bijlaard FS, da Silva LS (2004). Experimental assessment of the ductility of extended end plate connections. *Engineering Structures*, 26(9), 1185-1206.

Hendrick DM, Kukreti AR, Murray TM (1985). Unification of Flush End-Plate Design Procedures. Research Report No. FSEL/MBMA 85-01, Fears Structural Engineering Laboratory, School of Civil Engineering and Environmental Science, University of Oklahoma, Norman, Oklahoma.

Karasu A, Vatansever C (2021). Experimental study on the behavior of header end-plate connections under cyclic loading. *Teknik Dergi*, 32(6).

Kennedy NA, Vinnakota S and Sherbourne AN (1981). The split-tee analogy in bolted splices and beam-column connections. *Proceedings of the International Conference: Joints in Structural Steelwork: The Design and Performance of Semi-Rigid and Rigid Joints in Steel and Composite Structures and Their Influence on Structural Behaviour*, Teesside Polytechnic, Middlesbrough, Cleveland, England, 2.138-2.157.

Mann AP, Morris LJ (1979). Limit design of extended endplate connections. *ASCE Journal of Structural Engineering*, 105(ST3), 511–526.

Murray TM (1988). Recent developments for the design of moment end-plate connections. *Steel Beam-to-Column Building Connections*, Chen WF, ed., Elsevier Applied Science, New York, 133-162.

Murray TM (1990). AISC Design Guide 4, Extended End-Plate Moment Connections, American Institute of Steel Construction, Chicago.

Murray TM, Shoemaker WL (2002). Steel Design Guide 16, Flush and Extended Multiple-Row Moment End-Plate Connections, American Institute of Steel Construction, Chicago, IL.

Özkılıç YO (2020a). Experimental and Numerical Studies on Replaceable Links for Eccentrically Braced Frames. *Ph.D thesis*, Middle East Technical University, Ankara, Turkey.

Özkılıç YO (2020b). A new replaceable fuse for moment resisting frames: Replaceable bolted reduced beam section connections. *Steel and Composite Structures*, 35, 353-370.

Özkılıç YO (2021). Investigation of the effects of bolt diameter and end-plate thickness on the capacity and failure modes of end-plated beam-to-column connections. *Research on Engineering Structures & Material*, In-Press.

Özkılıç YO, Topkaya C (2021a). Extended end-plate connections for replaceable shear links. *Engineering Structures*, 240, 112385.

Özkılıç YO, Topkaya C (2021b). The plastic and the ultimate resistance of four-bolt extended end-plate connections. *Journal of Constructional Steel Research*, 181, 106614.

Qiang X, Wu N, Luo Y, Jiang X, Bijlaard F (2018). Experimental and theoretical study on high strength steel extended endplate connections after fire. *International Journal of Steel Structures*, 18(2), 609-634.

Packer JA, Morris LJ (1977). A limit state design method for the tension region of bolted beam column connections. *The Structural Engineer*, 55(10): 446–458.

Ryan JC (1999). Evaluation of extended end-plate moment connections under seismic loading. *Ph.D thesis,* Virginia Tech, United States.

Sağıroğlu M (2018). Kiriş gövdesinde berkitmeli alın levhalı birleşimlerin davranışının deneysel analizi. *Sakarya University Journal of Science*, 22(2), 502-508. (in Turkish)

Shi YJ, Chan SL, Wong YL (1996). Modeling for moment-rotation characteristics for end-plate connections. *Journal of Structural Engineering*, 122(11), 1300-1306.

Srouji R, Kukreti R, Murray T (1983). Yield-Line Analysis of End-Plate Connections with Bolt Force Predictions. Research Report FSEL/MBMA 83-05 Fears Structural Engineering Laboratory, University of Oklahoma, Norman OK.

Sumner EA (2003). Unified design of extended end-plate moment connections subject to cyclic loading. *Ph.D thesis,* Virginia Tech, United States.

Sumner EA, Murray TM (2001). Experimental Investigation of the MRE 1/2 End-Plate Moment Connection, Research Report No. CE/VPI-ST-01/14, submitted to Metal Building Manufacturers Association, Cleveland, Ohio.

Sumner EA, Murray TM (2002). Behavior of extended end-plate moment connections subject to cyclic loading. *Journal of Structural Engineering,* 128(4), 501-508.

Surtees J, Mann A (1970). End plate connections in plastically designed structures. C*onference on Joints in Structures: Institution of Structural Engineers,* University of Sheffield, United Kingdom.

TBEC (2018). Turkish Building Earthquake Code. Turkey Ministry of Interior Disaster and Emergency Management Authority, Ankara, Turkey.

Yılmaz O, Bekiroğlu S (2016). Alın levhalı bulonlu kolon kiriş birleşimlerinde panel bölgesi güçlendirmesinin etkisi. *Gazi Üniversitesi Mühendislik-Mimarlık Fakültesi Dergisi*, 31(2). (in Turkish)

Yun X, Gardner L (2017). Stress-strain curves for hot-rolled steels. *Journal of Constructional Steel Research*, 133, 36-46.

Wang J, Uy B, Thai HT, Li D (2018). Behaviour and design of demountable beam-to-column composite bolted joints with extended endplates. *Journal of Constructional Steel Research*, 144, 221-235.

Whittaker D, Walpole WR (1982). Bolted end plate connections for seismically-designed steel frames. Research Report No. 82-11, Department of Civil Engineering, University of Cantebury, Christchurch, New Zealand, 88–92.

Zhu C, Rasmussen KJ, Yan S, Zhang H (2019). Experimental full-range behavior assessment of bolted moment end-plate connections. *Journal of Structural Engineering*, 145(8), 04019079.

CHALLENGE JOURNAL OF STRUCTURAL MECHANICS 7 (2) (2021) 107–116

Research Article

Assessment of an old roadway bridge under static and seismic loading conditions

Mehmet Fatih Yılmaz [a], Abdulkadir Cüneyt Aydın [b,*]

[a] *Department of Civil Engineering, Ondokuz Mayıs University, 55139 Samsun, Turkey*
[b] *Department of Civil Engineering, Atatürk University, 25240 Erzurum, Turkey*

ABSTRACT

A large proportion of road and railway bridges, present in Turkey served for many years, have been completed their service life or will soon. Continuing safety and sustainability of these bridges under traffic loads have been of great increasing importance to roadway and railway transportation line to be continuous servicing. In addition, the demolition and reconstruction of bridges that have reached the end of their service life or are nearing completion will have a negative impact on the country's economy. All of these requirements' detailed examination of bridges in order to provide economical and safe service, considering current vehicle loads and earthquake loads. The Mahmutçavuş Bridge is investigated as a simply supported continuous composite roadway bridge at this work. The finite-element model of the bridge is constituted by site investigation and measurement. Different truckloads using for the design of the bridge are determined, and static analysis of the bridge is conducted. Seven earthquake records are scaled for two different earthquake design spectrums. The nonlinear time-history analyses are conducted, considering Δ-δ effects. The performance of the bridge for varying truckloads and earthquake loads is investigated, and results are discussed in detail.

ARTICLE INFO

Article history:
Received 3 December 2020
Revised 20 January 2021
Accepted 2 March 2021

Keywords:
Roadway bridge
Steel composite bridge
Time-history analysis
Pushover analysis

1. Introduction

Turkey has in the past experienced major earthquakes and, consequently, significant structural, life, and property losses (Damci et al., 2015; Inel et al., 2008; Korkmaz et al., 2010; Tolon and Mızrak, 2017). The disasters in the past have shown that timely delivery to the exposure areas is important as the damage occurs to the structure, and many urgent intervention plans are prepared for quick implementation in the area. Highway lines are the most basic transportation network used in transportation to disaster areas. For this reason, the fact that road transport systems continue to be functional after natural disasters are of great importance in order that disaster areas can be reached quickly and that necessary intervention can be made on time. Bridges are the vulnerable components of the transportation system, and due to economic reasons, the existing system needs to be used as long as possible, and its safety is ensured. The long service life and increasing traffic load require more detailed investigation on the roadway bridge to sustain the safe and economical servicing of the road.

Erzurum Province includes many active seismic faults and has been exposed to devastating earthquakes in the near past; Horasan-Narman 1983 (Ms=6.8), Erzurum 1859, Erzurum 1901 (MS=6.1), Horasan 1924 (Ms=6.8), Hinis (Erzurum) 1952 (Ms=5.6), Horasan-Narman 1983 (Ms=6.7), Balkaya 2984 (Mb=6.4), Şenkaya 1999 (MI=5.1), Aşkale 2004 (Ms=5.3). Because of these major earthquakes, much loss of life and property was experienced. In order to prevent loss of life and property, the earthquake performance of existing structures and bridges in the Erzurum region should be determined. Past earthquakes show that bridges are vulnerable components of the roadway system with regard to seismic

---

* *Corresponding author.* Tel.: +90-442-231-4781 ; Fax: +90-442-231-4910 ; E-mail address: acaydin@atauni.edu.tr (A. C. Aydın)
ISSN: 2149-8024 / DOI: https://doi.org/10.20528/cjsmec.2021.02.006

damage, and the main reason for damage in steel bridges essentially originates from buckling, extremely low-cycle fatigue, tension, shearing break, and damage to supports (Usami and Ge, 2009; Rokneddin et al., 2014). Past design criteria for roadway bridges do not include seismic load, and with an increase in vehicle loads, questions are starting to be asked regarding whether or not the performance of old roadway bridges is sufficient and safe. Also, bridges lose design load-carrying capacity due to many different aging phenomena, such as corrosion of steel bridge components, which is one of the well-known deterioration processes seen on bridges, and damage occurring after natural hazards (Ghosh and Padgett, 2010). Because of the deterioration of bridges and design that does not consider seismic code, the bridges are vulnerable to seismic events, and many different retrofitting methods are updated and used to increase the safety of these bridges (Usami et al., 2005). Besides, the Economical design of bridges for different truckloads and different beam configurations was investigated, which is essential for the financial growth of the civilization (Atmaca, 2019).

The seismic performance of bridges is determined using a mathematical model of the bridge. There are three analytical methods used for the seismic assessment of bridges: Static analysis, pushover analysis, and time history analysis. Static analysis is essentially used to calculate the live load acting on the bridge and increase the traffic load with a constant to determine the dynamic effect of the load and apply seismic load as a lateral static load and equivalent earthquake load method and mod shape assembly method. Pushover analysis and time history analysis are conducted to determine the seismic performance of the bridge. Pushover analysis applies a fundamental modal load to the bridge system and increases the load until a target displacement or collapse of the bridge and gives conservative results (Lu et al., 2004; Zheng et al., 2003). Time history analysis (THA) gives more realistic results but requires more time and computational efforts. However, with advances in computer technology, THA is beginning to be used in seismic assessment of structures and bridge systems (DesRoches et al., 2004; Nielson and DesRoches, 2007; Padgett and DesRoches, 2008; Saadeghvaziri and Yazdani-Motlagh, 2008). In addition to lateral seismic force, vertical seismic force is also critical to determine the seismic performance of the bridge, and recent seismic code has started to consider vertical ground motion in bridge design (Kunnath et al., 2008).

These studies investigate an existing bridge that was serviced until 1961. A finite element model using site investigation and finite element model is constituted. A different truckload is applied to the model to determine the highest moment occurring in the superstructure and the maximum displacement in the span. Seven seismic records are used for time history analysis with matching spectral response acceleration for 2% and 10% aceding probability for a 50-year period. Damage in the bridge column, steel girders, and bridge bearings are investigated. Location and progress of damages are determined according to the pushover-analysis. The weakest component of the bridge is determined according to the time history analysis. Spectral acceleration of scaled earthquake records shows that the record has different acceleration values for higher frequency from the 475-year design spectrum but closer values for the 2475-year design spectrum. Bridge components performance is determined considering both earthquake scenarios.

2. Description of the Bridge

Mahmutçavuş Bridge is located 400 km from Pasinler, Oltu, Narman National roadway, on the Kışla village roadway. The bridge is a typical multi-span continuous steel roadway bridge. The first and last spans of the bridge are 10 m long, and the middle span of the bridge is 12 m long. The total length of the bridge is 56 meters, and the total width of the bride is 5.4 meters. The bridge is in service since its construction time in 1961. There are two gravity abutments and four steel piers on which the superstructure is positioned. A composite steel section and concrete slabs are used to constitute the superstructure of the bridge, while elastomeric fixed bearings are positioned at the middle piers, and elastomeric expansion bearings are positioned at the abutments. The piers of the bridge are constituted by welding two IPN240 steel sections, and each pier is composed of four columns. The width of the bend beam is 52 cm, and the height of the bend beam is 58 cm. Fig. 1 shows the general view of the bridge, and Fig. 2 shows the section view of the bridge. The superstructure of the bridge is composed of 5 IPN360 steel beams and concrete slabs. The bridge overpasses the Norman stream, and the water height of the river changes seasonally. In winter, only one pier of the bridge is underwater, but in spring and summer, all piers of the bridge are exposed to water. The total height of the bridge piers is 4m, but because of soil accumulation in the river, half of the columns are placed under accumulated soil.

3. Finite Element Model

A finite element model of the bridge is constituted by Sap2000 finite element software according to site investigation and measurement. Because of the construction date of the bridge, there is no available shop drawing and design project. Therefore, all sections and distances are measured on-site, and the finite element models of the bridge are constituted. Two node beam elements are used to model the piers, and the superstructure and 4-node shell elements are used to model the concrete slab. The supports are modeled using nonlinear link elements. The friction coefficient between the bearings and supports are calculated as for elastomeric pads and modeled with a friction link. Fig. 3 shows a 3D finite element model of the bridge, Fig. 4 shows the actual photograph of the bridge, and Fig. 5 shows the hysteresis model of fixed and elastomeric expansion bearings.

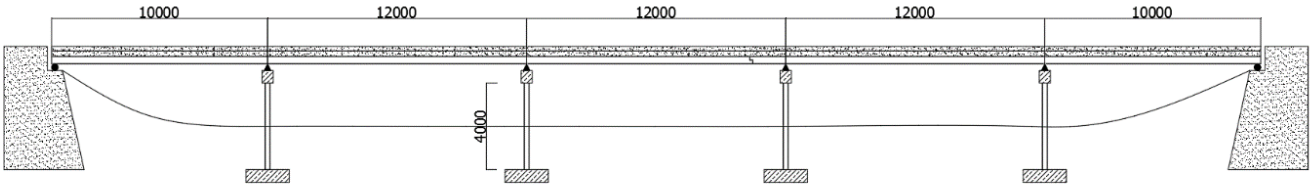

Fig. 1. General view of MSC composite bridge.

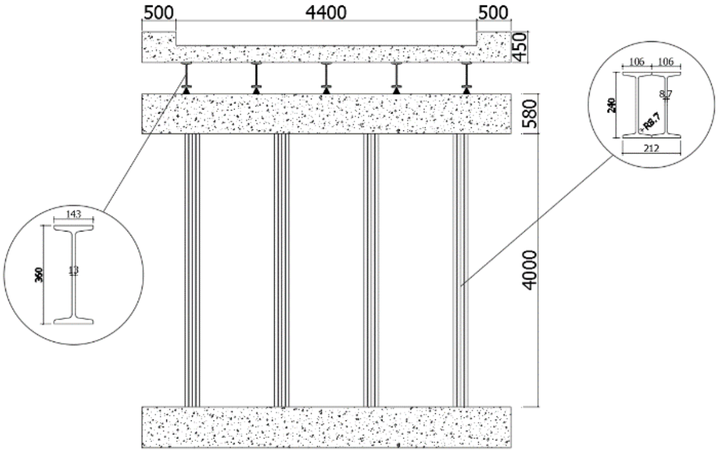

Fig. 2. Section view of MSC composite bridge.

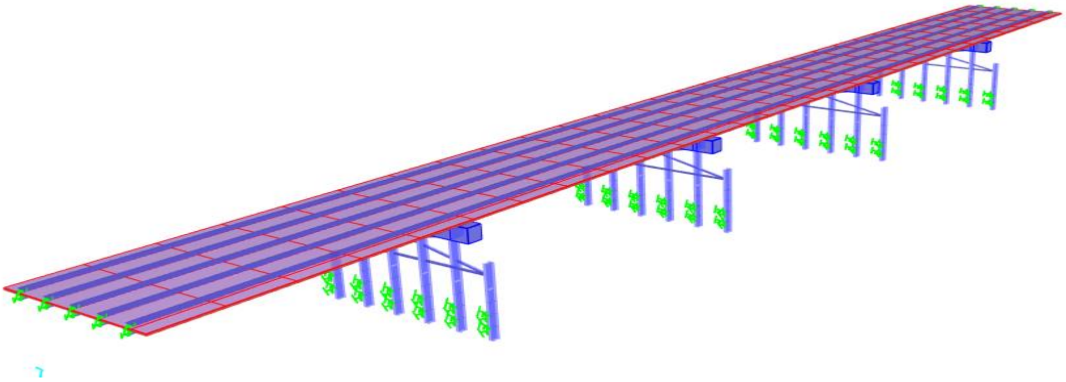

Fig. 3. 3D finite element view of MSC steel roadway bridge.

Fig. 4. Photograph of the bridge.

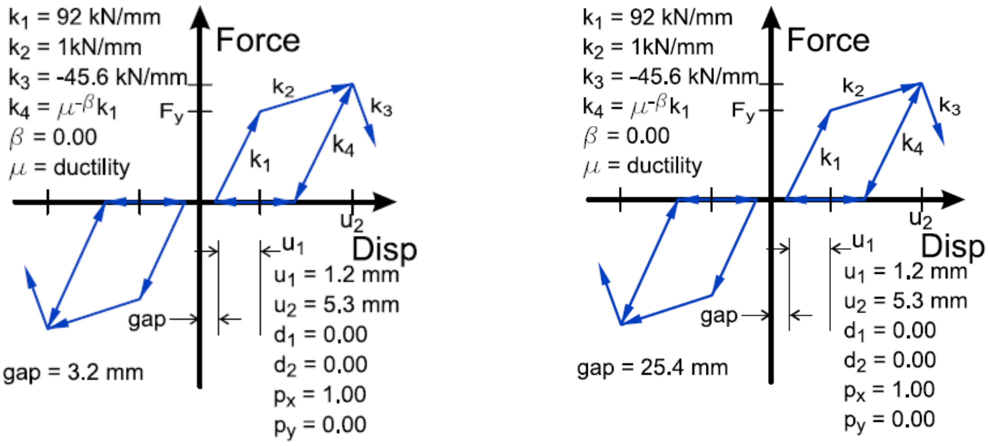

Fig. 5. Hysteresis models of: a) Fixed elastomeric bearing; b) Expansion elastomeric bearing (Nielson, 2005).

Since there is no specimen test for these MSC bridges, the material properties are obtained from previous studies in the literature. Yields and ultimate strengths are given for European railway and roadway bridges and are considered as MPa and MPa, respectively (Larsson and Lagerqvist, 2009). Both material and geometric nonlinear behaviors of bridges are considered in this study.

To conduct nonlinear time history analysis and pushover analysis, a finite element model of the bridge is constituted using Seismostruct finite element software. Material nonlinearity is defined by nonlinear hysteretic material modeling (Fig. 6) and the spread fiber model. Geometric nonlinearity is considered as *P*-Δ large displacement. Modal properties for the Mahmutçavuş Bridge are illustrated in Table 1. The first mod of the bridge is an effective mod and represents 55% of the longitudinal mass. The second, third, and fourth modes constitute transverse mods, which represent 82% of the bridge transverse mass and the periods of these mods change between 0.27s to 0.33s. The dominant vertical mod is also calculated. The modal participation mass ratio for the dominant vertical mod is 0.44, and the period is 0.098s.

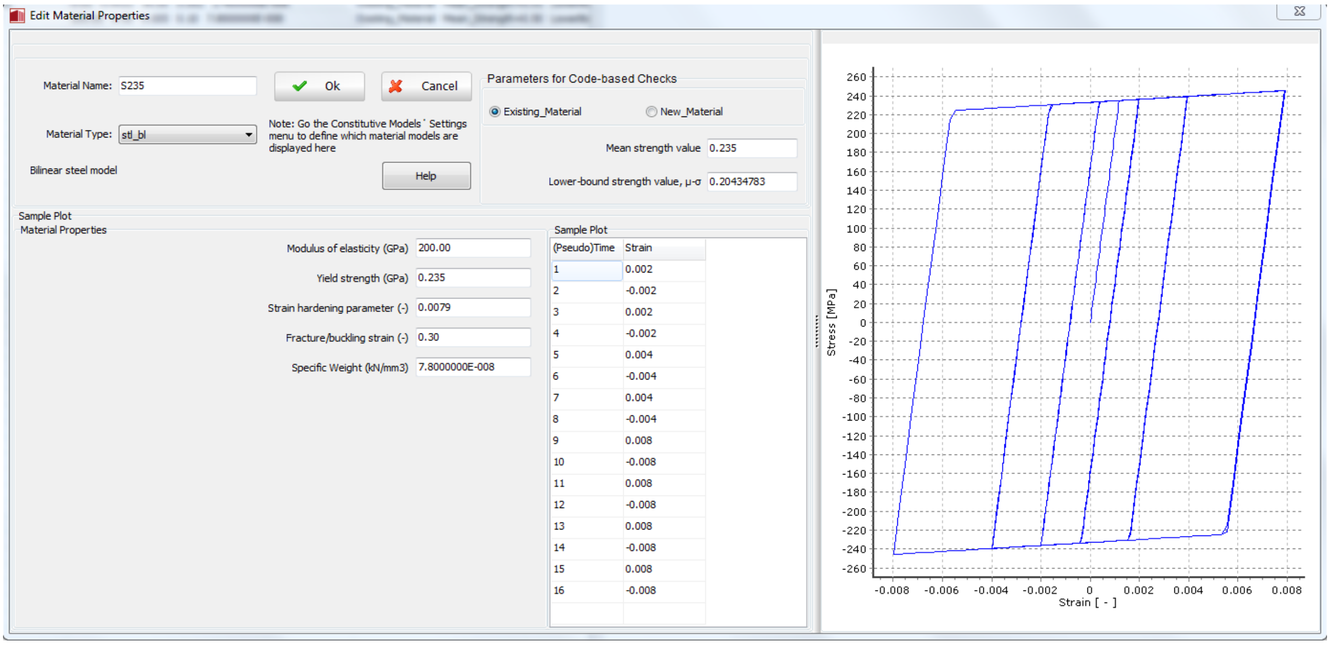

Material Name: S235

Material Type: stl_bl

Note: Go the Constitutive Models' Settings menu to define which material models are displayed here

Bilinear steel model

Parameters for Code-based Checks

● Existing_Material ○ New_Material

Mean strength value 0.235

Lower-bound strength value, μ-σ 0.20434783

Sample Plot

Material Properties

Modulus of elasticity (GPa) 200.00

Yield strength (GPa) 0.235

Strain hardening parameter (-) 0.0079

Fracture/buckling strain (-) 0.30

Specific Weight (kN/mm3) 7.8000000E-008

Sample Plot

(Pseudo)Time	Strain
1	0.002
2	-0.002
3	0.002
4	-0.002
5	0.004
6	-0.004
7	0.004
8	-0.004
9	0.008
10	-0.008
11	0.008
12	-0.008
13	0.008
14	-0.008
15	0.008
16	-0.008

Fig. 6. Hysteretic steel material model.

Table 1. Modal properties for MSC steel girder bridge.

Mode Number	Period	Longitudinal	Transverse	Vertical
First	0.4937	0.5487	0	0
Second	0.3336	0	0.4023	0
Third	0.2930	0	0.1058	0
Fourth	0.2759	0	0.3119	0
Twelfth	0.0987	0	0	0.4432

4. Loading of the Bridge

Mahmutçavuş Bridge is designed with H15-44 truckload, as illustrated in Fig. 7. In AASHTO (1935) specification, there are H15-44, H20-44, HS15-44, and HS20-44 truckloads used in the design of the bridge, considering the weight of the truck. In addition to this truckload, 9.35kN/m (240 flp), the continuous load is applied to the structure as mentioned in AASHTO (1935). The one-line truckload is applied to two longitudinal steel girders, and maximum displacement, maximum positive moment, and maximum negative moment are recorded as a result of static analysis.

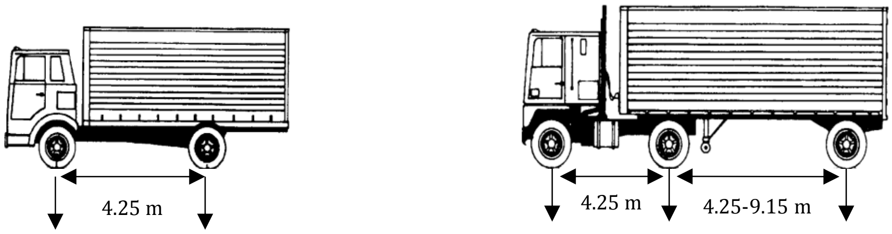

H15-44	30 kN	120 kN	HS15-44	30 kN	120 kN	120 kN
H20-44	40 kN	160 kN	HS20-44	40 kN	160 kN	160 kN

Fig. 7. Design truck load (HL-93, Caltrans).

AASHTO also developed an impact factor to increase the live load to account for the bounce and sway of vehicles, and the formulation is shown in Eq. (1). L is the length of the bridge span in feet.

$$I = \frac{50}{L+125} \le 0.3 \tag{1}$$

Using Eq. (1), the impact factor for 10m span and 12m span is calculated as 0.31 and 0.30, respectively. According to these calculations, the live load needs to be increased by 30%.

Maximum displacement and moments calculated in the bridge span under truckload are illustrated in Table 2. According to AASHTO specifications, the maximum permitted displacement is 15mm ($L/800$). The calculated vertical displacement in the bridge span changes between 29.06 mm and 41.89 mm and does not satisfy the specification limits. The maximum positive moment in the steel girder changes between 107.93 kN/m and 149.105 kN/m, and the minimum moment in the steel girder bridge changes between -118.47 kN/m and -176.22 kN/m. According to these moments, the maximum compression and tension stress in the steel girder beam change between 118.67 N/mm^2 and 193.75 N/mm^2. The examined stress is very close to the steel yielding stress limits. To the safety of the bridge transportation, detailed measurement and investigation should be done, and the serves load of the bridge should be limited before these measurement and further repair activities.

Table 2. Maximum displacement and moment calculated on the bridge span.

	Max Displacement (mm)	Max Moment (kN/m)	Min Moment (kN/m)
H15-44	34.30	139.03	-176.22
H20-44	41.89	149.105	-173.61
HS15-44	29.06	107.93	-118.47
HS20-44	35.10	128.48	-146.38

5. Pushover Analysis of the Bridge

Static pushover analysis in the transverse direction is conducted to determine the nonlinear behavior of the bridge. Lateral loads are applied to the bridge superstructure. Material nonlinearity is modeled with a spread fiber plastic hinge. Nonlinear material is modeled using a bilinear steel model. Geometric nonlinearity is considered with Δ-δ large displacement. Transverse displacement limits are assumed to be 20% off pier height, and the structure is pushed at the displacement limits. Fig. 8 shows the pushover curve and plastic hinge occurring in the bridge.

When the peak displacement reaches 16mm, the first plastic hinges occur at the brace member. When the peak displacement reaches 32 mm, the plastic hinge of the second and third bridge piers began to occur in the areas where the soil came into contact with the piers. As the horizontal displacement increases further, the plastic hinges are formed at the upper ends of the bridge piers and in the regions where the brace connects to the bridge piers. In the idealized force-displacement diagram in Fig. 8, the yielding displacement of the bridge is calculated as 38.13mm with 3380 kN base shear. For two types of design spectrums: level 1

(2% exceedance possibility for 50 years) and level 2 (10% exceedance possibility for 50 years), target displacements are calculated as 45.36mm and 22.79 mm, respectively. The bridge is pushed until the top displacement reaches 800mm, and the deform shape of the bridge is shown in Fig. 9. Using the deform shape of the bridge, lateral displacement at the top of all piers can easily be calculated.

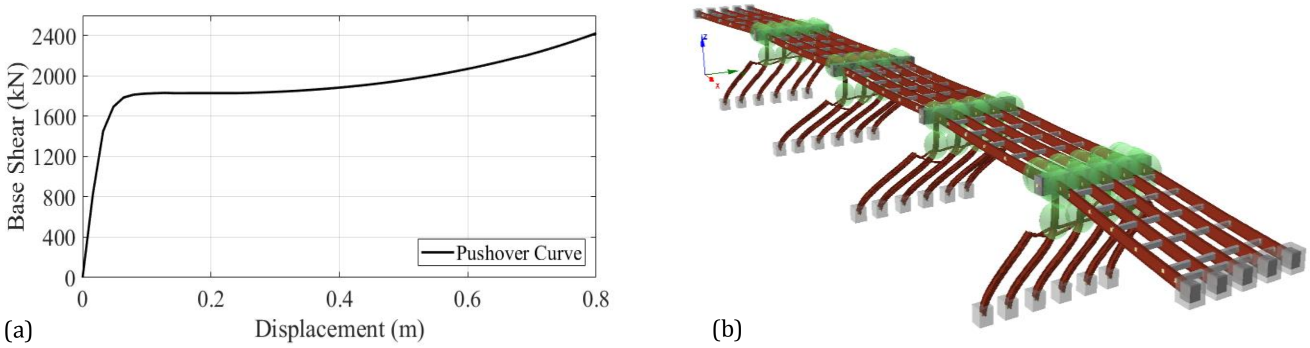

Fig. 8. Pushover analysis of Mahmutçavuş Bridge:
a) Pushover curve; b) 3D view of the location of the plastic hinges on the bridge.

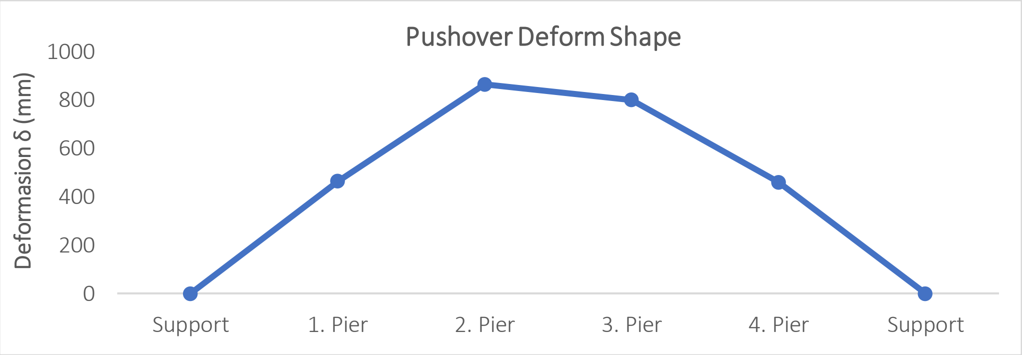

Fig. 9. Deform shape of the bridge under pushover analysis.

6. Time-History Analysis of the Bridge

Erzurum is located in a seismically active area of Turkey, and many catastrophic seismic events have occurred. 1901, Erzurum (Ms=6.1), 1924 Horasan (Ms=6.8), 1983, Horasan-Narman (Ms=6.8), 1984, Balkaya (Erzurum) (Ms=6.4) earthquakes are some of the devastating seismic events that have occurred in Erzurum Province. The investigated MSC bridge is located at the coordinates of 400, 20', 28" N, and 410,54', 56" E. According to Turkish Seismic Risk Maps, short-period spectral acceleration (S_(a_0.2s)) and long-period spectral acceleration (S_(a_1.0s)) values are obtained as 0.718g and 0.181g for 10% existing possibility for 50 years and 1.368g and 0.340g for 2% existing possibility for 50 years respectively.

Seven different strike-slip earthquake records are selected from Erzurum and other seismic areas and scaled to a design spectrum specified in the Turkish seismic risk maps for bridge location. The scaling of the earthquake records was made so that the scaled earthquake acceleration was not smaller than the design spectral acceleration, between 0.2 and 1.5 times the dominant period of the bridge. Fig. 10 shows the scaled earthquake record for a 475-year return period, and Fig. 11 shows the spectral acceleration of matched earthquake data and design spectrum for 475-year and 2475-year return periods.

6.1. Damage limit states

In determining the earthquake performance of the bridges, two different earthquake loads were defined: light earthquake (LL) and strong earthquake (UL). The LL earthquake is the earthquake with a high probability of being encountered during the lifetime of the bridge, and although the earthquake load of UL is greater than LL, the earthquake load is less likely to be encountered during the lifetime of the bridge. Damage occurs after extreme events described in the literature with a damage level of bridge elements is categorized into four different classes in the literature. These classes are slight damage, moderate damage, extensive damage, and collapse. In the bridge design, it is aimed to design it in such a way that slight damage could be visualized under LL earthquake to be exposed during the lifetime of the bridge, and bridges could be continuous servicing. Under UL earthquake load, bridges are expected to sustain life safety (extensive damage) damage level, and no collapse phenomena are expected under UL earthquake load.

An important part of the bridge was designed without considering seismic load. As a result, different damage to the bridge under seismic events has been seen. Deficiency of column rotation capacities and shear capacities and damage to bridge bearings and steel braces were seen in the 1978 Miyagi-ken-oki and 2011 Great East Japan earthquakes (Kawashima, 2012). Damage to steel columns, lateral braces, and bearings have also been seen in different earthquake events. Bridges exposed to earthquakes allow engineers to observe bridge performances under real conditions. In light of the data obtained from past earthquakes and experimental studies, many different damage limit states have been identified in the literature for the determination of bridge performance (Table 3) (Bruneau et al., 1996; Bruneau, 1998).

In this study, rotation limits were used to determine the four types of damage in the columns (see Table 3), and the four displacement limits determined for bearing damage are shown in Table 4. Also, yielding and fracture strain limits are used to determine the damage limit state of steel brace members.

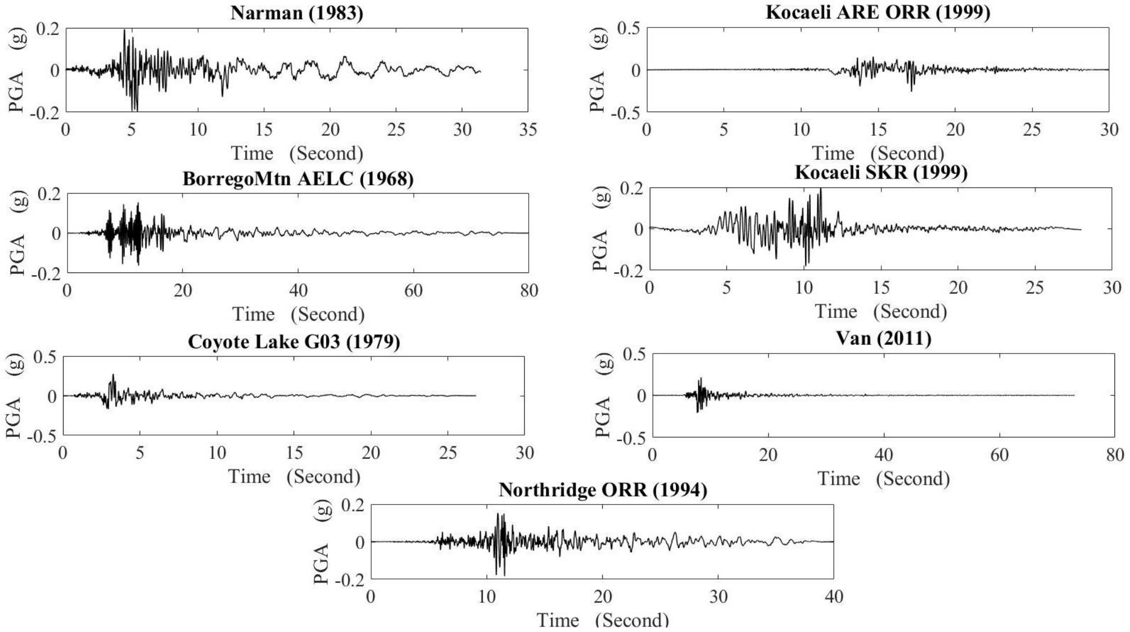

Fig. 10. Matched earthquake record for the 475-year return period.

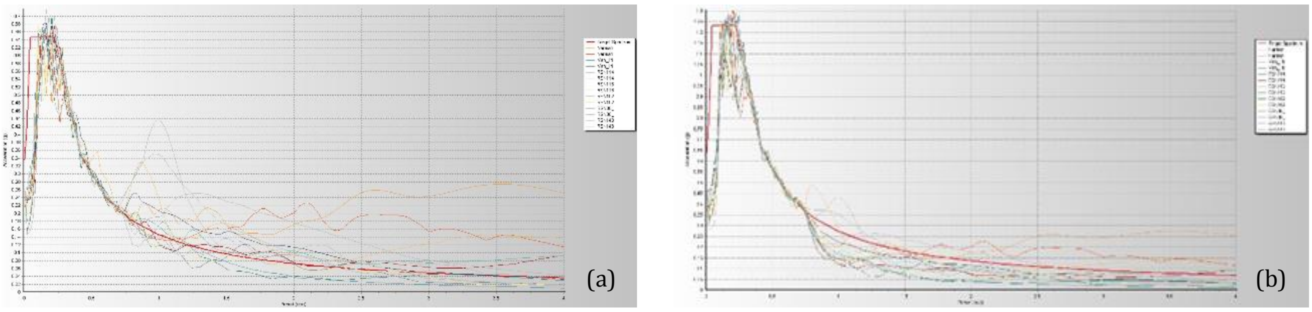

Fig. 11. a) Spectrum acceleration of matched earthquake data and design spectrum for the 475-year return period; b) Spectrum acceleration of matched earthquake data and design spectrum for the 2475-year return period.

Table 3. Column damage limit state.

	Damage State			
	Slight	Moderate	Extensive	Complete
Column Rotation (θ)	θ_y	$2\theta_y$	$4\theta_y$	$8\theta_y$

Table 4 Bearing damage limit state (Nielson, 2005).

	Damage State			
	Slight	Moderate	Extensive	Complete
Pinned Bearing Longitudinal (mm)	28.9	104.2	136.1	186.6
Pinned Bearing Transverse (mm)	28.8	90.9	142.2	195
Sliding Bearing Longitudinal (mm)	28.9	104.2	136.1	186.6
Sliding Bearing Transverse (mm)	28.8	90.9	142.2	195

The yielding rotation of the bridge and column are calculated using Eq (2). Yield rotation for the beam is θ_y=0.01512 for the first and last span and θ_y=0.01827 for the middle spans, and yield rotation for the column is θ_y=0.00414.

$$\theta_y = \frac{W_p F_y I_b}{6EI_b} \quad (2)$$

6.2. Analysis results and discussion

Nonlinear time history analysis was conducted for LL (475-year return period) and UL (2475-year return period) earthquakes. In five of the seven LL earthquake records, the braces were exposed to slight damage; for one LL earthquake, the piers were exposed to collapse damage, for one LL earthquake, the beam was exposed to extensive damage, and for one LL earthquake, sliding bearings were exposed to collapse damage. For seven UL earthquake records, the braces were exposed to slight damage; for three UL earthquakes, the piers were exposed to moderate damage, and for one UL earthquake, the piers were exposed to slight damage. For one UL earthquake, the beams were exposed to extensive damage, and for one UL earthquake, the beams were exposed to slight damage. Two cases of slight, one of moderate and one of extensive damage on the beams, are seen in seven UL earthquake. Tables 5 and 6 show the detailed performance of the bridge components in LL and UL earthquake conditions.

Table 5. Bridge performance for the 475-year return period earthquakes.

	Sliding Bearing	Pinned Bearing	Beam	Pier	Brace
1 Narman (1983)	Collapse	No Damage	Extensive	Collapse	Slight
2 BorregoMtn AELC (1968)	No Damage	No Damage	No Damage	No Damage	No Damage
3 Coyote Lake G03 (1979)	No Damage	No Damage	No Damage	No Damage	Slight
4 Northridge ORR (1994)	No Damage	No Damage	No Damage	No Damage	Slight
5 Kocaeli ARE ORR (1999)	No Damage	No Damage	No Damage	No Damage	No Damage
6 Kocaeli SKR (1999)	No Damage	No Damage	No Damage	No Damage	Slight
7 Van (2011)	No Damage	No Damage	No Damage	No Damage	Slight

Table 6. Bridge performance for the 2475-year return period earthquakes.

	Sliding Bearing	Pinned Bearing	Beam	Pier	Brace
1 Narman (1983)	Slight	No Damage	Extensive	Moderate	Slight
2 BorregoMtn AELC (1968)	No Damage	No Damage	No Damage	No Damage	Slight
3 Coyote Lake G03 (1979)	Extensive	No Damage	Slight	Moderate	Slight
4 Northridge ORR (1994)	Moderate	No Damage	No Damage	Moderate	Slight
5 Kocaeli ARE ORR (1999)	No Damage	No Damage	No Damage	No Damage	Slight
6 Kocaeli SKR (1999)	Slight	No Damage	No Damage	Slight	Slight
7 Van (2011)	No Damage	No Damage	No Damage	No Damage	Slight

Displacement under LL and UL earthquake for longitudinal and transverse directions is calculated using nonlinear time history analysis. Under Narman earthquake conditions, extensive longitudinal deformation is calculated. The mean of LL earthquake longitudinal displacement is 36.4 mm, and without the Narman earthquake, this value decreases to 7.96 mm. The mean value of the LL earthquake transverse direction is calculated as 10.59 mm. The mean values of the UL earthquakes for Longitudinal and Transverse directions are 40.31 mm and 15.34 mm, respectively. These displacements are much smaller than the target displacement calculated using pushover analysis. Fig. 12 shows displacement and intensity measures calculated for LL and UL earthquake records.

Figs. 13 and 14 show the plastic hinge location on the 3D view of the bridge and middle pier hysteretic behavior for LL and UL Narman earthquakes. In the figures, it has been determined that the plastic hinges are intensified at the soil fill boundary of the columns. Soil fill has a great effect on the seismic behavior of the bridge and determines the plastic hinge location. Therefore, bridge performance has varied from the construction date to the present. Time history models solution diverge after extensive plastic deformation at beam elements for both LL and UL Narman earthquakes.

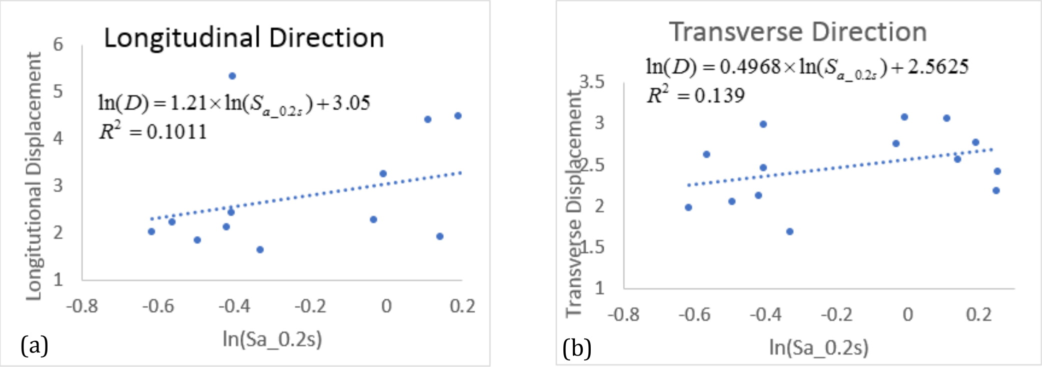

Fig. 12. Displacement and Intensity measure comparison: a) longitudinal direction; b) transverse direction.

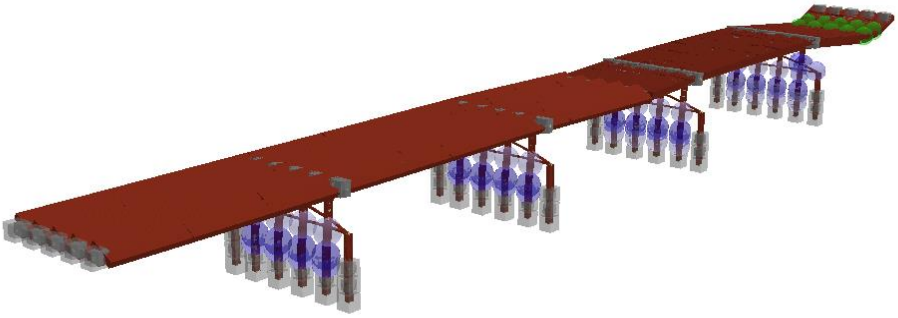

Fig. 13. 3D view of bridge and plastic hinge location for LL Narman earthquake.

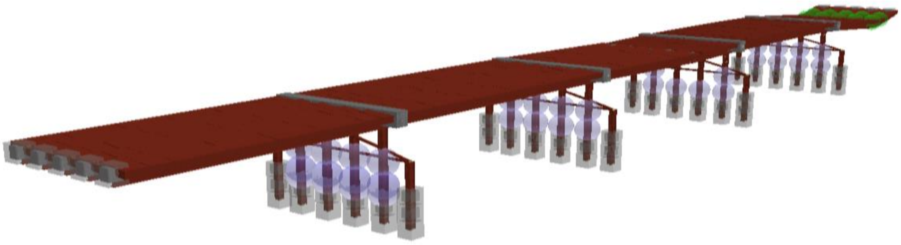

Fig. 14. 3D view of bridge and plastic hinge location for UL Narman earthquake.

7. Conclusions

The finite-element model of the bridge constituted using site investigation and measurement: all the span length and section dimension measured on the bridge. Material properties of the bridge were determined to depend on the construction date of the bridge using past studies in the literature. Modal properties of the bridge calculated using a finite-element model, and modal frequency and modal participation mass ratios were determined. The first mod of the bridge was a longitudinal mod with 0. 49s frequency and represented 55% of the longitudinal mass. The transverse mode frequency was changing between 0.27 s to 0. 33 s and represent 82% of the transverse mass. Finally, the vertical mod frequency calculated as 0.09 s and represent 44% of the vertical mass. Moreover, four different truckloads were applied to the bridge, and maximum moment and vertical displacements were calculated. Maximum moment and displacement visualized under the H20-44 truckload as 41.89 mm and -173.61 kNm, respectively. Vertical displacement limits for the bridge are described as L/800 in ASHTOO bridge design specification. Considering these specifications, the Mahmutcavuş Bridge does not satisfy vertical displacement limits for these four-track loads.

Nonlinear static pushover analysis conducted considering both material nonlinearity and Δ-δ effects. Lateral load acted on the bridge until the top displacement of the middle bridge piers reaches 800 mm in the transverse direction, and plastic hinge formation visualized. The first plastic hinge formed at the brace member, then the next plastic hinge formation started to occur at the bottom of the piers and at the top of the piers. The target displacements for the 2% and 10% possibility, for 50 years period, calculated as 45.36 mm and 22.79 mm, respectively. Finally, the pushover deform shape illustrated to easily calculate the top lateral displacement of all pears.

Seven earthquake records were selected and scaled for 475-year and 2475-year return period earthquake spectrum, which is illustrated by the Turkish Building Seismic Code. Bridge first mod frequency values used to calculate scaling frequency interval. Nonlinear time-history analyses conducted using scaled earthquake records. Damage states for bridge components determined for bridge piers, beams, brace members, and bearing members. For only one of the seven earthquake record collapse damage visualized for sliding bearing and piers. Only one of the seven earthquakes records extensive damage visualized for the beam members for a scaled earthquake for the 475-year return period. For three of seven earthquakes, moderate damage was visualized for piers for scaled seven earthquake records for the 2475-year return period. For LL earthquake, only one record does not satisfy bridge design specification requirement, and for UL earthquake all the record satisfies bridge design code requirement.

REFERENCES

Atmaca B (2019). Determination of minimum depth of prestressed concrete I-Girder bridge for different design truck. *Computers and Concrete*, 24(4), 303–311.

Bruneau M (1998). Performance of steel bridges during the 1995 Hyogoken – Nanbu (Kobe, Japan) earthquake — a North American perspective. *Engineering Structures*, 20(12), 1063–1078.

Bruneau M, Wilson JC, Tremblay R (1996). Performance of steel bridges during the 1995 Hyogo-ken Nanbu (Kobe, Japan) earthquake. *Canadian Journal of Civil Engineering*, 23(3), 678–713.

Damci E, Temur R, Bekdaş G, Sayin B (2015). Damages and causes on the structures during the October 23, 2011 Van earthquake in Turkey. *Case Studies in Construction Materials*, 3, 112–131.

DesRoches R, Choi E, Leon RT, Dyke SJ, Aschheim M (2004). Seismic response of multiple span steel bridges in central and southeastern United States. I: As built. *Journal of Bridge Engineering*, 9(5), 464–472.

Ghosh J, Padgett JE (2010). Aging considerations in the development of time-dependent seismic fragility curves. *Journal of Structural Engineering*, 136, No. December, 1497–1511.

Inel M, Ozmen HB, Bilgin H (2008). Re-evaluation of building damage during recent earthquakes in Turkey. *Engineering Structures*, 30(2), 412–427.

Kawashima K (2012). Damage of bridges due to the 2011 Great East Japan Earthquake. *Journal of Japan Association for Earthquake Engineering*, 12(4), 319–338.

Korkmaz HH, Korkmaz SZ, Donduren MS (2010). Earthquake hazard and damage on traditional rural structures in Turkey. *Natural Hazards and Earth System Science*, 10(3), 605–622.

Kunnath SK, Erduran A, Chai YH, Yashinsky M (2008). Effect of vertical motions on seismic response of highway bridges. *Journal of Bridge Engineering*, 13(3), 282–290.

Larsson T, Lagerqvist O (2009). Material properties of old steel bridges. *Nordic Steel Construction Conference 2009* (*NSCC2009*), 120–127.

Lu Z, Ge H, Usami T (2004). Applicability of pushover analysis-based seismic performance evaluation procedure for steel arch bridges. *Engineering Structures*, 26(13), 1957–1977.

Nielson BG (2005). Analytical fragility curves for highway bridges in moderate seismic zones. *Georgia Institute of Technology*, No. December, 400.

Nielson BG, DesRoches R (2007). Seismic performance assessment of simply supported and continuous multispan concrete girder highway bridges. *Journal of Bridge Engineering*, 12(5), 611–620.

Padgett JE, DesRoches R (2008). Three-dimensional nonlinear seismic performance evaluation of retrofit measures for typical steel girder bridges. *Engineering Structures*, 30(7), 1869–1878.

Rokneddin K, Ghosh J, Dueñas-Osorio L, Padgett JE (2014). Seismic reliability assessment of aging highway bridge networks with field instrumentation data and correlated failures, II: Application. *Earthquake Spectra*, 30(2), 819–843.

Saadeghvaziri MA, Yazdani-Motlagh AR (2008). Seismic behavior and capacity/demand analyses of three multi-span simply supported bridges. *Engineering Structures*, 30(1), 54–66.

Tolon M, Mızrak KC (2017). Development of disaster management in Turkey: from 1999 Kocaeli Earthquake to 2011 Van Earthquake. *International Journal of Engineering Science and Application*, 1(4), 145–151.

Usami T, Ge H (2009). A performance-based seismic design methodology for steel bridge systems. *Journal of Earthquake and Tsunami*, 3(3), 175–193.

Usami T, Lu Z, Ge H (2005). A seismic upgrading method for steel arch bridges using buckling-restrained braces. *Earthquake Engineering and Structural Dynamics*, 34(4–5), 471–496.

Zheng Y, Usami T, Ge H (2003). Seismic response predictions of multi-span steel bridges through pushover analysis. *Earthquake Engineering and Structural Dynamics*, 32(8), 1259–1274.